

# ANALYSIS OF IMAGE NOISE IN MULTISPECTRAL COLOR ACQUISITION

Peter D. Burns

Submitted to the Center for Imaging  
Science in partial fulfillment of the  
requirements for Ph.D. degree at  
the Rochester Institute of Technology

May 1997

The design of a system for multispectral image capture will be influenced by the imaging application, such as image archiving, vision research, illuminant modification or improved (trichromatic) color reproduction. A key aspect of the system performance is the effect of noise, or error, when acquiring multiple color image records and processing of the data. This research provides an analysis that allows the prediction of the image-noise characteristics of systems for the capture of multispectral images. The effects of both detector noise and image processing quantization on the color information are considered, as is the correlation between the errors in the component signals.

The above multivariate error-propagation analysis is then applied to an actual prototype system. Sources of image noise in both digital camera and image processing are related to colorimetric errors. Recommendations for detector characteristics and image processing for future systems are then discussed.

*Indexing terms: color image capture, color image processing, image noise, error propagation, multispectral imaging.*

Electronic Distribution Edition 2001.

©Peter D. Burns 1997, 2001 All rights reserved.

## COPYRIGHT NOTICE

P. D. Burns, 'Analysis of Image Noise in Multispectral Color Acquisition', Ph.D. Dissertation, Rochester Institute of Technology, 1997.

Copyright © Peter D. Burns 1997, 2001  
Published by the author

All rights reserved. No part of this work may be reproduced, stored in a retrieval system, or transmitted in any form, or by any means, electronic, mechanical, photocopying, recording or otherwise, without prior written permission of the copyright holder.

*Macintosh* is a registered trademark of Apple Computer, Inc. *WriteNow* is a registered trademark of WordStar International, Inc. *Expressionist* is a registered trademark of Prescience Corp. *Mathematica* is a registered trademark of Wolfram Research, Inc. *PostScript*, *Acrobat Distiller* and *Acrobat Exchange* are a registered trademarks of Adobe Systems, Inc. *Systat* registered trademark of SPSS, Inc. *DCS Digital Camera* is registered trademark of Eastman Kodak Company.

COLLEGE OF SCIENCE  
ROCHESTER INSTITUTE OF TECHNOLOGY  
ROCHESTER, NEW YORK

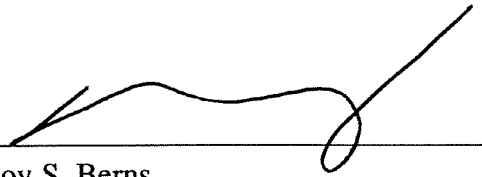
CERTIFICATE OF APPROVAL

---

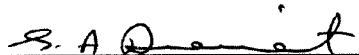
Ph.D. DEGREE DISSERTATION

---

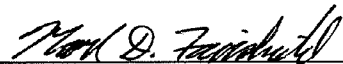
The Ph.D. degree dissertation of Peter D. Burns  
has been examined and approved by the  
dissertation committee as satisfactory for the  
dissertation requirement for the Ph.D. degree in  
Imaging Science

  
\_\_\_\_\_

Dr. Roy S. Berns

  
\_\_\_\_\_

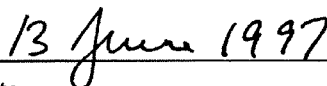
Dr. Soheil Dianat

  
\_\_\_\_\_

Dr. Mark D. Fairchild

  
\_\_\_\_\_

Mr. Edward Giorgianni

  
\_\_\_\_\_

Date

## PREFACE TO ELECTRONIC DISTRIBUTION EDITION

This edition is made available in electronic form as a Portable Document Format (PDF) file, and includes several minor corrections to the printed dissertation, completed in May 1997. In all important respects, however, such as pagination and equation numbering, it is unchanged.

If you have comments about the work or difficulties with this edition of it, please contact me at the e-mail address,

pdburns@ieee.org

*PDB*

*Fairport, New York*

*February 2001*

### *Production of Electronic Edition*

The composition was from the word processing software *WriteNow 4.0*, run on an Apple Power Macintosh, with equations assembled using *Expressionist*. Almost all graphics originated as output from *Mathematica 2.2* notebooks. Apple fonts, Times 12 pt, Helvetica 10 pt, and Symbol 12 pt were used for the body, graphics text and Greek characters, respectively. The PDF distribution files were generated by *Acrobat Distiller 3.0* from intermediate *PostScript* files with all fonts included. Assembly and bookmarking of the final document was done using *Acrobat Exchange 3.0*.

## ACKNOWLEDGEMENTS

This endeavor would not have been completed without the help of many people. I thank my family for accommodating the demands on my time, showing interest in my progress, and providing advice. Completing the degree requirements as a full-time employee, I also benefited from the solid support of several members of Kodak management. They provided early and consistent encouragement for the work, and financial support as part of an employee development program. Although my list is incomplete; Dr. Roger Morton, Mr. Paul Ward, Mr. Terry Lund, Dr. Julie Skipper and Dr. Jim Milch were especially helpful.

My faculty advisor, Prof. Roy Berns, gave generously of his advice, humor and time throughout my research work at the Munsell Color Science Lab. To the other gentlemen of my dissertation committee; Prof. Mark Fairchild, Prof. Soheil Dianat and Mr. Edward Giorgianni, I also extend my thanks for their advice and cooperation.

I would also like to acknowledge several other colleagues and friends at the Center for Imaging Science for their contributions to my studies, especially Drs. John Handley, Ricardo Toledo-Crow and Karen Braun, Mr. Glenn Miller and Ms. Lisa Reniff.

I cannot close without acknowledging two blighters whom I credit with setting my sights higher than I might have, and cultivating the way I look at imaging. Anyone who accuses me of being influenced by Dr. Rodney Shaw and Mr. Peter Engeldrum will not get away without being thanked.

*PDB*

*Fairport, New York  
May 1997*

## TABLE OF CONTENTS

---

I. INTRODUCTION	1
A. Why Analyze Image Noise?	3
B. Multispectral Image Capture	4
C. Spectral Sensitivities: Number and Shape	6
D. Image Noise Propagation	8
E. Quantization	9
F. Technical Approach	12
II. THEORY: MULTISPECTRAL IMAGE CAPTURE AND SIGNAL PROCESSING	13
A. Multispectral Camera	13
B. Principal Component Analysis	17
C. Munsell 37 Sample Set	19
D. Spectral Reconstruction from Camera Signals	27
1. Modified PCA	27
2. MDST and Spline Interpolation	31
3. Direct Colorimetric Transformation	34
III. THEORY: IMAGE NOISE ANALYSIS	37
A. Error Propagation Analysis	37
1. Univariate Transformation	39
2. Multivariate Linear Transformation	41
3. Multivariate Nonlinear Transformation	42
4. Spectrophotometric Colorimetry	44
a. Error in Tristimulus Values	44
b. CIELAB Errors	48
c. CIELAB Chroma and Hue	50
5. Computed Example for Colorimeter/Camera	53
a. $\Delta E_{94}^*$ Color-difference Measure	60
6. Detector Error Specification	63
B. Detector Noise Modeling	65
C. Image Noise Propagation for 3-Channel CCD Camera	69
D. Conclusions	74

## TABLE OF CONTENTS, continued

	Page
IV. EXPERIMENTAL: MULTISPECTRAL DIGITAL IMAGE CAPTURE	77
A. Equipment	77
B. Spectral Measurements of Camera Components	80
C. Photometric, Dark Signal and Illumination Compensation	84
D. Experimental Image Capture	88
E. Conclusions	91
V. IMPLEMENTATION: SPECTRAL AND COLORIMETRIC ESTIMATION	92
A. Estimation for Each Pixel.	92
B. Improving System Accuracy	96
C. Conclusions	102
VI. IMPLEMENTATION: SIGNAL QUANTIZATION AND IMAGE NOISE	103
A. Observed Camera-Signal Noise and Quantization	103
B. Error in Spectral and Colorimetric Estimates	109
C. Verification of error-propagation analysis for camera signals	111
D. Conclusions	115
VII. MODELING IMPROVED CAMERA PERFORMANCE	116
A. Quantization	116
1. Three-channel Camera/colorimeter	118
2. Multispectral Camera	122
B. Imager Noise	124
C. Application to Metamer Characterization	130
VIII. DISCUSSION: SUMMARY CONCLUSIONS AND RECOMMENDATIONS FOR FURTHER STUDY	136
IX. REFERENCES	142

TABLE OF CONTENTS, continued

	Page
<hr/>	
X. APPENDICES	152
A. $\Delta E_{ab}^*$ for PCA Spectral Reconstruction Errors for Munsell 37 data set	152
B. CIELAB Color-Difference Results for Simulated Multispectral Camera Image Acquisition	154
C. Moments of Functions of Random Variables	156
D. Expected Value of $\Delta E_{ab}^*$	159
E. Model for CCD Imager Fixed-pattern Noise	162
F. Measurement of the Kodak Digital Camera Spectral Sensitivity	164
G. Camera Signals for Macbeth ColorChecker Image Capture, Photometric Correction Eqs.	168
H. $\Delta E_{ab}^*$ for PCA and Direct Transformations.	172
I. CIELAB image noise for PCA and Direct transformations	173
J. Camera RMS Noise for Macbeth ColorChecker Image Capture	175
K. CIELAB Color-Differences Due to Multispectral Camera Signal Quantization	177
L. Camera Image Noise as Projected into CIELAB	178

## LIST OF TABLES

	Page
Table 2.1: Percentage of variance attributable to the basis vectors computed from the second moments about the mean vector (covariance) and zero vector for the Munsell-37 sample set.	20
Table 2.2: Summary of the PCA reconstruction for the Munsell-37 sample set $\Delta E_{ab}^*$ given are calculate following reconstruction using 6 and 8 principle components based on the covariance, and second moment about the zero vector. CIE Illuminant A and the 10° observer was assumed.	26
Table 2.3: Summary of CIELAB color-difference error, $\Delta E_{ab}^*$ , following a simulation of multispectral image capture and signal processing, for the Munsell 37 set.	31
Table 3-1: CIELAB values and rms error for the example signal.	58
Table 3-2: $L^*$ , $C_{ab}^*$ , $\Delta H_{ab}^*$ values and rms error for the example signal. The values of the fourth column have been scaled to conform to the $\Delta E_{94}^*$ color-difference measure.	60
Table 3.3: Measured CIELAB coordinates for the 24 patches of the MacBeth ColorChecker, and the calculated CIELAB RMS errors following imager noise model.	74
Table 4-1: Camera settings used for Munsell 37 set and Macbeth ColorChecker target imaging.	85
Table 5-1: Summary of average $\Delta E_{ab}^*$ errors following PCA and the direct colorimetric transformations based on ColorChecker pixel data.	96
Table 5-2: CIELAB $\Delta E_{ab}^*$ errors for spectral reconstruction from experimental camera signals for the Macbeth ColorChecker target via 3 sets of basis vectors.	101
Table 6-1: The unpopulated (8-bit encoded) digital signal levels that were observed for the camera images of several steps of a photographic step tablet.	105
Table 6-2: Summary of the CIELAB errors for estimates computed from ColorChecker pixel data, for PCA and the two direct methods.	110
Table 6-3: Comparison of the standard deviation in the CIELAB coordinates for sample pixel data (n= 400), and error-propagation methods.	114
Table 7-1: Quantization interval as CIELAB color-difference values, for several levels of signal encoding and signal selections.	124
Table: 7-2: Average of calculated stochastic error statistics for ColorChecker samples, due to detector noise (dark- and shot-noise model).	129
Table 7-3: CIELAB coordinates for the reference samples, and average color difference between each and its set of metamers under illuminant A, and the 2° observer.	133

## LIST OF TABLES, continued

	Page
Table 7-4: Results of the multivariate test (0.99 level) for significance difference between the mean reference and corresponding metamer CIELAB coordinates for illuminant $D_{65}$ , based on the camera model in experiment 1.	135
Table 7-5: Results of the multivariate test (0.99 level) for significance difference between the mean reference and corresponding metamer CIELAB coordinates for illuminant A, based on the camera model in experiment 2.	136
Table A-1: PCA reconstruction errors for the Munsell-37 set, where p is the number of components used.	147
Table B-1: Average CIELAB errors calculated from model image acquisition	149
Table: G-1: The average camera signal value for each of the color samples in the ColorChecker target.	163
Table: G-2: The average dark signal value for each of the color samples in the ColorChecker target.	164
Table: G-3: The average white reference signal value for each of the color samples in the ColorChecker target.	165
Table H-1: Average colorimetric errors, $\Delta E_{ab}^*$ , based on the processing of captured ColorChecker pixel data by the PCA method, simple direct (Eq. 2-10) and complex direct (Eq. 2-11) calculations.	166
Table I-1: RMS colorimetric errors and $E[\Delta E_{ab}^*]$ based on the processing of captured ColorChecker pixel data by the PCA method.	168
Table I-2: RMS colorimetric errors and $E[\Delta E_{ab}^*]$ based on the processing of captured ColorChecker pixel data by the two direct colorimetric transformations.	169
Table: J-1: The observed camera rms noise for each of the color samples in the ColorChecker image files.	170
Table: J-2: The observed camera rms dark for each for the image locations and camera settings used for the ColorChecker target capture.	171
Table K-1: CIELAB color-differences due to uniform camera signal quantization, and modified PCA spectral reconstruction.	172
Table L-1: Stochastic errors in CIELAB due to detector noise, following the dark- and shot-noise model.	173

## LIST OF FIGURES

	Page
Fig. 2-1 Elements of of a multispectral camera.	14
Fig. 2-2 The spectral sensitivities of each of the seven filter-sensor channels	16
Fig. 2-3 Mean vector (a), and the first eight basis vectors for the Munsell-37 spectral reflectance set. The vectors are based on the covariance matrix about the mean.	21
Fig. 2-4 The first eight basis vectors for the Munsell-37 spectral reflectance set. These are based on the second-moment matrix about the zero vector. The first component is spectrally non-selective, similar in shape to the mean in Fig. 2.3 (a).	24
Fig. 2-5 PCA spectral reconstruction for a Munsell color sample, 5PB5/10, using an increasing number of components. (a) is based on the components of Fig. 2.3, and (b) is based on those of Fig. 2.4.	25
Fig. 2-6 Outline of the modified PCA spectral reconstruction from the digital camera	28
Fig. 2-7 Relative spectral power distributions for the incandescent light source used with the experimental camera (exp.), CIE illuminants A and $D_{65}$ .	29
Fig. 2-8 The simulated mean and rms spectral reconstruction errors for the modified PCA method, and the Munsell 37 sample set.	30
Fig. 2-9 The basic steps in the MDST interpolation method	32
Fig. 2-10 MDST interpolation of simulated camera signals for a munsell color sample, 5PB5/10.	33
Fig. 3-1: ASTM, 10 nm weights for CIE illuminant A and the 10° observer.	48
Fig. 3.2 Error ellipsoid (95%) for the measured tristimulus values example.	54
Fig. 3-3: The three projections of the CIELAB error ellipsoid (95% confidence) for the example.	56
Fig. 3-4 $L^*$ , $a^*$ , $b^*$ error ellipsoid about the mean (95% confidence) for the example.	57
Fig.3- 5 $\Delta L^*$ , $\Delta C_{ab}^*$ , $\Delta H_{ab}^*$ error ellipsoid for the example color.	59
Fig. 3-6 Error ellipsoid based on transformed $\Delta L^*$ , $\Delta C_{ab}^*$ , $\Delta H_{ab}^*$ coordinates, consistent with the $\Delta E_{94}^*$ color-difference measure.	62
Fig. 3-7 Model for electronic image detection	66
Fig. 3.8 RMS imager noise model as a function of mean signal and fixed-pattern gain noise.	69
Fig. 3.9: Spectral sensitivity functions of detector and optics in arbitrary units.	70
Fig. 3.10: RMS noise characteristics for model imager, where signal and noise are expressed on a [0-1] scale.	73
Fig. 4-1 Experimental multispectral camera layout	78
Fig. 4-2 Kodak Professional DCS 200m digital camera	79
Fig. 4-3 Measured spectral radiance for the copy stand source, in units of $w/sr\ m^2/nm$ .	81
Fig. 4-4 Measured spectral transmittance characteristics, on a [0-1] scale, for the set of interference filters.	82

## LIST OF FIGURES, continued

	Page
Fig. 4-5 Comparison of the measured digital camera quantum efficiency and that calculated from nominal data supplied from Eastman Kodak.	83
Fig. 4-6 Basics steps in image capture in a digital camera	84
Fig. 4-7 Compensation used for the DCS camera for images captured with filter number 3.	86
Fig. 4-8 Observed dark-signal and white reference image characteristics plotted as a function of pixel location.	88
Fig. 4-9. Captured images of the ColorChecker target with filters 1-8.	90
Fig. 4-10 Digital camera signal for the f3 image, before photometric calibration (camera), corrected and with the reference white correction also applied.	91
Fig. 5-1: Examples of spectral reconstruction from 8 digital camera signals using 8 basis vectors.	93
Fig. 5-2: Example estimated spectral reflectance factor for the Neutral 3.5 (a) and Blue (b) samples following PCA reconstruction based on a single pixel set of seven values.	94
Fig. 5-3: Examples of spectral reconstruction from 8 digital average camera signals using 8 basis vectors. (a) is for the Neutral 3.5 sample, and (b) for the Blue sample.	98
Fig. 5-4: Estimated spectral reflectance factor for the Blue color sample using 8 basis vectors, model camera-, and actual camera signal values.	99
Fig. 5-5: Mean and maximum $\Delta E_{ab}^*$ following modified PCA spectral reconstruction from camera signals, versus the number of basis vectors used.	101
Fig. 6-1: Observed rms noise levels for capture of ColorChecker target, for several images taken varying the camera exposure and lens f/number settings.	104
Fig. 6-2: Observed rms noise for capture of ColorChecker target, with all eight image records pooled.	105
Fig. 6-3: Example histograms of pixel values for two uniform image areas (n = 400).	106
Fig. 6-4: Observed camera signal quantization interval in units of 8-bit counts.	107
Fig. 6-5: The internal camera look-up table that was estimated from the observed signal quantization.	108
Fig. 6-6: The result of propagating the observed rms image noise to effective imager noise levels.	109
Fig. 6-7: RMS error in the estimated spectral reflectance factor, based on modeled signal path and set of 400 pixel values.	110
Fig. 7-1: Average quantization interval color-difference, $\Delta E_{ab}^*$ , that results from the uniform quantization of tristimulus values, 8, 10 and 12-bit encoding for achromatic colors.	119
Fig. 7-2: Nonuniform quantization scheme using a uniform quantizer and a discrete m-to-n look-up table transformation.	120

## LIST OF FIGURES, continued

	Page
Fig. 7-3: Average quantization interval color-difference, $\Delta E_{ab}^*$ , that results from the nonuniform, power-law quantization of tristimulus values and 10-bit encoding for achromatic colors.	121
Fig. 7-4: Average quantization interval color-difference, $\Delta E_{ab}^*$ , for the example camera when the R, G, B signals are quantized according to a power-law using 10-bit encoding.	122
Fig. 7-5: Analysis of signal quantization for the multispectral camera and spectral reconstruction via the modified PCA method.	123
Fig. 7-6: Example of spectral reconstruction of the ColorChecker Cyan color.(a) and (b) show signal (solid) and rms noise (symbol). (c) shows the signal-to-noise ratio.	128
Fig. 7-7: Reflectance factors for one reference (5BG3/6) and the set of computed metamers.	132
Fig. E-1: Results of Fixed-pattern noise simulation.	163
Fig. F-1 Measured spectral irradiance for the monochromator source used to measure the spectral sensitivity of the DCS 200m digital camera, in units of $\text{j/m}^2/\text{nm} \times 10^3$	165
Fig. F-2 Two stage model of digital camera spectral sensitivity and signal processing	166

## **I. INTRODUCTION**

During the specification and design of most color-imaging systems, much attention is given to the system's ability to capture and preserve the required color information. Measures of the accuracy of color reproduction often indicate the extent of deviation from desired performance. Also important are limitations to the precision of the system, exhibited by unwanted pixel-to-pixel variations. This image noise contributes to the appearance of graininess and artifacts in viewed scenes, and impedes signal detection and other image processing tasks. The architecture of a system and the consequent signal processing can affect the extent and form of the stochastic error in a recorded or displayed image. This image noise is rarely analyzed in terms of its physical origins and how it propagates through various signal transformations. Such an analysis would be useful in predicting the likely performance and the contribution of each stage to the final image noise.

Noise propagation with statistical descriptions of imaging mechanisms has most often been modeled for monochrome imaging systems. Multichannel system analysis often assumes simple additive sources, and ignores the effect of correlation between the noise fluctuations in the signals. The results of more extensive error analysis, however, have been reported in the related areas of spectrophotometry and colorimetry.

In the research reported here, the objective is to provide an analysis of common sources of stochastic noise in multistage electronic-imaging systems, and how they contribute to the final image noise characteristics. The approach will be to describe how the first two statistical moments of the image noise are propagated. This analysis is applicable to both trichromatic and multispectral image acquisition. For several common signal transformations, the mean level and noise statistics will be described. This facilitates the comparison of actual performance with that limited by fundamental signal-detection

mechanisms, such as available exposure the quantum efficiency of the detector. The effect of the precision used for signal storage, i.e., quantization, is also analyzed and compared with stochastic noise levels.

The above analysis is then applied to the task of spectral reconstruction, or estimation, in the visible wavelength range. A CCD camera-based system is then used to capture several multispectral images. The resultant image noise characteristics are compared with performance predicted by the above theoretical analysis.

The objective of this dissertation research is to provide a statistical analysis of the noise limitations to system performance that result from image acquisition and signal processing in multispectral color systems. The general results are expressed in measurable performance parameters that are familiar to the color and imaging science technical communities. The specific objectives of the research are given below.

1. To develop an analysis of image-noise propagation that includes the following:
  - electronic image acquisition noise model
  - detector spectral sensitivity
  - signal matrixing
  - nonlinear signal transformations
2. To apply the above to the problem of spectral reconstruction, and subsequent colorimetric transformation.
3. To develop a model of the noise characteristics of a system using a CCD camera and filter set, based on a physical model of the noise characteristics of the CCD imager and signal processing.
4. To evaluate the noise characteristics of this multispectral camera system and compare

- the results with those predicted by the above analysis.
5. To identify when and where signal quantization contributes significantly to image noise.

### **A. Why analyze image noise?**

The development of communications systems in the last half-century has been aided by the information theory framework, developed by Shannon (1948). He showed, for example, how statistical models of both signal and noise could be used to identify fundamental limits to the efficiency with which information could be encoded and transmitted. Today, the influence of information theory in the design of imaging systems is found not only in image compression, but also in the use of signal-to-noise measures. These can indicate fundamental limits to imaging performance. These measures have been most influential for applications where scene exposure is at a premium such as in medical and astronomical applications (Felgett 1955, Linfoot 1961, Coleman 1977), but also for general CCD image acquisition (Burns 1990), photography and laser printing (Beiser 1966, Burns 1987a).

Electronic imaging systems often combine various technologies, and a consistent analysis of imaging performance aids in the matching of the requirements of each stage. Since noise is a key image quality characteristic, analysis of its sources and how they combine is an important tool. Specifically, if a physical model is available to describe the signal and noise performance of a system in terms of design choices, it can be used as an aid for component selection and system optimization. A useful analysis, therefore, should predict imaging performance and quantify the effect of specific design parameters and technology choices. The imaging characteristics of the acquisition step are particularly important since they limit the image information available later for image processing and

display.

The research reported here develops a general statistical analysis applicable to multispectral image capture. Before describing the technical approach, a review of multispectral imaging in the visible wavelength region is presented.

### **B. Multispectral imaging capture**

In most color imaging systems, three different signal values, corresponding to three wavelength weightings, are recorded or estimated for each location in a scene. For example, a television camera, or photographic film records three signals associated with the approximately red, green and blue intensities in the image. Colorimetry is based on the trichromatic nature of human vision (Wyszecki and Stiles 1982), that makes it possible to match a given object color with an appropriate optical mixture of three light sources for a given viewing condition. For specific viewing conditions, if the three spectral sensitivities of the capture stage are matched to the three emissions of the display (or spectral reflectance of the print) stage, accurate color reproduction can be achieved for colors within the color gamut of the display.

There are several color-imaging applications, however, where three image records are insufficient to capture all the needed color information. If the spectral sensitivities available do not correspond to those of human vision, or a linear combination of them, color information will be lost. Some colors that are viewed as different, will be recorded as having the same (3) signal values, and will therefore be indistinguishable at the image display. This is referred to as metamerism. To alleviate this problem, missing spectral information can be supplied by additional image records.

For most image printing and publishing applications, a reproduced image is viewed

under different illumination than was used for original scene capture. To transform image data to represent the same scene captured under a different illuminant, one needs a model of the color image formation for all object colorants in the scene. This is practical if it is known that the scene is, e.g., a page whose colors are formed by mixing a set of inks, or photographic dyes. The transformation of the image between illuminants can take the form of a polynomial model (Hung 1993) based on extensive measurements. Alternatively, an analytical model that describes how the image colorants mix to form the color stimuli in the scene (Allen 1980, Berns 1993) can be employed. In such models a reconstruction of the spectral reflectance or transmittance curve is an intermediate step, whether explicit or implied. If an accurate spectral model is unavailable then color reproduction is inaccurate, e.g., when a purchased product does not ‘match’ its reproduction in a printed catalogue. In this case more complete information about the spectral reflectance of the product is needed than is supplied by the three (although colorimetrically accurate) signals.

The archiving and conservation of artworks are other areas where both colorimetric and multispectral image information are currently being used. This is being done for various reasons, with varying technical requirements. The approaches include: photography (Miller 1995), spectrophotometry (Quindos *et al.* 1987, Grosjean *et al.* 1993), and electronic image capture (Saunders 1989, Martinez *et al.* 1993). Martinez and Hamber (1989) discuss the requirements for three applications: public access and galleries, university study, and scientific/conservation work. They recommend both the required levels of color and wavelength information, and spatial detail sampling for the above uses of image archives.

Colorimetric and multispectral image information are also frequently used in remote sensing (Juday 1979). Infrared information is often combined with the visible light record,

and displayed in pseudo-color. In astronomy, colorimetric data and knowledge of human vision have been used to improve stellar observations. Since stars can be modelled as black body sources their spectral emissions are governed by the Planck formula. Chollet and Sanchez (1990), modeled the attenuation of the star emission by the atmosphere and instrument optics. They then introduced the spectral sensitivity of the observer, including the Purkinje phenomenon, to estimate the mean wavelength. This approach reduced systematic error in the estimation of the magnitude of stars.

### C. Spectral Sensitivities: Number and Shape

Various approaches to characterizing object spectral reflectances have been reported, aimed at determining the number of required spectral image records. Several workers have used statistical modeling to identify the fundamental characteristic spectra for various classes of objects. Cohen found that four basis spectra could be combined to reconstruct, or specify, a selection of Munsell colors (Cohen 1964). A subsequent study, however, found up to eight were needed for a larger set (Kawata *et al.* 1987). More recent research included a wide variety of natural and manufactured object spectra, and concluded that up to seven basis vectors were needed to characterize some objects (Vrhel *et al.* 1994). Note that the basis vectors that were identified do not necessarily correspond to physically realizable detector-filter spectral sensitivities. However a set of spectral sensitivities that are linear combinations of the eigenvectors could be used.

The shape of capture spectral sensitivity functions also can be addressed by starting from the eigenvectors of the spectral covariance matrix. Chang and coworkers (1989) took this approach and investigated the use of the first three Fourier basis functions. They demonstrated that band-limited (slowly varying) spectra could be well reconstructed by a wide variety of spectral sensitivity shapes. This should be expected, given that the first

Fourier bases are associated with low-frequency signal components.

We can also treat the capture of color-image information as a spectral sampling problem for a set of detectors with all-positive responses. For any sampled signal, there is an inverse relationship between the sampling distance, and the detailed information that is unambiguously captured. For a given imaging application, if it is necessary to differentiate between samples containing rapid spectral fluctuations, then this requires a set of several narrow-band capture spectral sensitivities.

Both human vision, and object spectral reflectance characteristics have been analyzed for the required (or implied) spectral sampling. The characteristics of color vision were described in terms a Modulation Sensitivity Functions (MSF) of spectral frequency, analogous to the more commonly used Modulation Transfer Functions (MTF) of spatial frequency (Benzschawel *et al.* 1986). Various color vision models were characterized in terms of both their modulation and phase responses. The Fourier transforms of the CIE color matching functions have also been calculated (Romero *et al.* 1992) to understand the spectral sampling requirements of (trichromatic) color vision. Limiting frequencies of 0.02 cy/nm for  $\bar{x}$  and  $\bar{z}$ , and 0.05 cy/nm for  $\bar{y}$  were estimated. It was concluded that spectral sampling of 10-25 nm would be sufficient for colorimetric matching. This analysis, however, overlooked the fact that the spectral bandwidth of information is determined by the combination of illuminant, color matching and object spectral reflectance functions. It has been observed that this is equivalent to a convolution of the Fourier transform of these functions in the frequency domain (Burns 1994).

Stiles and co-workers (1977) decomposed a set of object reflectance spectra into band-limited basis functions. Sample spectra with at most four oscillations in the visible range were characterized as having a limiting frequency of 0.02 cy/nm, which implies a required

spectral sampling of about 25 nm, if equally spaced in wavelength. In a study of simulated ideal all-positive spectral sensitivities using Macbeth ColorChecker colors (McCamy *et al.* 1976), improvements were found in the spectral reconstruction from 3 to 7 bands, but little beyond that number (Ohta 1981).

The CIE chromaticity coordinates for band-limited reflectance spectra have also been investigated (Buchsbaum and Gottschalk 1984) and plotted as a ‘frequency-limited signal gamut’. Gamuts corresponding to spectral bandwidths from 0.033 to 0.005 cy/nm were compared with those for the NTSC color television primaries. The conclusion was that band-limited metamers can be found for most practical colors.

To date little attention has been paid to the limitations to the performance of practical multispectral imaging systems imposed by signal uncertainty, or noise. While its presence is acknowledged, error measures are often given in terms of the variation of mean differences across the color space. The research reported here aims to provide an analysis that is generally applicable to the propagation of stochastic image variations (across an image or day-to-day). It is intended to facilitate both the interpretation of observed performance, and its reduction when necessary.

#### **D. Image Noise Propagation**

The presence of image noise is acknowledged in reports of practical multispectral imaging systems (e.g. Saunders and Hamber 1990). Analysis of its sources, and how they combine and propagate through a system, however, is rare. Noise is usually described as a constant-magnitude, stochastic source which is added to each signal with independent distributions. Thus it is often assumed that the least significant one or two bits of encoded signal information are corrupted. While this simplifies subsequent analysis, it is not based on a physical description of its origins, and sheds no light on how its effect could be

reduced by design choices. Recently, Engelhardt and Seitz (1993) addressed the effect of detector noise in the design of optimal filters for a CCD camera with a color filter array. They included a shot noise and CCD crosstalk simulation in a numerical method based on simulated thermal annealing.

Physical modeling of noise is commonly applied to multistage monochrome systems, and usually includes the spatial (Wiener, or noise power, -spectrum) characteristics. Example applications include, photography (Doener 1965), radiography (Rossmann 1963), laser printing (Burns 1987a) and CCD image acquisition (Burns 1990). While the spatial characteristics of image noise in multispectral imaging systems may also be important, they will not be explicitly addressed here.

For multispectral image noise analysis one can borrow from the approaches taken in addressing colorimetric and spectrophotometric measurement error. For example several workers (Nimeroff 1953, 1957, 1966, Nimeroff *et al.* 1961, Lagutin 1987) have addressed error propagation from instrument reading to chromaticity coordinates. In addition, propagation of uncorrelated measurement errors in the nonlinear colorimetric transformations from tristimulus values to perceptual color spaces has also been described (Robertson 1967, Fairchild and Reniff 1991). Methods of correcting for systematic measurement error due to spectrophotometer bandpass, wavelength scale and linearity (Stearns 1981, Stearns and Stearns 1988, Berns and Peterson 1988, Berns and Reniff 1997) have also been reported.

## **E. Quantization**

One factor that determines the precision with which images are stored in digital systems is the way in which the continuous detected signals are encoded using discrete levels. Not

only is the number of levels important, but also the spacing of them over the expected signal range (minimum to maximum value). The number of levels is usually specified by the required storage, for example an eight-bit byte can be used to encode a signal by rounding each pixel value to one of  $2^8=256$  levels. Most analog-to-digital converters (ADC) are uniform quantizers, i.e., they round to equal increments of input signal. Nonuniform quantization is achieved by preceding the ADC with a nonlinear analog circuit, which must have a stable, distortion-free response at a high temporal bandwidth. More frequently, nonuniform quantization is achieved in two steps. The signal is first quantized using  $m$  levels at uniform intervals. This discrete signal is then transformed via a look-up table to one where the signal is rounded to one of  $n$  output levels, where  $n \leq m$  ( $m$ -to- $n$  mapping). The form of the look-up table determines the input analogue signal values that correspond to the  $n$  output levels, so that when they are projected back to the continuous input signal, they are usually at non-uniform intervals.

Considerations of the number of required colors available for imaging systems fall into two types. First, for any single typical scene, a limited number of object colors are available for image capture, due to a limited number of reflective materials and light sources. This leads to the conclusion that for 3-channel (e.g. colorimetric) imaging, the required pixel values take the form of a scene-dependent set of quantized levels, i.e., a palette of colors. For this form of image compression various algorithms are available for selecting the set of levels, based on the statistics of pixel values (Gentile *et al.* 1990). In addition, human vision has also been analyzed in terms of the number of simultaneous colors that are discernible in a single image (Buchsbbaum and Bedrosian 1984).

A second, and more common approach to analyzing signal quantization requirements is to estimate the errors in the multi-dimensional signal (space of all possible signal values)

introduced as a function of number and spacing of the available quantization levels. The quantizing of multi-dimensional signals and the interpretation of the resultant differences in a transformed (perceptual) space is a common theme. Recommendations for the required number of levels, however, vary depending on the signal space for both image capture and display, intended image usage (display), and perceptual criterion used. A recent study (Gan *et al.* 1994) suggested that up to 42 bits/pixel are needed for RGB signals with quantization errors interpreted in Munsell color space, or 31 bits/pixel if nonuniform quantization is achieved by prior analog transformation.

Approximately the same requirements were identified when quantizing tristimulus values and interpreting the results in CIELAB. Quantization by truncation, rather than rounding, required 12-13 bits/sample for each of the *XYZ* or *RGB* signals (Ikeda 1992). Analysis for a CCD camera (Engelhardt and Seitz 1993) included quantization of the original RGB signals, of displayed images, and of the arithmetic precision of the calculated matrix transformation. It was concluded that the output display introduced the main degradation, and that 10-12 bits/signal (30-36 bits/pixel) would be sufficient. Stokes *et al.* (1992) also concluded that approximately 10-bit encoding is required for image display.

The effect of signal quantization in a multispectral system was also addressed for imaging of paintings by Saunders and Hamber (1990). They concluded that, for the task of detecting small signal differences, 10 bits/signal were found to yield acceptable results for several filter sets. This simplified analysis, however, assumed that the two least significant bits were corrupted by noise.

In a more general treatment of the subject, both image dependent (palette selection) and image independent quantization of tristimulus values have been interpreted in terms of the resultant perceptual color space differences (Gentile *et al.* 1990). It was concluded that the visual impression of quantization is reduced by quantizing in more visually uniform color

spaces, but with the cost of increased complexity. Simple linear transformations (such as matrix rotation) yielded minor gains.

### **F. Technical approach**

In this research, it is assumed that analysis of the propagation of the first- and second order statistical moments provides sufficient description of multi-dimensional image noise characteristics. Techniques developed for multistage monochrome imaging systems are extended so they can be used for multi-dimensional signals. The statistical analysis, therefore, becomes multivariate.

We borrow from the approaches taken in addressing colorimetric and spectrophotometric measurement error, and the estimation of image signal-to-noise ratio measures. For example, Nimeroff (1953, 1957, 1966) derived expressions for the propagation of instrument error statistics to the variance and covariance of the resulting tristimulus and chromaticity coordinates. These results are expressed in a matrix notation as the first step in demonstrating their general applicability to common signal transformations in trichromatic and multispectral imaging. This is followed by applying nonlinear noise propagation techniques that have been previously applied to uncorrelated errors, and univariate signal transformations (Burns 1987b). This analytical approach is then applied to a practical system for multispectral image capture, a CCD camera and filter set and compared with observed performance.

## **II. THEORY: MULTISPECTRAL IMAGE CAPTURE AND SIGNAL PROCESSING**

In this chapter, the general characteristics of a multispectral camera are described. This is followed by a description of a specific system based on a monochrome digital camera used with a set of interference filters. Several approaches to spectral reconstruction based on the camera signals are developed.

The design of a multispectral camera and its associated signal processing depends on the intended application. It can be assumed, however, that the objective is to acquire spectral rather than merely colorimetric information about an illuminated scene. This information could be used to estimate the spectral reflectance at each pixel. From these data it is possible to calculate a colorimetric representation of the image as viewed under secondary viewing conditions. Alternatively, the  $m$  camera signals could be used to directly calculate colorimetric coordinates at each pixel (Hamber *et al.* 1993). While there are other color applications for multispectral cameras, in this research attention is restricted to those above. This allows the definition of both technical objectives such as reconstruction of the scene spectral reflectance, and the general signal processing steps needed.

### **A. Multispectral Camera**

The basic elements of a multispectral camera are shown in Fig. 2-1. Light from the scene is detected after passing through each of a set of optical filters. The image is stored as  $m$  signal values per pixel. For systems that do not require simultaneous acquisition of all records, such as document or artwork imaging, a multispectral camera can be formed using

a single detector and a set of filters.

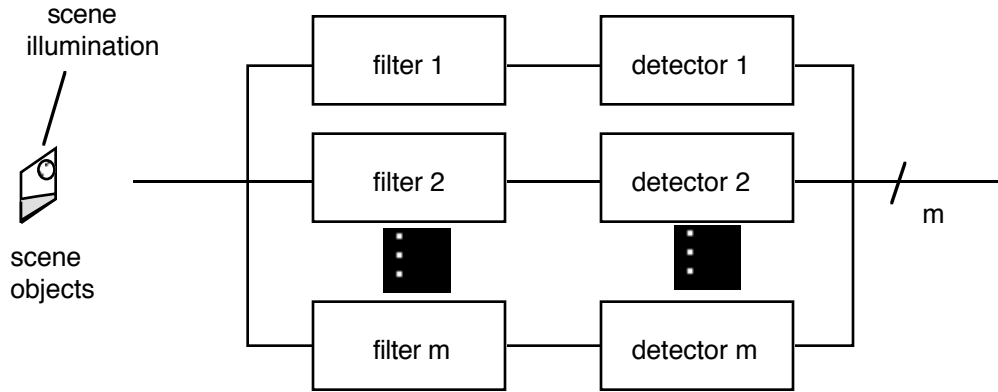


Fig. 2-1: Elements of of a multispectral camera.

One can model multispectral image acquisition using matrix-vector notation. The sampled illumination spectral power distribution is expressed as

$$\mathbf{S} = \begin{bmatrix} s_1 & & 0 \\ & s_2 & \\ 0 & & \ddots \\ & & & s_n \\ & & & & 0 \end{bmatrix},$$

and the object spectral reflectance is  $\mathbf{r} = [r_1, r_2, \dots, r_n]^T$ , where the index indicates the set of  $n$  wavelengths over the visible range, e.g. [380, 410, ..., 730 nm] and  $^T$  the matrix transpose. If the transmittance characteristics of the  $m$  filters are the columns of  $\mathbf{F}$

$$\mathbf{F} = \begin{bmatrix} f_{1,1} & f_{1,2} & \cdots & f_{1,m} \\ \vdots & \vdots & \cdots & \vdots \\ f_{n,1} & f_{n,2} & \cdots & f_{n,m} \end{bmatrix},$$

and the spectral sensitivity of the detector is

$$\mathbf{D} = \begin{bmatrix} d_1 & & 0 \\ & d_2 & \\ & & \ddots \\ 0 & & & d_n \end{bmatrix},$$

then the captured image, assuming a linear detector characteristic, is

$$\mathbf{t} = (\mathbf{DF})^T \mathbf{Sr} . \quad (2-1)$$

If the filter and detector spectral characteristics are combined,  $\mathbf{G} = \mathbf{DF}$ , then

$$\mathbf{t} = \mathbf{G}^T \mathbf{Sr} . \quad (2-2)$$

To investigate the capabilities of a practical multispectral camera, a set of seven interference filters manufactured by Melles Griot was chosen to sample the visible wavelength range at intervals of approximately 50 nm. This equal-interval sampling does not favor the characteristics of any particular radiation sources, nor class of object spectra (e.g., manufactured colorants or natural objects). On the other hand, the transmittance functions impose a reduced spectral-frequency bandwidth on the acquired signals. This is analogous to the smoothing of spatial information by the collection optics and scanning aperture prior to sampling in a document or film scanner.

The input device selected for this study was the Kodak Professional DCS 200m (monochrome) digital camera. The lower sensitivity of the CCD imager in the short wavelength regions, coupled with the throughput of the filters results in a wide range of

relative spectral sensitivities, as shown in Fig. 2-2. Further details of the experimental procedures used to characterize and operate the camera and filter set are deferred until Chapter IV. It is simply assumed here that the filter set and camera combination are ideal and characterized by the spectral responses shown in Fig. 2-2.

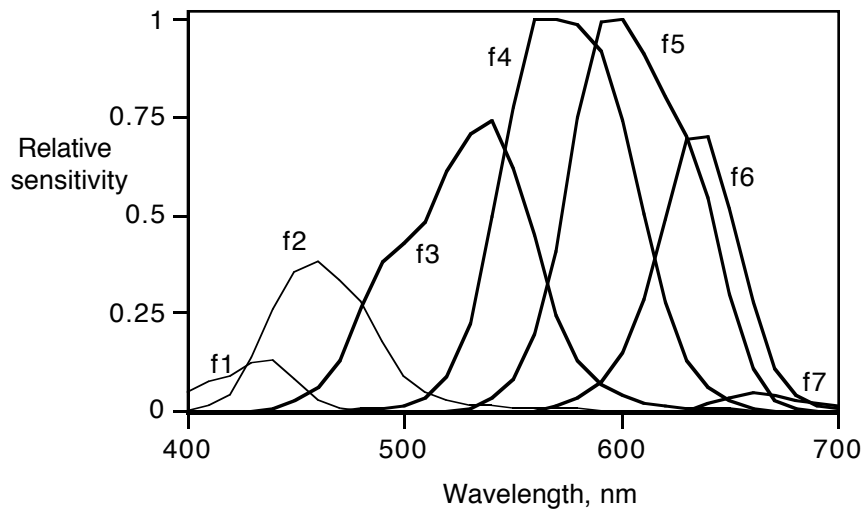


Fig. 2-2: The spectral sensitivities of each of the seven filter-sensor channels.

The  $m$  camera signals will rarely be in a form that yields the required information about the scene. For example, if the intent is to obtain the object spectral reflectance function at each pixel, then further signal processing is required. As with most signal processing, *a priori* information about the signal population can be useful in estimating the scene spectral characteristics from the camera data. Specifically, linear modeling techniques based on principal component analysis (PCA) (Jackson 1991, Jaaskelainen *et al.* 1990, Maloney 1986, and Vrhel *et al.* 1994) have been successfully applied to sets of paints and natural object spectral reflectance functions. The application of PCA to spectral reconstruction from the  $m$  camera signals follows a brief description of PCA.

### **B. Principal Component Analysis**

For a given sample population, the objective usually includes the identification of a small set of underlying basis functions, linear combinations of which can be used to approximate, or reconstruct, members of the population (Jackson 1991). This is easily described in the context of our spectral reconstruction task.

Consider a population of sampled ( $n \times 1$ ) spectral reflectance measurements,  $\mathbf{r}$ , for which one would like to identify the underlying basis vectors. First calculate the ( $n \times n$ ) covariance matrix,  $\Sigma_{\mathbf{r}}$ , which is the multivariate second moment about the mean vector,  $\mu_{\mathbf{r}}$ . Then compute the  $n$  ( $n \times 1$ ) eigenvectors  $\{\mathbf{e}_1, \mathbf{e}_2, \dots, \mathbf{e}_n\}$ , and the scalar eigenvalues,  $\{\lambda_1, \lambda_2, \dots, \lambda_n\}$  associated with each eigenvector. The eigenvectors are the basis vectors for the population of spectral reflectance characteristics. Examination of the eigenvalues indicates the amount of population variance about the mean vector that is explained by each orthogonal eigenvector. When the eigenvalues are arranged in descending order, as is usual, then the fraction of variance explained by the first corresponding  $j$  vectors is

$$v_j = \frac{\sum_{k=1}^j \lambda_k}{\sum_{k=1}^n \lambda_k} .$$

The number of basis vectors,  $p$ , to be used to reconstruct the spectral reflectance vectors is often chosen so that, e.g.,  $v \geq 0.99$ . For populations of reflectance spectra,  $p$  is usually in the range of 5 to 8 (Cohen 1964, Jaaskelainen *et al.*, 1990, Vrhel *et al.*, 1994). Each object reflectance vector in the sample population can be reconstructed, to within an error, from a set of  $p$  scalars. For the  $i$ th sample the reconstructed vector is given by

$$\hat{\mathbf{r}}_i = \Phi \alpha_i + \mu \quad (2-3)$$

where  $\Phi = [e_1, e_2, \dots, e_p]$ , and the set of weights (also called principal components) associated with the  $i$ th sample is  $\alpha_i = [a_1, a_2, \dots, a_p]$ , and  $\mu$  is the  $(n \times 1)$  mean vector. For a given sample reflectance vector,  $\mathbf{r}_i$ , the set of scalar weights can be found by

$$\alpha_i = \Phi^T (\mathbf{r}_i - \mu) . \quad (2-4)$$

PCA allows us to approximate a vector,  $\mathbf{r}_i$ , using only  $p$  scalar values, in combination with the population basis vectors and mean vector. So  $\Phi$  and  $\mu$  represent *a priori* information about the ensemble of vectors to reconstructed. A variation of the above method uses the eigenvectors of the second moments (matrix) about the zero vector, rather than about the mean. In this case the reconstruction equation becomes

$$\hat{\mathbf{r}}_i = \Phi_r \alpha_i \quad (2-5)$$

and

$$\alpha_i = \Phi^T \mathbf{r}_i . \quad (2-6)$$

Considering the form of Eq. (2-6),  $\Phi$  can be interpreted as a set of filter spectral sensitivity vectors that could be use to analyze a sample,  $\mathbf{r}_i$ , for subsequent spectral reconstruction. Therefore, if a multispectral camera could detect  $p$  signals at each pixel, via spectral sensitivities,  $\Phi$ , then the spectral reconstruction could be simply achieved using Eq. (2-5). There are two immediate problems with this approach. First, there is no

guarantee that the camera spectral sensitivities will be practically realizable, and in fact they usually contain negative values. The second limitation is that the camera would be optimized for spectral reconstruction for a single population, rather than for general multispectral imaging.

Despite these limitations to the direct application of PCA to multispectral camera signal processing, it is possible to successfully apply a modified form of the technique to the digital camera system whose spectral sensitivity characteristics were given in Fig. 2-2. Before describing this, however, results are presented for PCA of a set of Munsell color samples.

### **C. Munsell-37 sample set**

For our multispectral image capture and modeling, a group of samples were selected from the Glossy Munsell Book of Color (Munsell 1976). Samples were chosen for 10 hues with three samples per hue at or near the gamut boundary. In addition, seven neutral samples were included for a total of 37 samples. Each sample measured 3.5 cm by 5 cm. A list of the Munsell notations for the samples is given in Appendix A. The spectral reflectance factor of each sample was measured using the Milton Roy ColorScan II/45 spectrophotometer. An established technique (Reniff 1994), that included the measurement of eight standard tiles, was used to obtain spectral reflectance factor data for each sample at 10nm intervals from 400 - 700nm traceable to NIST with minimal systematic spectrophotometric error.

The basis vectors were computed for the second-order moment matrix about the mean (covariance matrix) and about zero. The cumulative percentage of variance accounted for by up to the first eight vectors is shown in Table 2-1.

Table 2-1: Percentage of variance attributable to the basis vectors computed from the second moments about the mean vector (covariance) and zero vector for the Munsell-37 sample set.

p	covariance	moments about zero
1	75.65	89.49
2	92.35	96.65
3	98.35	99.23
4	99.20	99.65
5	99.69	99.86
6	99.87	99.94
7	99.93	99.97
8	99.96	99.98

Figure 2-3 shows the mean vector and first eight principle components for the covariance matrix. These are the set of orthogonal basis functions for the population of spectral reflectance vectors. They represent a set of vectors in  $n$ -space along which the most variation between samples is observed. Although these ( $n \times 1$ ) vectors (directions) are unique, their sign is arbitrary. For example, the same accuracy in spectral reconstruction would be achieved using the first component,  $e_1$ , in Fig. 2-3 (b), which is all-negative, as would be achieved using  $-e_1$ . The first corresponding scalar weight,  $a_1$ , for each color sample would merely change sign. The sign of the principal components may be arbitrary, but the sign of the elements of each is not. This is because a change in the sign of any (other than all) would change the direction of the vector in  $n$ -space. So, although one can select an all-positive form for  $e_1$ , it is not possible do so for the remaining principle components, since they contain both positive and negative elements.

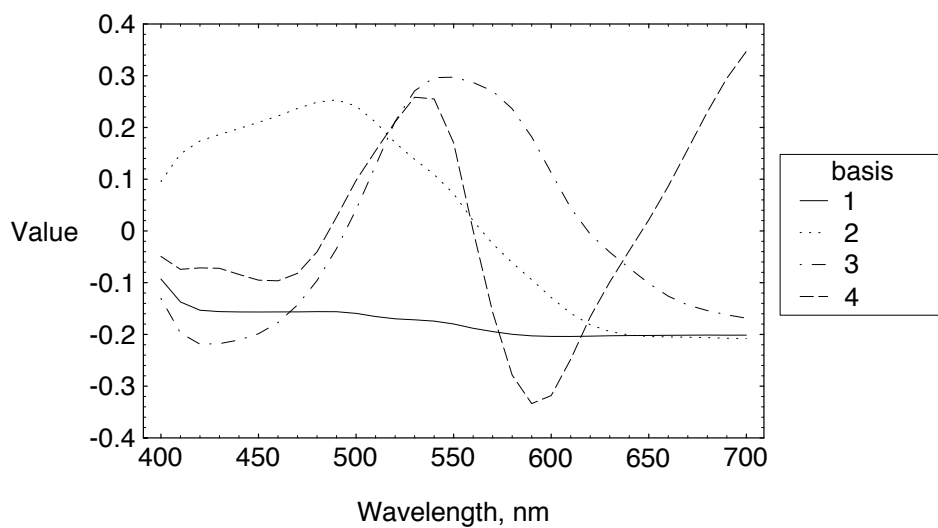
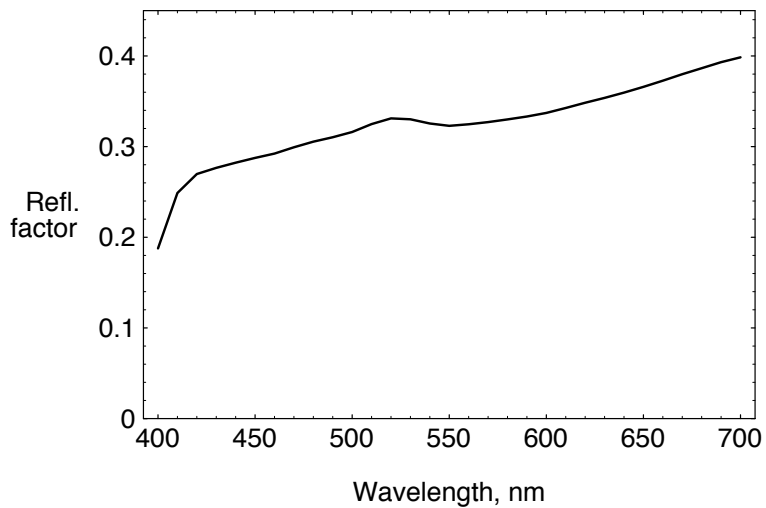


Fig. 2-3: Mean vector (a), and the first four basis vectors (b) for the Munsell-37 spectral reflectance set. The vectors are based on the covariance matrix about the mean.

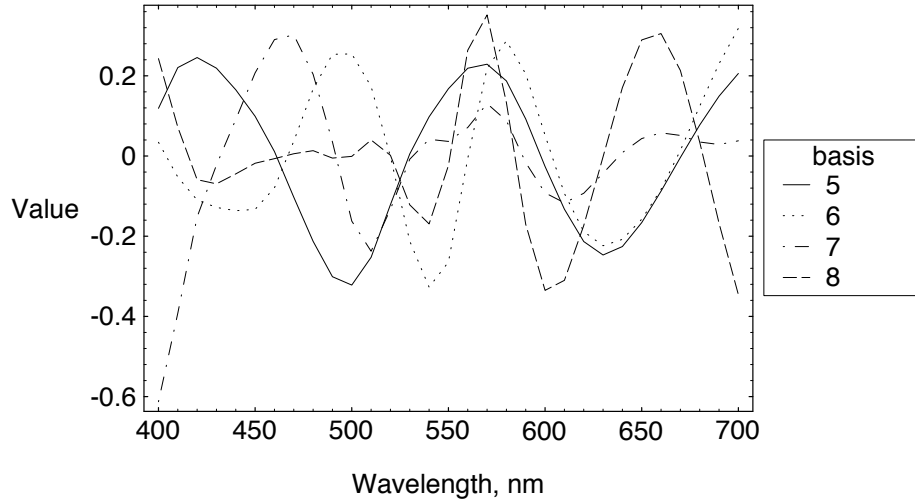


Figure 2-3 (c): The fifth to eighth basis vectors for the Munsell-37 spectral reflectance set. The vectors are based on the covariance matrix about the mean.

The above property of the basis vectors being equivalent under a change of sign is actually a special case of a scaling property. The spectral reconstruction uses a simple linear combination of basis vectors in Eq. (2-3) and (2-5). One is free to scale the vectors by any real value without changing the reconstruction. This can be seen by introducing a scaling matrix

$$\mathbf{K} = \begin{bmatrix} k_1 & & & 0 \\ & k_2 & & \\ & & \ddots & \\ 0 & & & k_n \end{bmatrix}$$

so that the new basis vectors are  $\mathbf{K}\Phi$ . Equations (2-5) and (2-6) become

$$\hat{\mathbf{r}}_i = \Phi \mathbf{K} \alpha_i$$

$$\alpha_i = \mathbf{K}^{-1} \Phi \mathbf{r}_i,$$

where

$$\mathbf{K}^{-1} = \begin{bmatrix} 1/k_1 & & & 0 \\ & 1/k_2 & & \\ & & \ddots & \\ 0 & & & 1/k_n \end{bmatrix}.$$

Some statistical software products, such as *Systat*, present the basis vectors as scaled eigenvectors so that the norm of each is equal to the corresponding eigenvalue. In this analysis any scaling is avoided, so that the components are the eigenvectors with a norm of unity.

The basis vectors calculated from the second moments about the zero vector are shown in Fig. 2-4. Note that the first component is spectrally non-selective, similar in shape to the mean, shown in Fig. 2-3 (a). The remaining vectors are similar to the corresponding ones based on the covariance matrix, shown in Fig. 2-3 (b) and (c).

A corresponding spectral reconstruction based on an increasing number of vectors is shown for a single sample, 5PB5/10, in Fig. 2-5. It is seen that a close approximation is achieved using six or more components for this sample.

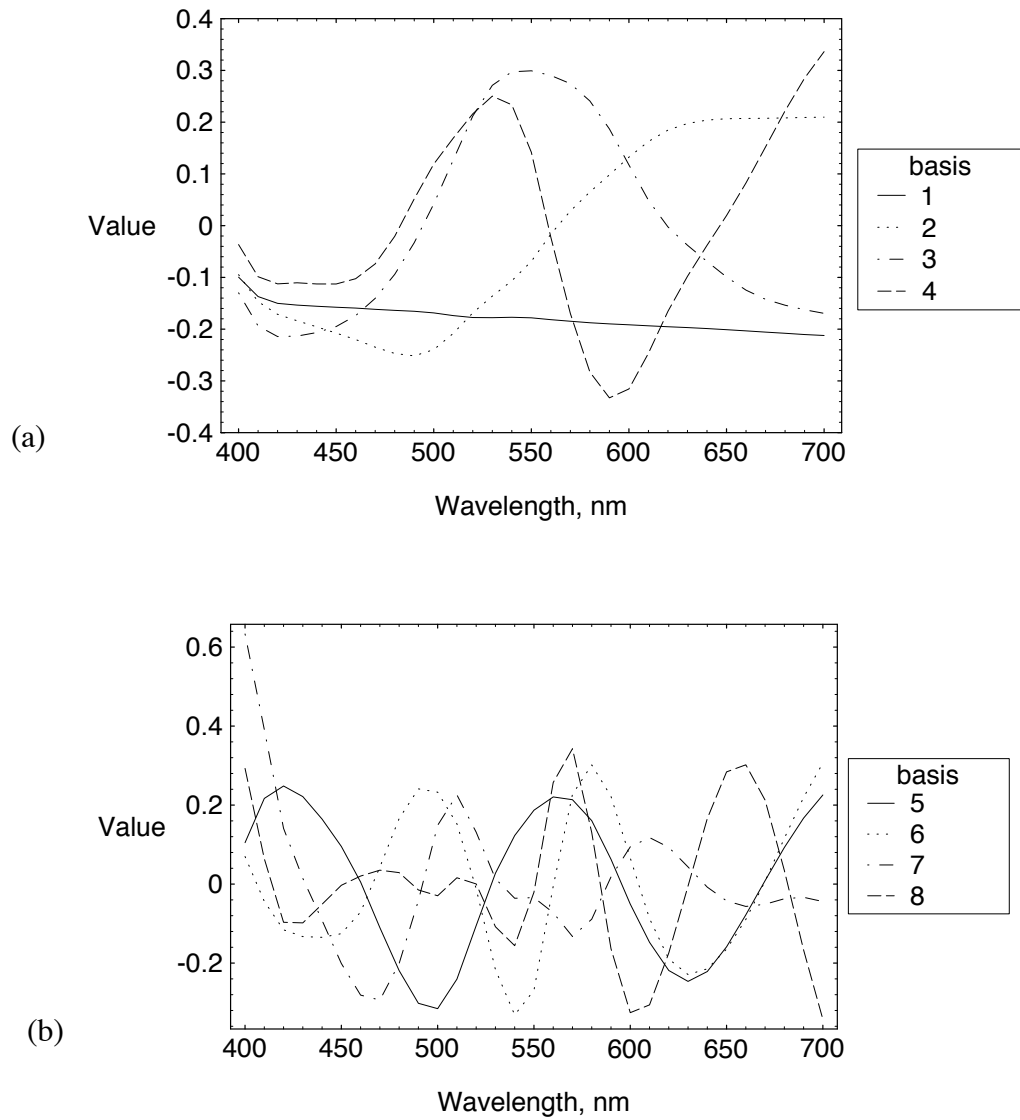


Fig. 2-4: The first eight basis vectors for the Munsell-37 spectral reflectance set. These are based on the second-moment matrix about the zero vector. The first component is spectrally non-selective, similar in shape to the mean in Fig. 2-3 (a).

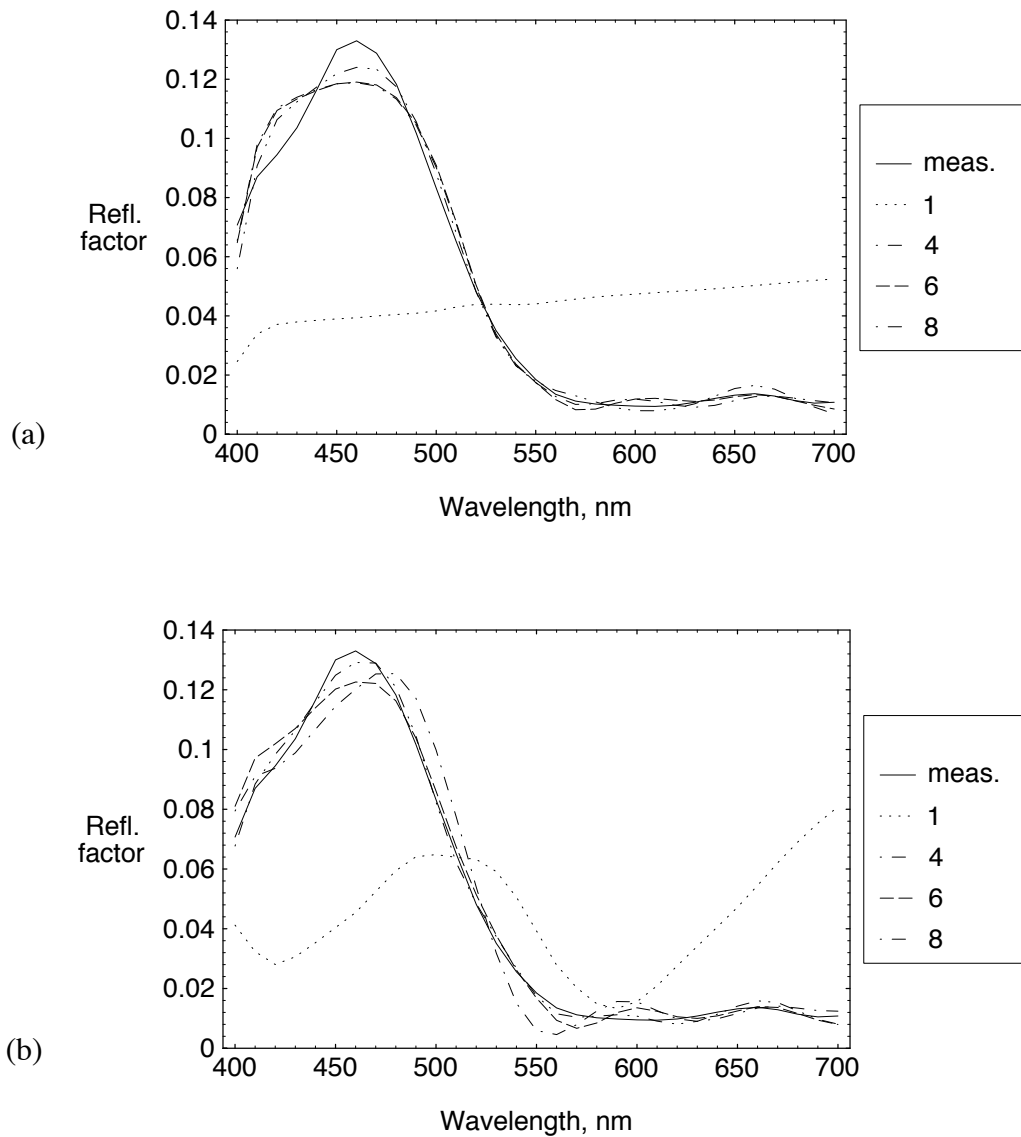


Fig. 2-5: PCA spectral reconstruction for a Munsell color sample, 5PB5/10, using an increasing number of components. (a) is based on the components of Fig. 2-3, and (b) is based on those of Fig. 2-4.

For many applications, estimating the object spectral reflectance is merely an intermediate step toward colorimetric scene information. In these cases a meaningful measure of multispectral image capture is in terms of color differences in, e.g, CIELAB. For each of the measured color samples in the data set the CIELAB coordinates,  $L^*$ ,  $a^*$ ,

$b^*$  (CIE 1986), were calculated using CIE illuminant A and the  $10^\circ$  observer. The corresponding coordinates for the PCA-reconstructed reflectance vector were also computed. The color-difference measure,  $\Delta E_{ab}^*$ , which is the Euclidian distance between the two CIELAB locations, was calculated for each sample. Table 2-2 summarizes the results in the form of the average, minimum and rms  $\Delta E_{ab}^*$  values for the Munsell 37 sample set. Table A-1 in Appendix A lists the corresponding color errors for each sample.

Table 2-2: Summary of the PCA reconstruction for the Munsell-37 sample set  $\Delta E_{ab}^*$  given are calculated following reconstruction using 6 and 8 principle components based on the covariance, and second moment about the zero vector. CIE Illuminant  $D_{65}$  and the  $10^\circ$  observer was assumed. See Table A-1 in Appendix A for more details.

no. components	Covariance		$\Delta E_{ab}^*$ moments about zero	
	6	8	6	8
mean	1.17	0.221	1.18	0.224
max.	8.28	0.770	8.36	0.719
RMS	1.51	0.195	1.52	0.178

These results indicate that at least six basis vectors are needed for critical applications calling for average colorimetric errors of  $\Delta E_{ab}^* \leq 1.0$ . They also show the limitation of the population variance measure,  $v$ , based on the eigenvalues. The fraction of population variance accounted for is high ( $> 99.7\%$ ) for  $p = 4$ , as shown in Table 2-1, however this analysis, is far from complete in terms of the spectral reconstruction or colorimetric coordinates.

### **D. Spectral Reconstruction From Camera Signals**

#### 1. Modified PCA

As discussed above, it is usually impractical to use PCA directly from multispectral camera signals. The technique can be modified, however, by computing a transformation that allows the camera signals to estimate the scalar weights for a given sample set and illuminant. A simple approach was applied to the digital camera-filter set system described earlier. This resulted in the derivation of a least-square matrix transformation of the camera signals. The matrix transforms the camera signals into estimates of the set of principal components,  $\hat{\alpha}$ , for the each color sample,

$$\hat{\alpha} = \mathbf{A} \mathbf{t} . \tag{2-7}$$

The matrix is calculated based on a set of camera signals (either modeled or actual) and the corresponding components, via the pseudo-inverse,

$$\mathbf{A} = \alpha \mathbf{t}^T [\mathbf{t} \mathbf{t}^T]^{-1} \tag{2-8}$$

where the rows of  $\alpha$  and  $\mathbf{t}$  correspond to the samples in the set of reflectance vectors. Note that a given matrix needs to be calculated for each sample set-illuminant combination, under this procedure. Figure 2-6 indicates the signal processing from camera to spectral reconstruction.

Note that, the basis vectors are orthogonal. The reconstruction error can always be reduced by using additional bases. Furthermore, a reconstruction based on the first  $n$  vectors is the minimum-rms error estimate based on any  $n$  vectors if they are included in order of decreasing eigenvalues. The matrix  $\mathbf{A}$  of Eq. (2-8) allows the *estimation* of the

principal components from the camera signals. Any  $n$  camera signals in general will not span the same signal-space as the first  $n$  orthogonal bases. Therefore there is no reason that the number of camera signals used should be equal to the number bases. Spectral reconstructions were successfully obtained, for example, using 7 signals and various numbers of bases, 5, 6,..12. The error was found to decrease as  $n$  increased, but with minor gains beyond 8.

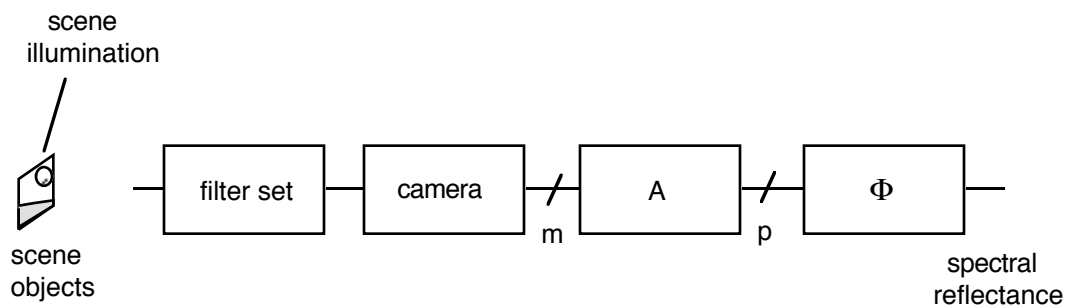


Fig. 2-6: Outline of the modified PCA spectral reconstruction from the digital camera.

The Munsell 37 data set was used to calculate a matrix  $\mathbf{A}$ , based on a simulation of the experimental camera and set of seven interference filters. The spectral power distribution of the incandescent light source used with the digital camera is shown with CIE illuminants  $\mathbf{A}$  and  $\mathbf{D}_{65}$  in Fig. 2-7. As expected, it matches illuminant  $\mathbf{A}$  closely.

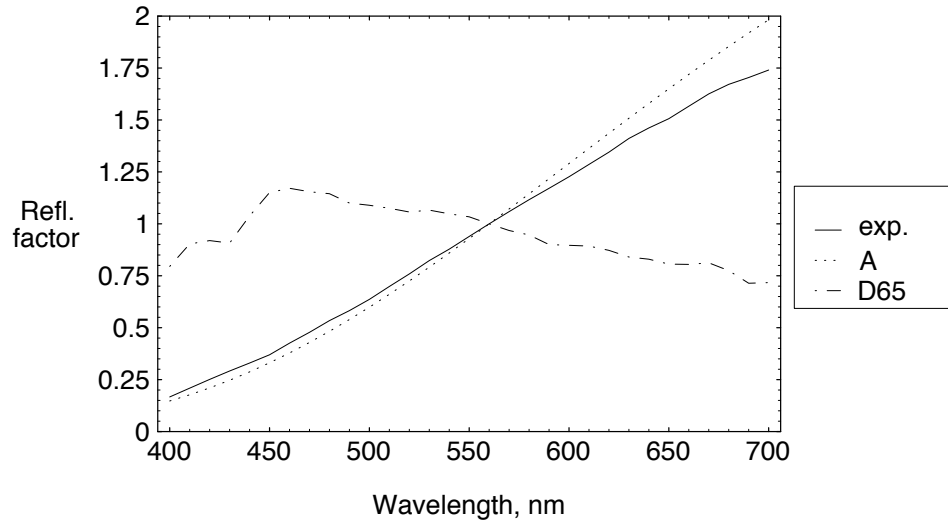


Fig. 2-7: Relative spectral power distributions for the incandescent light source used with the experimental camera (exp.), CIE illuminants A and  $D_{65}$ .

As in Eq. (2-1), the source spectral distribution was cascaded with the camera and filter sensitivity matrix,  $\mathbf{G}$ , which was shown in Fig. 2-2. This resulted in the simulated, or ideal, camera signals,  $\mathbf{t}$ , corresponding to the Munsell 37 sample set. The set of spectral 37 reflectance vectors were also analyzed using the basis vectors shown in Fig. 2-4. For each sample, the set of scalar weights,  $\alpha$ , (the principal components) were calculated via Eq. (2-6). Equation (2-7) was then used to derive the matrix  $\mathbf{A}$

$$\mathbf{A} = \begin{bmatrix} -0.7579 & -0.5856 & -1.886 & 1.38 & -3.483 & 1.924 & -2.067 \\ -0.545 & -1.527 & -1.426 & 1.348 & -0.4675 & 0.6137 & 1.475 \\ -1.231 & -0.4659 & 1.215 & 2.516 & -2.034 & 1.438 & -1.538 \\ -0.4061 & -0.7758 & 2.806 & -3.056 & 0.907 & -1.907 & 2.275 \\ 2.179 & -2.149 & -0.7936 & 3.416 & -2.914 & -0.6495 & 1.037 \\ -1.677 & 1.934 & -0.5267 & -2.14 & 6.097 & -6.505 & 2.672 \\ 1.273 & -2.109 & 2.98 & -6.528 & 8.254 & -4.445 & 0.6202 \\ -0.6452 & 1.182 & -1.992 & 4.808 & -6.465 & 3.797 & -0.6975 \end{bmatrix}, \quad (2-9)$$

where the 8 rows and 7 columns correspond to the basis vectors and camera signals, respectively. To test the utility of this procedure, the reflectance vector for each of the Munsell 37 samples was reconstructed by substituting Eq. (2-7) into Eq. (2-5)

$$\hat{\mathbf{r}}_i = \Phi_r \mathbf{A} \mathbf{t}_i$$

where  $\hat{\phantom{x}}$  indicates the estimate. The mean and rms spectral reflectance error are shown in Fig. 2-8.

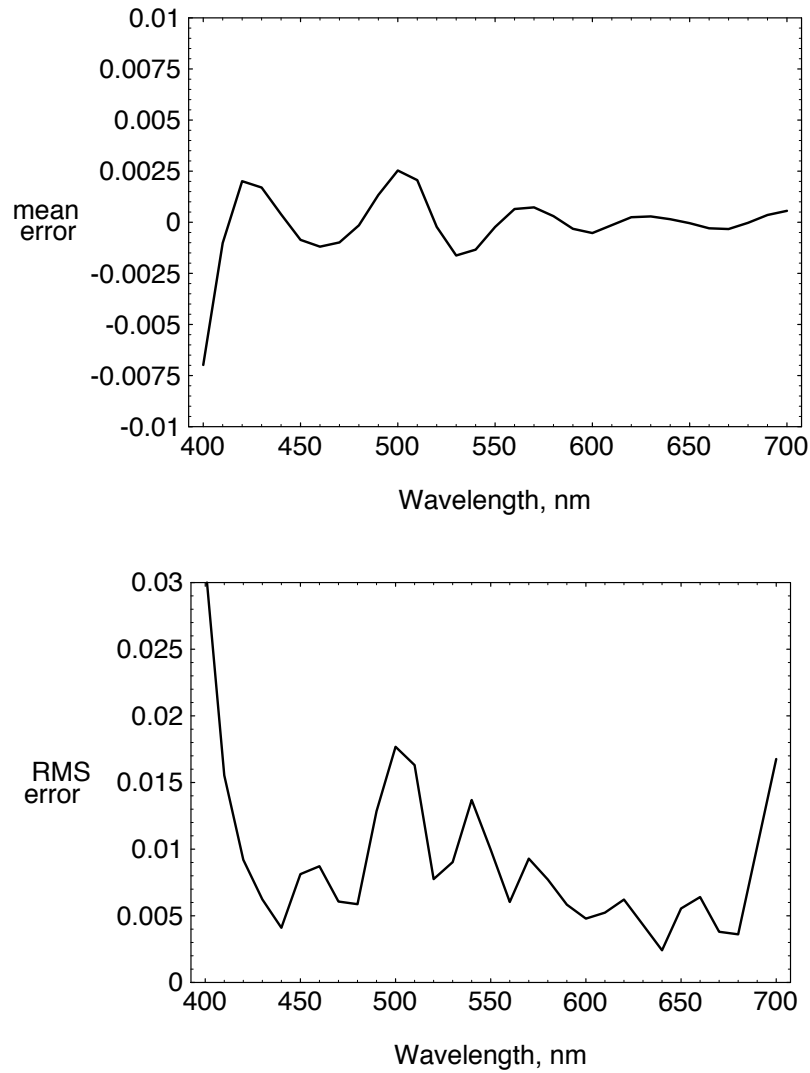


Fig. 2-8: The simulated mean and rms spectral reconstruction errors for the modified PCA method, and the Munsell 37 sample set. The spectral reflectance is on a [0-1] scale.

The CIELAB coordinates corresponding to the reconstructed vectors were then calculated. CIE illuminant  $D_{65}$  was chosen because the actual source distribution used for both the experimental and calculated image capture was significantly different than  $D_{65}$ , as shown in Fig. 2-7. Transformation from image capture under illuminant A to display under  $D_{65}$ , therefore, seemed a reasonable and challenging task. The color-difference errors are summarized in Table 2-3, with more details in Appendix B.

Table 2-3: Summary of CIELAB color-difference error,  $\Delta E_{ab}^*$ , following a simulation of multispectral image capture and signal processing, for the Munsell 37 set, CIE illuminant  $D_{65}$  and the  $10^\circ$  observer. The PCA reconstruction is for the 8 basic functions The simple direct model is based on Eq. (2-10) and the complex model includes the mixed second-order terms, as in Eq. (2-11). For more details see the text and Appendix B.

sample	mod. PCA	MDST	Spline	Direct models	
				simple	complex
mean	0.63	5.59	6.77	3.00	0.68
rms	0.57	4.33	5.13	2.13	0.70
max.	2.70	15.40	18.30	10.60	3.97

Comparing the results of Tables 2-2 and 2-3, it is concluded that the modified PCA technique can be successfully applied to actual multispectral camera signals. This method will now be compared with two interpolation methods that do not rely on the *a priori* description of the sample set in terms of a set of basis vectors.

## 2. MDST and Spline Interpolation

For the interference filter set used with the CCD camera, the transmittance curves have similar shape and are centered at approximately equal intervals in wavelength, as shown in

Fig. 2-2. This observation suggests that the multispectral image capture can be described as a spectral sampling problem. Image acquisition can be seen as analogous to the spectral scanning of the light reflected from the scene, followed by a sampling at approximately 50nm. Following this approach, two interpolation methods often applied to time series and other sampled signals are applied to the spectral reconstruction from camera signals.

The Modified Discrete Sine Transformation (MDST) (Keusen 1994, Praefcke and Keusen 1995) interpolation method has successfully been applied to the data-compression of spectral reflectance vectors. This technique relies on properties of the sine-transform (and Fourier transform) representations of the signal, and the steps are shown in Fig. 2-9. To avoid the introduction of errors due to circular convolution, or Gibbs phenomenon (Bendat and Piersol 1971), the input sequence is first separated into a linear fit and differential components, the latter of which is then subjected to the sine transform. This transformed sequence is extended with zero values, and then inverse transformed. An interpolated version of the differential signal is then extracted from the inverse transformed sequence, and added to the (interpolated) linear fit to the original data.

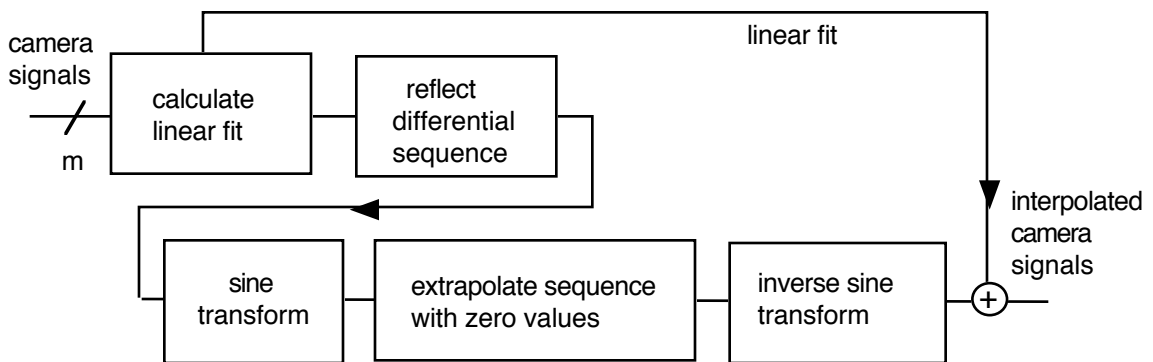


Fig. 2-9 The basic steps in the MDST interpolation method.

While this procedure yields a smooth interpolated signal, it will not escape from the limitations imposed by the original spectral sampling. In time series analysis and signal processing these errors are often called aliasing errors. To some extent these will be mitigated by the spectral smoothing of the filter response profile. The interpolated signals, however, will then also include the effect of this spectral smoothing, for which it is not possible to completely compensate, due to the low spectral sampling rate, 50nm. The results of applying the MDST method to the camera signals, for a single sample from the Munsell 37 set is shown in Fig. 2-10. Note the smooth nature of the interpolated signal, and the resultant higher errors in the rapidly varying parts of the sequence. A summary of the corresponding CIELAB color-difference errors, for CIE illuminant  $D_{65}$  and the  $10^\circ$  observer, are given in Table 2-3.

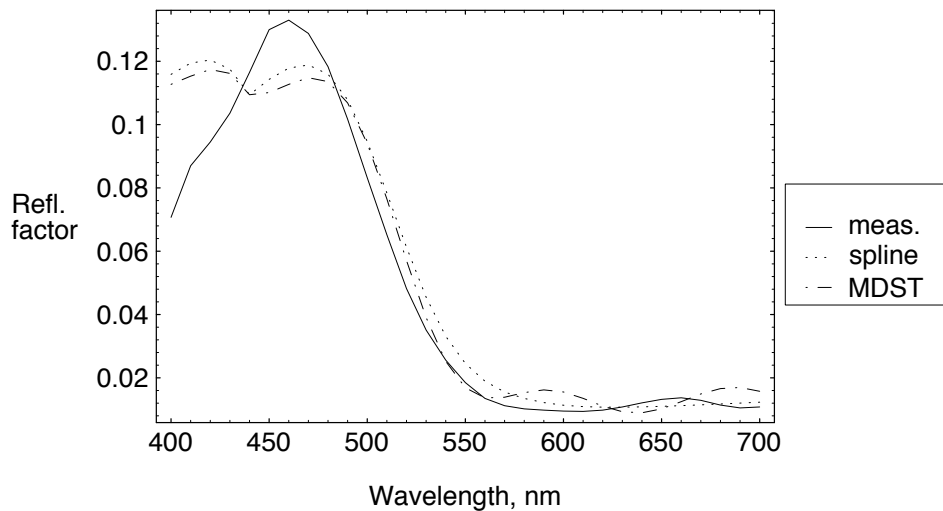


Fig. 2-10: MDST and cubic spline interpolation of simulated camera signals for a Munsell color sample, 5PB 5/10. The solid line is the measured spectral reflectance factor.

Cubic spline interpolation (Conte and de Boor 1972, Press *et al.* 1988) was also applied to the spectral reconstruction from camera signals. This technique is known for smooth interpolation of a sampled data and, like the MDST method, requires no prior description of the sample set. Figure 2-10 includes an example of cubic spline interpolation of camera signals for sample 5PB 5/10 comparison. This method is seen to yield similar results to those for the other interpolation method. This is also evident from the CIELAB errors summarized in Table 2-3., with more details given in Appendix B.

### 3. Direct Colorimetric Transformation

The use of spectral reconstruction as an intermediate toward a colorimetric image capture has been demonstrated above. For applications where the estimated reflectance vector is not needed, however, the use of a direct colorimetric transformation has been suggested (Hamber *et al.* 1993). Two forms of direct colorimetric transformation were investigated for the multispectral camera signals. The simple model can be written as

$$\begin{aligned}
 L^* &= \sum_{i=1}^m a_i (t_i)^{b_i} \\
 a^* &= \sum_{i=1}^m c_i (t_i)^{d_i} , \\
 b^* &= \sum_{i=1}^m e_i (t_i)^{f_i}
 \end{aligned}
 \tag{2-10}$$

where a, b, ...f are constants and  $t_1, t_2, \dots, t_m$  are the set of camera signals. The resulting least-square fit to this model, based on the CIELAB coordinates for the Munsell 37 set, CIE illuminant D<sub>65</sub> and the 10° observer is

$$\begin{bmatrix} L^* \\ a^* \\ b^* \end{bmatrix} = \begin{bmatrix} -52.4 & 79.5 & -3.04 & 132. & -135. & 95.9 & -16.2 \\ 102. & -89.3 & -160. & 114. & -111. & 155. & -8.65 \\ -214. & 38.3 & 48.1 & 137. & -78.3 & 47.6 & 20.7 \end{bmatrix} \begin{bmatrix} t_1^p \\ t_2^p \\ t_3^p \\ t_4^p \\ t_5^p \\ t_6^p \\ t_7^p \end{bmatrix}. \quad (2-11)$$

where the exponent p, corresponds to b = 0.430, d = 0.405 and f = 0.315 for  $L^*$ ,  $a^*$  and  $b^*$ , respectively. Given the nonlinear cube-root part of the CIELAB calculation from tristimulus values, these exponential values are not surprising. The results for this direct transformation for the Munsell 37 sample set can be compared with the other methods in Table 3-3 and in Appendix B. This direct transformation is seen to yield results lying between those for the modified PCA method, and the interpolation methods.

A second, more complex, model that included squared mixed-signal terms was also fit to the Munsell 37 data set. The model form is

$$\begin{bmatrix} L^* \\ a^* \\ b^* \end{bmatrix} = \mathbf{B} \begin{bmatrix} t_1^{1/3} \\ t_2^{1/3} \\ \vdots \\ t_7^{1/3} \\ t_1^{1/3} t_2^{1/3} \\ t_1^{1/3} t_3^{1/3} \\ \vdots \\ t_6^{1/3} t_7^{1/3} \end{bmatrix} \quad (2-12)$$

where the second-order elements of the left matrix include all of the signals taken two at a time, resulting in a total of 28 elements, and  $\mathbf{B}$  is a (3 x 28) matrix. The resulting least-

square fit to the Munsell 37 data set resulted in matrix of weights

$$\mathbf{B} = 100 \begin{bmatrix} -1.17 & 0.668 & -2.02 \\ 2.89 & -0.771 & -0.004 \\ -5.76 & -0.537 & 1.54 \\ 13.6 & -0.633 & -0.425 \\ -16.1 & -0.935 & 0.325 \\ 6.01 & 4.44 & 1.08 \\ 1.11 & -2.21 & -0.477 \\ 1.73 & 0.118 & 0.0211 \\ -27. & -8.97 & 2.12 \\ 116. & 41.5 & 2.46 \\ -199. & -42.2 & -4.16 \\ 186. & -26.5 & -10.7 \\ -73.3 & 34.4 & 10.8 \\ 24.9 & 15.9 & -1.71 \\ -129. & -83.8 & 0.135 \\ 221. & 118. & -10.8 \\ -222. & -14.8 & 32.7 \\ 97.7 & -32.5 & -20.7 \\ 21. & 22.5 & -3.91 \\ -17.4 & -91.5 & 33.4 \\ 40.3 & 78.8 & -55.9 \\ -33.2 & -20. & 25.4 \\ -40.8 & 68.2 & -26.1 \\ 85.6 & -155. & 71.8 \\ -68.2 & 110. & -43.7 \\ -58.5 & 76.4 & -30.3 \\ 115. & -132. & 38.5 \\ -39.2 & 40.7 & -9.52 \end{bmatrix}^T \tag{2.12b}$$

The application of this more complex quadratic model led to a reduced color-difference error, comparable to that for the modified PCA spectral reconstruction, as summarized in Table 2-3, and Appendix B.

## E. CONCLUSIONS

In this chapter a model multispectral camera and matrix-vector description of image capture have been described. These were then used to develop several approaches to the processing of the camera signals for spectral reconstruction. Interpolation methods were seen to yield poorer results than either the modified PCA method or the complex form of direct colorimetric transformation. Signal uncertainty, or noise, will now be introduced as it applies to multispectral color image capture.

### **III. THEORY: IMAGE NOISE ANALYSIS**

In the previous chapter a model for multispectral image acquisition was described, as were several signal processing methods for estimating the spectral reflectance factor and colorimetric coordinates of scene objects. The ideal image capture was characterized by a set of fixed spectral sensitivity functions (or vectors) associated with the filter set and camera combination. Any practical system, however, will also be subject to error in the form of variations in camera signal across the image or from day-to-day. In addition, any signal processing steps that follow image detection, such as spectral estimation, will influence both the amplitude and correlation of the error in the final image.

A multivariate error-propagation analysis is now presented, which describes how stochastic errors that originate at image detection are transformed as the image is processed. The analysis is generally applicable to multispectral image capture and transformation using  $m$  signals. This is illustrated by a detailed discussion of the signal path used for spectrophotometric colorimetry. A physical model that describes the noise characteristics of the detector is then introduced. This is then combined with the error-propagation in a computed example of three-channel image acquisition.

#### **A. Error Propagation Analysis**

Uncertainty or noise in a detected or recorded color signal can arise from many sources, e.g., detector dark current, exposure shot noise, calibration variation, or varying operating conditions. If a physical model of the system and its associated signal processing is available, the influence of various sources on system performance can be understood for

both color-measurement (Nimeroff 1953, 1957, 1966, Nimeroff *et al.* 1961, Lagutin 1987, Robertson 1967, Fairchild and Reniff 1991) and imaging applications (Dainty and Shaw 1974, Huck *et al.* 1985, Burns 1987a, 1990). This approach allows the comparison of design/technology choices in terms of system performance requirements, e.g., color error or signal-to-noise ratio. The case of general stochastic error sources which can be functions of exposure level, wavelength etc. is addressed.

Measurements of systematic error are often used to evaluate accuracy during system calibration. Methods of correcting for systematic measurement error due to spectral band-pass, wavelength scale and linearity (Stearns 1981, Stearns and Stearns 1988, Berns and Petersen 1988) have been reported. From a statistical point of view this type of error represents bias, since the mean signal is not equal to the true value.

To address system precision one needs a description of the origin and propagation of signal uncertainty (Papoulis 1965, Box *et al.* 1978, Wolter 1985, Taylor and Kuyatt 1993). This would, for example, allow the comparison of observed performance in a secondary color-space, such as CIELAB, with that limited by measurement error, or image detection, in an original camera-signal space. The magnitude of errors introduced by approximations to functional color-space transformations (Hung 1988, Kasson *et al.* 1995) could also be compared with intrinsic errors.

Several workers (Nimeroff 1953, 1957, 1966, Nimeroff *et al.* 1961, Lagutin 1987) have addressed error propagation from instrument reading to chromaticity coordinates. In addition, propagation of uncorrelated measurement errors in the nonlinear colorimetric transformations from tristimulus values to perceptual color spaces has also been described (Robertson 1967, Fairchild and Reniff 1991). Here the above analysis is extended to

include the effect of correlation between the uncertainty in related sets of color signals. As Nimeroff has shown, the correlation is needed when computing error ellipses for 2-dimensional color-space projections, such as chromaticity coordinates.

The analysis is given in a functional and matrix-vector notation, to aid in its broad application to color measurement, calibration and color-image processing. While this approach is now common in color modeling (Allen 1966, Jaaskelainen *et al.* 1990, Trussell 1991, Quiroga *et al.* 1994), it is rarely used in color-error propagation (Wolter 1985). Many previously published reports on the subject can be seen as special cases of the general approach taken here. The results are applied to several specific common transformations from spectrophotometric colorimetry and CIELAB color specification. In addition the influence of stochastic color errors on the average value of color-difference measures,  $\Delta E^*_{ab}$  and  $\Delta E^*_{94}$  is demonstrated.

### 1. Univariate Transformation

If a signal is subject to an error, a measurement or recorded image can be seen as a random variable. For example, if a signal value  $x$  is detected for a process or image whose true value is  $K$ , one can represent the set of measurements as

$$x = \mu_x + e_x$$

where  $e_x$  is a zero-mean random variable with a probability density function, corresponding variance,  $\sigma_x^2$ , and mean value,  $\mu_x$ . If  $x$  is an unbiased measurement of the physical process, then the mean value is equal to  $K$ . If the original signal is transformed

$$y = f(x) ,$$

then  $y$  will also be a random variable. If  $f(x)$  and its derivatives are continuous, the statistical moments of  $y$  can be approximated in terms of the original moments,  $\mu_x$ ,  $\sigma_x^2$ , and  $f(x)$ . This is done by expanding the function in a Taylor series about the mean value,  $\mu_x$ , and expressing the first and second moments of  $y$  in terms of those of  $x$ . The mean value of  $y$  is given by (Papoulis 1965a, Box *et al.* 1978)

$$\mu_y = E[f(x)] \cong f(\mu_x) + \frac{1}{2} [f''_{xx} \sigma_x^2] \quad (3-1)$$

where  $E[.]$  is the statistical expectation and

$$f''_{xx} = \left. \frac{\partial^2 f(x)}{\partial x^2} \right|_{\mu_x} .$$

Equation (3-1) indicates that the expected value of  $f(x)$  is equal to the function evaluated at its mean value, but with the addition of a bias which is the product of the second derivative of  $f$  and the variance of  $x$ . For many applications the second, bias, term is small compared to the first. This assumption will be adopted, except as noted.

An expression for the variance of  $y$  can be similarly found. Following this approach (Papoulis 1965a, Box *et al.* 1978, Wolter 1985, Taylor and Kuyatt 1993), it can be shown that

$$\sigma_y^2 \cong f_x'^2 \sigma_x^2 + \frac{f_{xx}''^2}{4} (E[(x - \mu_x)^4] - \sigma_x^4), \quad (3-2)$$

where  $f_x'$  is the first derivative of  $f$  with respect to  $x$  evaluated at  $\mu_x$ . If  $x$  is, or can be approximated by, a normal random variable then  $E[(x - \mu_x)^4] = 3\sigma_x^4$  and Eq. (3-2) becomes

$$\sigma_y^2 \cong f_x'^2 \sigma_x^2 + \frac{f_{xx}''^2}{2} \sigma_x^4. \quad (3-3)$$

The usual expression for  $\sigma_y^2$  includes only the first term of the RHS of the previous equations (3-2) and (3-3),

$$\sigma_y^2 \cong f_x'^2 \sigma_x^2. \quad (3-4)$$

In most cases relevant to color-measurement and color-image processing this term is the dominant one, but there may be mean values for which this is not a good approximation. Equation (3-4) will be assumed unless stated otherwise. This shows that for a univariate transformation, the signal variance is scaled by the square of the first derivative of the function, evaluated at the mean value.

## 2. Multivariate Linear Transformation

A common color-signal transformation is a matrix operation, e.g.,

$$\mathbf{y} = \mathbf{A} \mathbf{x},$$

where a set of  $n$  input signals  $\{x\}$  is written as  $\mathbf{x} = [x_1 \ x_2 \ \cdots \ x_n]^T$  and the output is  $\mathbf{y}^T = [y_1 \ y_2 \ \cdots \ y_m]$ . The superscript, T, indicates matrix transpose, and  $\mathbf{A}$  is the  $(m \times n)$  matrix of weights. If each member of the set  $\{x\}$  is a random variable, the second-order moments can be written as a covariance matrix;

$$\Sigma_x = \begin{bmatrix} \sigma_{11} & \sigma_{12} & \cdots & \sigma_{1n} \\ \sigma_{21} & \sigma_{22} & \cdots & \\ \vdots & & \ddots & \\ \sigma_{n1} & & & \sigma_{nn} \end{bmatrix}$$

where  $\sigma_{11} \equiv \sigma_{x_1}^2$ , and the covariance between  $x_1$  and  $x_2$  is  $\sigma_{12}$ . If the set of signals  $\{x\}$  are statistically independent then  $\Sigma_x$  is diagonal. The resulting covariance matrix for  $y$ , from multivariate statistics (Wolter 1985, Johnson and Wichern 1992) is given by

$$\Sigma_y = \mathbf{A} \Sigma_x \mathbf{A}^T. \quad (3.5)$$

Equation (3-5) can also be written as an equivalent set of linear equations. For example, Wysecki and Stiles (1982) address such matrix transformations and their effect on color-matching ellipsoids.

### 3. Multivariate Nonlinear Transformation

When multivariate signals are transformed and combined, the resulting transformation of the covariance matrix can be seen as a combination of the above two cases. Starting with

a set of input signals with covariance matrix,  $\Sigma_x$ , each of the signals is transformed

$$\begin{aligned} y_1 &= f_1(x_1, x_2, \dots, x_n) \\ y_2 &= f_2(x_1, x_2, \dots, x_n) \\ &\vdots \\ & \end{aligned} , \quad (3-6)$$

where  $f$  may represent a compensation for detector response, or a nonlinear transformation between color spaces. Let the matrix derivative operator be

$$\mathbf{J}_{f(x)} = \begin{bmatrix} \frac{\partial y_1}{\partial x_1} & \frac{\partial y_1}{\partial x_2} & \dots & \frac{\partial y_1}{\partial x_n} \\ \frac{\partial y_2}{\partial x_1} & \ddots & & \\ \vdots & & \ddots & \\ \frac{\partial y_n}{\partial x_1} & & & \frac{\partial y_n}{\partial x_n} \end{bmatrix} ,$$

where each element of  $\mathbf{J}_{f(x)}$  is evaluated at the mean,  $(\mu_{x_1}, \mu_{x_2}, \dots, \mu_{x_n})$ . This notation is that of Sluban and Nobbs (1995), and this operator is the Jacobian matrix (Searle 1982).

The transformation of the covariance matrix due to Eq. (3.6) is given by (Wolter 1985)

$$\Sigma_y \cong \mathbf{J}_{f(x)} \Sigma_x \mathbf{J}_{f(x)}^T . \quad (3-7)$$

Equation (3-7) can also be written (Taylor and Kuyatt 1993)

$$\sigma_{y_i} \cong \sum_{j=1}^n \left( \frac{\partial f_i}{\partial x_j} \right)^2 \sigma_{x_{jj}} + 2 \sum_{j=1}^{n-1} \sum_{k=j+1}^n \frac{\partial f_i}{\partial x_j} \frac{\partial f_i}{\partial x_k} \sigma_{x_{jk}} ,$$

which is the form most often used. Note that the simpler univariate and matrix results of Eqs. (3-4) and (3-5) are special cases of Eq. (3-7).

Many color-signal transformations can be seen as a cascading of the above types of transformations. This will now be demonstrated by developing specific expressions for error propagation from spectral reflectance data to tristimulus values. This is followed by the transformation to CIELAB coordinates. These are important and common transformations, but can also be prototypes for image processing steps found in many electronic imaging systems.

#### 4. Spectrophotometric Colorimetry

A fundamental color transformation is that between instrument spectral measurement data and the corresponding colorimetric coordinates. If one is using a spectrophotometer, this involves measuring the spectral reflectance factor at several wavelengths over the visible range. These are weighted with an illuminant spectral power distribution, and combined in the form of the three tristimulus values. Often these data are then transformed into a perceptual color space such as CIELAB or CIELUV. The following analysis addresses noise propagation through this signal-processing path.

##### *a. Error in Tristimulus Values*

The tristimulus values are calculated by multiplying the measured sample spectral

reflectance factor by a CIE illuminant and color matching function weighting at each wavelength. A summation of the result yields the three tristimulus values. For the first tristimulus value this is expressed as,

$$X = k \Delta\lambda \sum_{j=1}^{jmax} s_j \bar{x}_j R_j$$

where  $\bar{x}_j$  is the first CIE color matching function,  $s$  is the illuminant spectral power distribution,  $\Delta\lambda$  is the wavelength sampling interval,  $R$  is the sampled spectral reflectance factor, and  $k$  is a normalizing constant.

The calculation of the tristimulus values can be expressed in matrix notation,

$$\mathbf{t} = k \Delta\lambda \mathbf{M}^T \mathbf{S} \mathbf{r} \quad (3-8)$$

where

$$\mathbf{t} = \begin{bmatrix} X \\ Y \\ Z \end{bmatrix}, \quad \mathbf{S} = \begin{bmatrix} s_1 & & 0 \\ & s_2 & \\ & & \ddots \\ 0 & & & s_n \end{bmatrix}, \quad \mathbf{r} = \begin{bmatrix} R_1 \\ R_2 \\ \vdots \\ R_n \end{bmatrix},$$

and  $\mathbf{M}$ , comprises the CIE color matching functions,

$$\mathbf{M} = \begin{bmatrix} \bar{x}_1 & \bar{y}_1 & \bar{z}_1 \\ \vdots & \vdots & \vdots \\ \bar{x}_n & \bar{y}_n & \bar{z}_n \end{bmatrix}.$$

Often Eq. (3-8) is implemented using ASTM weights (ASTM 1990) that combine the illuminant and color matching function information,

$$\mathbf{t} = \mathbf{M}^T \mathbf{r} \quad (3-9)$$

where  $\mathbf{M}$  now indicates the weight matrix for a specified CIE illuminant and observer.

The fact that the three color matching functions overlap at various wavelengths introduces correlation into the error associated with the tristimulus elements of  $\mathbf{t}$  (Nimeroff 1953). If  $\mathbf{t}$  is calculated as in Eq. (3-9), then the resulting covariance matrix is given as in Eq. (3-5)

$$\Sigma_{\mathbf{t}} = \mathbf{M}^T \Sigma_{\mathbf{r}} \mathbf{M} . \quad (3-10)$$

where  $\Sigma_{\mathbf{r}}$  is the (n x n) spectral-reflectance covariance matrix. If the CIE color matching functions, and ASTM weights, did not overlap this result would revert to the uncorrelated error case. Note that, since the covariance matrix comprises the moments about the mean values of  $X, Y, Z$ , a constant bias error in  $\{r\}$  has no effect on  $\Sigma_{\mathbf{t}}$ .

Assuming uncorrelated instrument errors, one can assess the effect of the overlapping color matching functions alone on colorimetric error correlation. In this case the instrument error covariance matrix,  $\Sigma_{\mathbf{r}}$ , is diagonal. To more easily identify correlation introduced by the overlapping color matching functions, consider the special case of uncorrelated and equal instrument error whose covariance matrix is

$$\Sigma_{\mathbf{r}} = \sigma_{\mathbf{r}}^2 \mathbf{I} \quad (3-11)$$

where  $\mathbf{I}$  is the diagonal identity matrix. This case could be used to model simple dark current error, or that due to quantization rounding. The resulting tristimulus-vector covariance matrix,  $\Sigma_{\mathbf{t}}$ , is found by substituting Eq. (3-11) into Eq. (3-10)

$$\Sigma_{\mathbf{t}} = \sigma_{\mathbf{f}}^2 \mathbf{M}^T \mathbf{M}. \quad (3-12)$$

As an example, consider the case of the CIE illuminant A for the 10° observer, whose weights are plotted in Fig. 3-1. The tristimulus matrix that would result from uncorrelated instrument spectral reflectance error is calculated from Eq. (3-12)

$$\Sigma_{\mathbf{t}} = \sigma_{\mathbf{f}}^2 \begin{bmatrix} 0.095 & 0.067 & 0.003 \\ 0.067 & 0.069 & 0.002 \\ 0.003 & 0.002 & 0.015 \end{bmatrix}$$

where the diagonal elements represent the variance of the error associated with the tristimulus values, X, Y, and Z. The corresponding correlation matrix is

$$\mathbf{R}_{\mathbf{t}} = \begin{bmatrix} 1 & 0.826 & 0.071 \\ 0.826 & 1 & 0.069 \\ 0.071 & 0.069 & 1 \end{bmatrix}$$

Thus, there is a correlation coefficient,  $r_{xy} = 0.826$  between X and Y values, due to the overlapping weights.

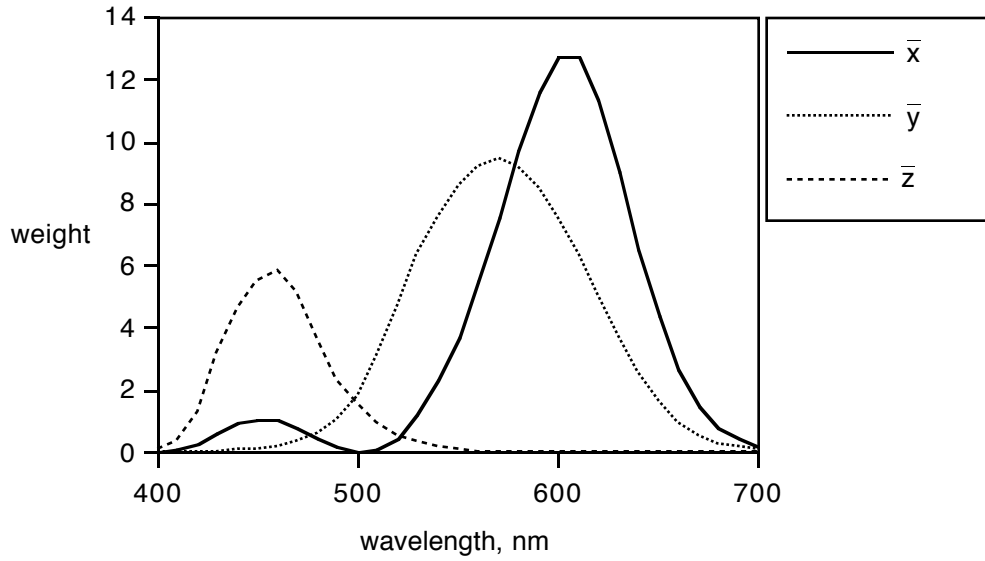


Fig. 3-1: ASTM, 10 nm weights for CIE illuminant A and the 10° observer.

*b. CIELAB Errors*

CIELAB coordinates,  $L^*$ ,  $a^*$ , and  $b^*$ , are calculated from the tristimulus values, and those of a white object color stimulus (CIE 1986) whose tristimulus values are  $X_n$ ,  $Y_n$ ,  $Z_n$ .

For example,  $L^*$  is given by

$$L^* = 116 f(Y) - 16 \quad (3.13a)$$

where

$$f(Y) = \left(\frac{Y}{Y_n}\right)^{1/3} \quad \text{for } Y/Y_n > 0.008856 \quad (3.13b)$$

$$f(Y) = 7.787 \frac{Y}{Y_n} + \frac{16}{116}, \quad \text{for } Y/Y_n \leq 0.008856$$

This indicates that  $L^*$  can be computed by first evaluating the nonlinear function Eq. (3-13b) and then the linear operation Eq. (3-13a).

The variance of the error in  $f(Y)$  can be approximated as,

$$\begin{aligned}\sigma_{f(Y)}^2 &\cong \left( \frac{df(Y)}{dY} \right)^2 \sigma_Y^2 \\ &\cong \left( \frac{1}{3\mu_Y^{2/3} Y_n^{1/3}} \right)^2 \sigma_Y^2 \quad \text{for } \mu_Y/Y_n > 0.008856 \quad (3-14) \\ &\cong \left( \frac{7.787}{Y_n} \right)^2 \sigma_Y^2 \quad \text{for } \mu_Y/Y_n \leq 0.008856 .\end{aligned}$$

Here it is assumed that  $Y_n$  is a constant, but if errors between laboratories or over time are important, then the measurement of the white object color stimulus can be a significant source of stochastic error (Fairchild and Reniff 1991). In addition, the measured value of  $Y_n$  can introduce a bias error into all CIELAB values that are based on the measurement. Equation (3-14) represents one element of the matrix operation of Eq. (3-7)

$$\Sigma_{f(\mathbf{t})} \cong \mathbf{J}_{f(\mathbf{t})} \Sigma_{\mathbf{t}} \mathbf{J}_{f(\mathbf{t})}^T$$

where, for  $\mu_X, \mu_Y, \mu_Z > 0.008856Y_n$ ,

$$\mathbf{J}_{f(\mathbf{t})} = \frac{1}{3} \begin{bmatrix} \mu_X^{-2/3} X_n^{-1/3} & 0 & 0 \\ 0 & \mu_Y^{-2/3} Y_n^{-1/3} & 0 \\ 0 & 0 & \mu_Z^{-2/3} Z_n^{-1/3} \end{bmatrix} .$$

As stated previously, the error-propagation techniques used here only apply strictly to continuous functions with continuous derivatives. Clearly  $f(Y)$  and its derivative functions are not continuous near  $Y = 0.008856$ , but evaluation of the function indicates that both  $f(Y)$  and  $df(Y)/dY$  are approximately continuous, to the limit imposed by the four digits of the constant 903.3. The second derivative function is discontinuous and error propagation analysis that includes this function could include verification of the error statistics in this region by direct simulation.

The corresponding calculations of  $a^*$  and  $b^*$  have a similar nonlinear first step and subsequent second step. The transformation to CIELAB can be expressed in matrix notation,

$$\begin{bmatrix} L^* \\ a^* \\ b^* \end{bmatrix} = \begin{bmatrix} 0 & 116 & 0 \\ 500 & -500 & 0 \\ 0 & 200 & -200 \end{bmatrix} \begin{bmatrix} f(X) \\ f(Y) \\ f(Z) \end{bmatrix} + \begin{bmatrix} -16 \\ 0 \\ 0 \end{bmatrix} \quad (3-15)$$

or

$$\mathbf{c} = \mathbf{N} \mathbf{f}(\mathbf{t}) + \mathbf{n}.$$

where  $\mathbf{c}$  is the CIELAB vector,  $\mathbf{f}(\mathbf{t})$  represents the three univariate transformations, and  $\mathbf{N}$  and  $\mathbf{n}$  are the corresponding matrix and vector from Eq. (3-15). The covariance matrix for the error in the CIELAB values is given by,

$$\Sigma_{L^*a^*b^*} \equiv \mathbf{N} \Sigma_{f(\mathbf{t})} \mathbf{N}^T = \mathbf{N} \mathbf{J}_{f(\mathbf{t})} \Sigma_{\mathbf{t}} \mathbf{J}_{f(\mathbf{t})}^T \mathbf{N}^T. \quad (3-16)$$

*c. CIELAB Chroma and Hue*

In addition to distances in  $L^*$ ,  $a^*$ ,  $b^*$  space, visual color differences can also be expressed in the rotated rectangular differences in lightness, chroma, and hue,  $\Delta L^*$ ,  $\Delta C_{ab}^*$ ,  $\Delta H_{ab}^*$  (CIE 1986). To express the covariance description of errors in  $L^*$ ,  $a^*$ ,  $b^*$  in terms of their transformed statistics,  $\Sigma_{\Delta L^* \Delta C_{ab}^* \Delta H_{ab}^*}$ , first consider the transformation to lightness, chroma and hue angle,  $h_{ab}$ . The chroma is

$$C_{ab}^* = \sqrt{a^{*2} + b^{*2}}$$

and the hue angle,

$$h_{ab} = \tan^{-1}\left(\frac{b^*}{a^*}\right).$$

One can again apply Eq. (3-7),

$$\mathbf{J}_{L^* C_{ab}^* h_{ab}} = \begin{bmatrix} 1 & 0 & 0 \\ 0 & \frac{\mu_{a^*}}{\mu_{C_{ab}^*}} & \frac{\mu_{b^*}}{\mu_{C_{ab}^*}} \\ 0 & -\frac{\mu_{b^*}}{\mu_{C_{ab}^*}^2} & \frac{\mu_{a^*}}{\mu_{C_{ab}^*}^2} \end{bmatrix},$$

where  $\mu_{C_{ab}^*} = \sqrt{\mu_{a^*}^2 + \mu_{b^*}^2}$ , and

$$\Sigma_{L^* C_{ab}^* h_{ab}} \cong \mathbf{J}_{L^* C_{ab}^* h_{ab}} \Sigma_{L^* a^* b^*} \mathbf{J}_{L^* C_{ab}^* h_{ab}}^T. \quad (3-17)$$

The hue difference between two color samples is given by

$$\Delta H_{ab}^* = 2\sqrt{C_{ab_1}^* C_{ab_2}^*} \sin\left(\frac{\Delta h_{ab}}{2}\right), \quad (3-18)$$

where  $C_{ab_1}^*$  and  $C_{ab_2}^*$  are the two chroma values and  $\Delta h_{ab}$  is the hue-angle difference. To find the covariance matrix for the color-difference values,  $\Delta L^*$ ,  $\Delta C_{ab}^*$ ,  $\Delta H_{ab}^*$ , only involves the additional transformation from  $\Delta h_{ab}$  to  $\Delta H_{ab}^*$ . Since hue differences about the mean are being addressed, the reference  $C_{ab_1}^* = \mu_{C_{ab}^*}$  and  $C_{ab_2}^*$  of Eq. (3-18) is taken as the ensemble of chroma values. Assuming small angles,  $\Delta h_{ab}$ , then

$$\Delta H_{ab}^* \approx \Delta h_{ab} \sqrt{\mu_{C_{ab}^*} C_{ab_2}^*},$$

so

$$\mathbf{J}_{L^*, C_{ab}^*, H_{ab}^*} = \begin{bmatrix} 1 & 0 & 0 \\ 0 & 1 & 0 \\ 0 & 0 & \mu_{C_{ab}^*} \end{bmatrix},$$

$$\Sigma_{\Delta L^* \Delta C_{ab}^* \Delta H_{ab}^*} \cong \mathbf{J}_{\Delta L^* \Delta C_{ab}^* \Delta H_{ab}^*} \Sigma_{L^* \Delta C_{ab}^* h_{ab}} \mathbf{J}_{\Delta L^* \Delta C_{ab}^* \Delta H_{ab}^*}^T. \quad (3-19)$$

The use of the above analysis will now be shown in a computed example of colorimetric error propagation.

### 5. Computed Example For Colorimeter/Camera

Consider a tristimulus-filter colorimeter whose three spectral sensitivities are the CIE color matching functions. The instrument, therefore, measures the sample tristimulus values directly. Let us also assume the signal includes a random error whose rms value is 0.5% of full scale, *i.e.*, 0.005. This error is uncorrelated between the  $X$ ,  $Y$ , and  $Z$  signals. The variance of each signal is given by  $(0.005)^2$  where the signal range is [0-1], or  $\Sigma_t = 2.5 \times 10^{-5} \mathbf{I}$ .

If the CIELAB coordinates are computed from the measured data, the corresponding errors will be a function of the (mean) signals as in Eq. (3-14). As an example, let the true color tristimulus values be  $X/X_n = 0.55$ ,  $Y/Y_n = 0.5$ , and  $Z/Z_n = 0.05$ , corresponding to a strong orange yellow. These values are on a [0-1] scale. Assuming that the measurement errors are described or approximated by normal probability distributions, then the three-dimensional, 95% probability error ellipsoid is shown in Fig. 3-2. This is derived from the eigenvectors and eigenvalues of the covariance matrix, as is commonly done in multivariate statistics (Johnson and Wichern 1992). The ellipsoid represents a three-dimensional analog of the univariate 95% confidence interval about the mean, for the population of measurements  $\{X, Y, Z\}$  whose variation is described by the covariance matrix  $\Sigma_t$ . The spherical shape is due to the independent and equal-variance nature of the errors for the three signals.

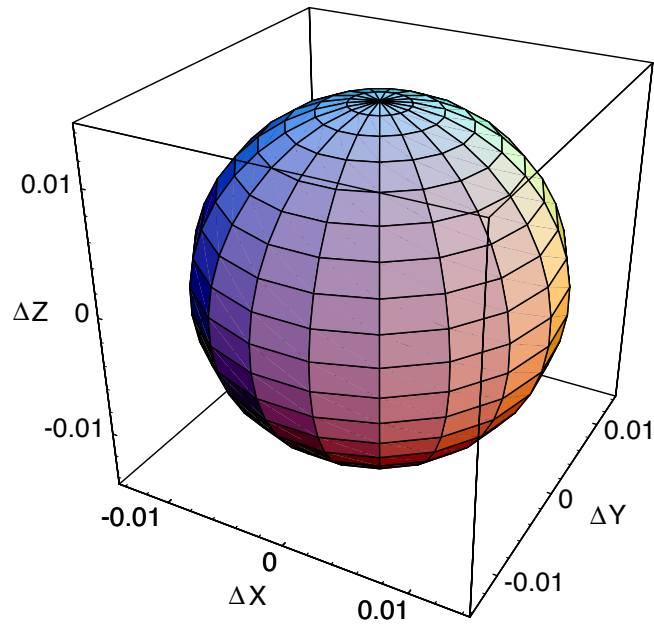


Fig. 3.2: Error ellipsoid (95%) for the measured tristimulus values example.

In applying Eq. (3-14b) for each tristimulus value,

$$f'_X(0.55) = 0.496, f'_Y(0.5) = 0.529, f'_Z(0.05) = 2.46 .$$

Using Eq. (3-16) the covariance matrix of the errors in the CIELAB coordinates is,

$$\Sigma_{L^*a^*b^*} = \begin{bmatrix} 0.094 & -0.406 & 0.162 \\ & 3.291 & -0.700 \\ & & 6.312 \end{bmatrix},$$

where the high value of  $\sigma_{b^*}^2$  is due to the high value of the derivative,  $f'_Z(0.05)$ , and large

coefficients of third row of matrix  $\mathbf{N}$ . The corresponding correlation matrix is,

$$\mathbf{R}_{L^*a^*b^*} = \begin{bmatrix} 1 & -0.729 & 0.211 \\ & 1 & -0.154 \\ & & 1 \end{bmatrix}.$$

Figure 3-3 shows the three projections of the 95% confidence ellipsoid that results from the propagation of the uncorrelated instrument error to CIELAB. The influence of the relatively high  $\sigma_{a^*}^2$  value, compared to  $\sigma_{L^*}^2$ , is seen in the highly elliptical shapes for this example. The corresponding three-dimensional plot for the CIELAB errors is shown in Fig. 3-4.

The square roots of the diagonal elements of the covariance matrix give the rms deviations for the CIELAB signals. These are listed in Table 3-1. The common color-difference metric,  $\Delta E_{ab}^*$  (CIE 1986) is the Euclidian distance

$$\Delta E_{ab}^* = \sqrt{\Delta L^{*2} + \Delta a^{*2} + \Delta b^{*2}}.$$

The expected value of  $\Delta E_{ab}^*$  can be approximated as shown in Appendix I,

$$E[\Delta E_{ab}^*] \approx \sqrt{\sigma_{L^*}^2 + \sigma_{a^*}^2 + \sigma_{b^*}^2} - \frac{\sigma_p^2}{8(\sigma_{L^*}^2 + \sigma_{a^*}^2 + \sigma_{b^*}^2)^{3/2}}, \quad (3.20)$$

where

$$\sigma_p^2 = 2(\sigma_{L^*}^4 + \sigma_{a^*}^4 + \sigma_{b^*}^4) - 4((\sigma_{L^*a^*})^2 + (\sigma_{L^*b^*})^2 + (\sigma_{a^*b^*})^2).$$

and was found to be equal to 2.79 for this computed example.

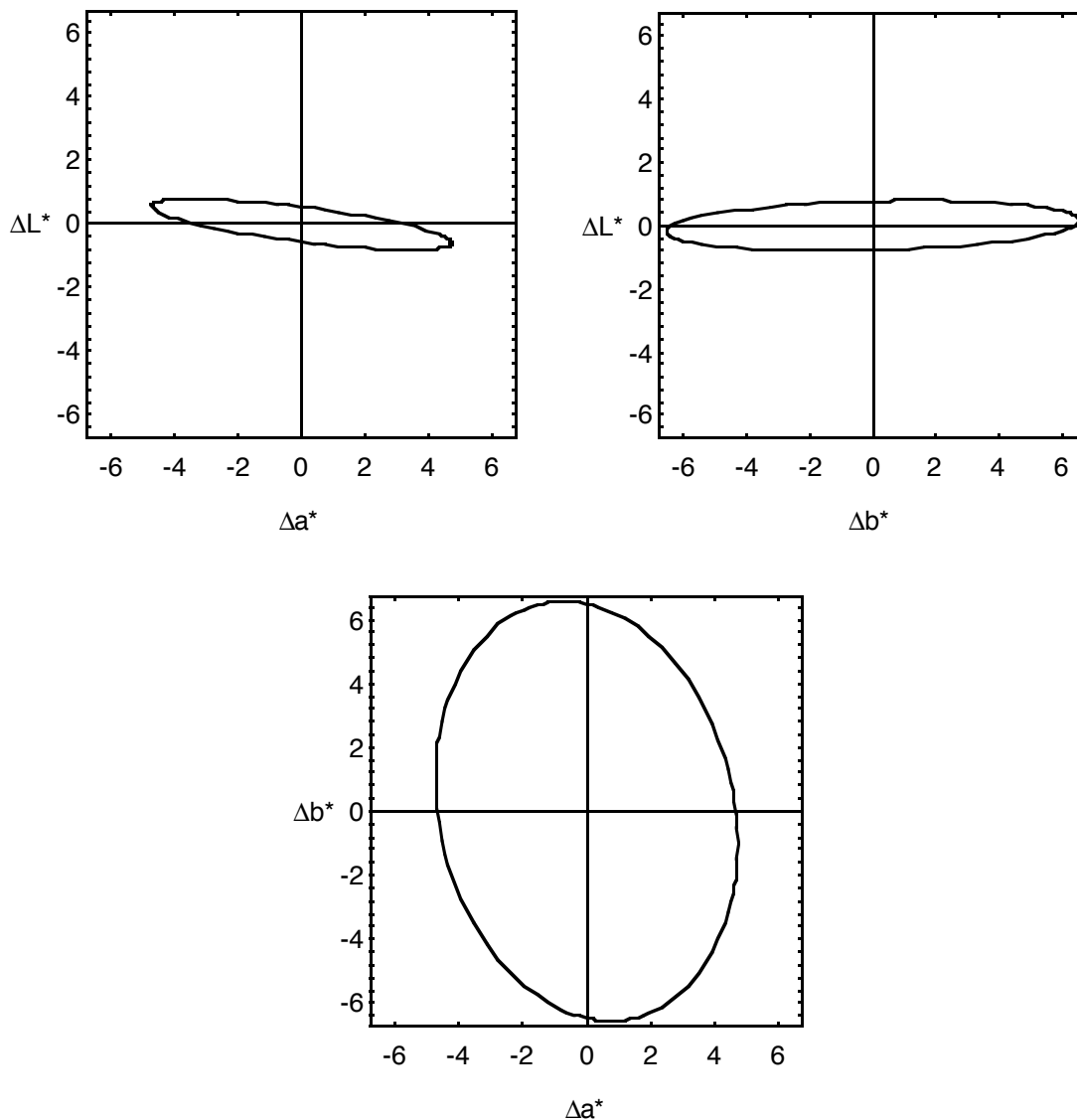


Fig. 3-3: The three projections of the CIELAB error ellipsoid (95% confidence) for the example.

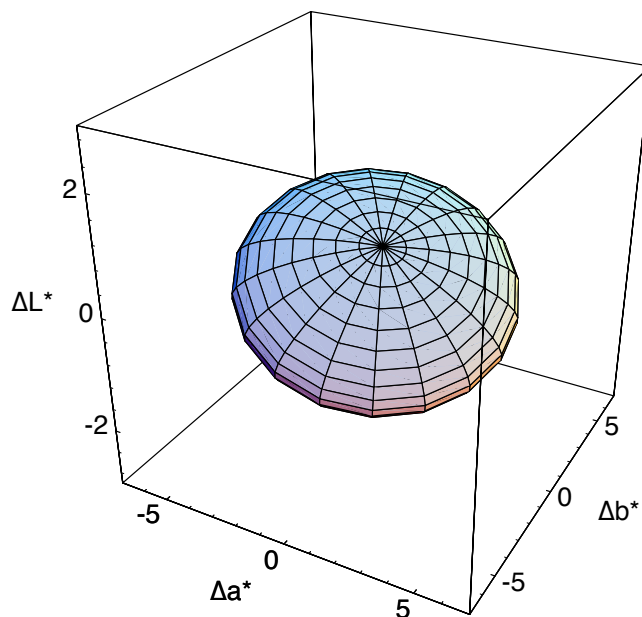


Fig.3-4 :  $L^*$ ,  $a^*$ ,  $b^*$  error ellipsoid about the mean (95% confidence) for the example.

The square roots of the diagonal elements of the covariance matrix give the rms deviations for the CIELAB signals. These are listed in Table 3-1. The common color-difference metric,  $\Delta E_{ab}^*$  (CIE 1986) is the Euclidian distance

$$\Delta E_{ab}^* = \sqrt{\Delta L^{*2} + \Delta a^{*2} + \Delta b^{*2}} .$$

The expected value of  $\Delta E_{ab}^*$  can be approximated as shown in Appendix B,

$$E[\Delta E_{ab}^*] \approx \sqrt{\sigma_{L^*}^2 + \sigma_{a^*}^2 + \sigma_{b^*}^2} - \frac{\sigma_p^2}{8(\sigma_{L^*}^2 + \sigma_{a^*}^2 + \sigma_{b^*}^2)^{3/2}} , \quad (3-20)$$

where

$$\sigma_p^2 = 2(\sigma_{L^*}^4 + \sigma_{a^*}^4 + \sigma_{b^*}^4) - 4((\sigma_{L^*a^*})^2 + (\sigma_{L^*b^*})^2 + (\sigma_{a^*b^*})^2).$$

and was found to be equal to 2.79 for this computed example.

Table 3-1: CIELAB values and rms error for the example signal.

CIELAB Coordinates	mean	standard deviation
L*	76.07	0.31
a*	12.81	1.81
b*	85.06	2.51

Note that Eq. (3-20) can be interpreted as describing the  $\Delta E_{ab}^*$  bias due to variations in  $L^*$ ,  $a^*$ , and  $b^*$ . In the absence of signal variation,  $\Sigma_{L^* a^* b^*} = 0$ , and therefore  $\Delta E_{ab}^* = 0$ . This is consistent with taking the ‘true’ CIELAB coordinate to be  $\{\mu_{L^*}, \mu_{a^*}, \mu_{b^*}\}$  for the zero-mean error case considered in this example.

Following Eqs. (3-17) and (3-19), the covariance matrix for the  $\Delta L^*$ ,  $\Delta C_{ab}^*$ ,  $\Delta H_{ab}^*$  error representation is

$$\Sigma_{\Delta L^* \Delta C_{ab}^* \Delta H_{ab}^*} = \begin{bmatrix} 0.094 & 0.100 & 0.426 \\ & 6.039 & 1.114 \\ & & 3.564 \end{bmatrix}. \quad (3-21)$$

This results in the error ellipsoid shown in Fig. 3-5.

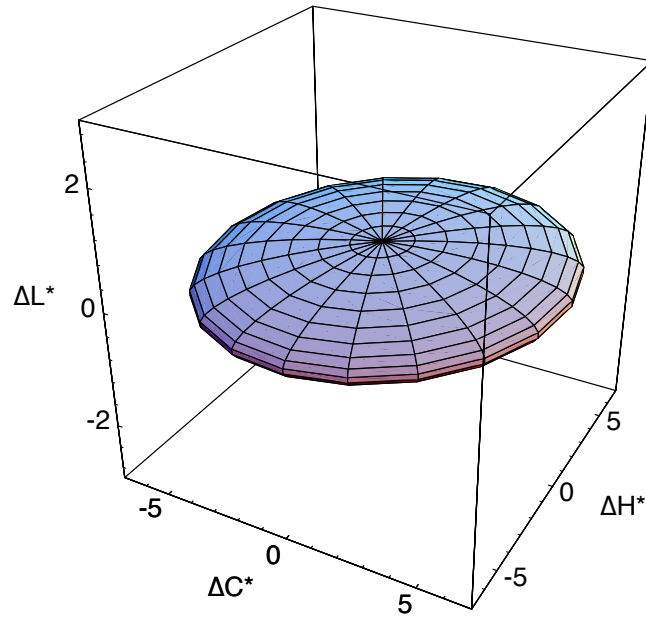


Fig.3-5:  $\Delta L^*$ ,  $\Delta C_{ab}^*$ ,  $\Delta H_{ab}^*$  error ellipsoid for the example color. Note unequal axes scales.

The rms  $\Delta L^*$ ,  $\Delta C_{ab}^*$ ,  $\Delta H_{ab}^*$  deviations for these signals are given in Table 3-2. The values for each signal should be interpreted in terms of the units of each. For example  $C_{ab}^*$ , chroma, is in units of CIELAB distance projected onto the  $a^*-b^*$  plane. Hue angle,  $h_{ab}$ , however, is in degrees.

Table 3-2:  $L^*$ ,  $C_{ab}^*$ ,  $\Delta H_{ab}^*$  values and rms error for the example signal. The values of the fourth column have been scaled to conform to the  $\Delta E_{94}^*$  color-difference measure.

CIELAB Coordinates	mean	standard deviation	scaled standard dev.
$L^*$	76.07	0.31	0.31
$C_{ab}^*$	86.02	2.46	0.51
$h_{ab}^*$	81.4°	-	-
$\Delta H_{ab}^*$	-	1.89	0.82
$\Delta E_{ab}^*$	2.79	-	-
$\Delta E_{94}^*$	0.89	-	-

a.  $\Delta E_{94}^*$  Color-difference Measure

Recently (CIE 1995) the CIE adopted the  $\Delta E_{94}^*$  color-difference measure, designed to overcome some limitations of  $\Delta E_{ab}^*$ . Specifically, the new measure discounts the visual color difference as the chroma of the reference color increases. This relationship can be seen from the expression,

$$\Delta E_{94}^* = \sqrt{\left(\frac{\Delta L^*}{k_L S_L}\right)^2 + \left(\frac{\Delta C_{ab}^*}{k_C S_C}\right)^2 + \left(\frac{\Delta H_{ab}^*}{k_H S_H}\right)^2} \quad (3-22)$$

where

$$\begin{aligned} S_L &= 1 \\ S_C &= 1 + 0.045 C_{ab}^* \\ S_H &= 1 + 0.015 C_{ab}^* \end{aligned}$$

$C_{ab}^*$  is the chroma of the standard, or geometric mean, and  $k_L = k_C = k_H = 1$  for a set of reference sample, viewing, and illuminating conditions.

The calculation of  $\Delta E_{94}^*$  can be interpreted as a scaling of the  $\Delta C_{ab}^*$  and  $\Delta H_{ab}^*$  coordinates so that they are transformed into a modified perceptual color space, followed by a distance computation. In matrix notation, the first step is

$$\begin{bmatrix} \Delta L^* \\ \Delta C_{ab}^*/S_C \\ \Delta H_{ab}^*/S_H \end{bmatrix} = \begin{bmatrix} 1 & 0 & 0 \\ 0 & 1/1+0.045C_{ab}^* & 0 \\ 0 & 0 & 1/1+0.015C_{ab}^* \end{bmatrix} \begin{bmatrix} \Delta L^* \\ \Delta C_{ab}^* \\ \Delta H_{ab}^* \end{bmatrix}. \quad (3-23)$$

If the (3 x 3) diagonal matrix of Eq. (3-23), evaluated where  $C_{ab}^* = \mu_{C_{ab}^*}$ , is denoted as  $\mathbf{P}$ , then the covariance matrix for the transformed  $\Delta L^*$ ,  $\Delta C_{ab}^*$ ,  $\Delta H_{ab}^*$  color space is,

$$\Sigma_{L^* C^*/S_C H^*/S_H} = \mathbf{P} \Sigma_{L^* C^* H^*} \mathbf{P}^T. \quad (3-24)$$

This is found to be

$$\Sigma_{L^* C^*/S_C H^*/S_H} = \begin{bmatrix} 0.094 & 0.021 & 0.186 \\ & 0.255 & 0.100 \\ & & 0.680 \end{bmatrix}. \quad (3-25)$$

The square-root of the diagonal elements gives the rms deviations, also listed in Table 3-2.

Following the same steps as for the calculation of  $E[\Delta E_{ab}^*]$ , in Eq. (3-20),  $E[\Delta E_{94}^*]$  was found to equal to 0.885. As expected from Eq. (3-22), the weighting of the variation in chroma and hue difference has been reduced. An equivalent error ellipsoid calculated from the covariance matrix of Eq. (3-25) is given in Fig. 3-6, and completes the analysis. Note that the figure is not only smaller, but more spherical than that of Fig. 3-5.

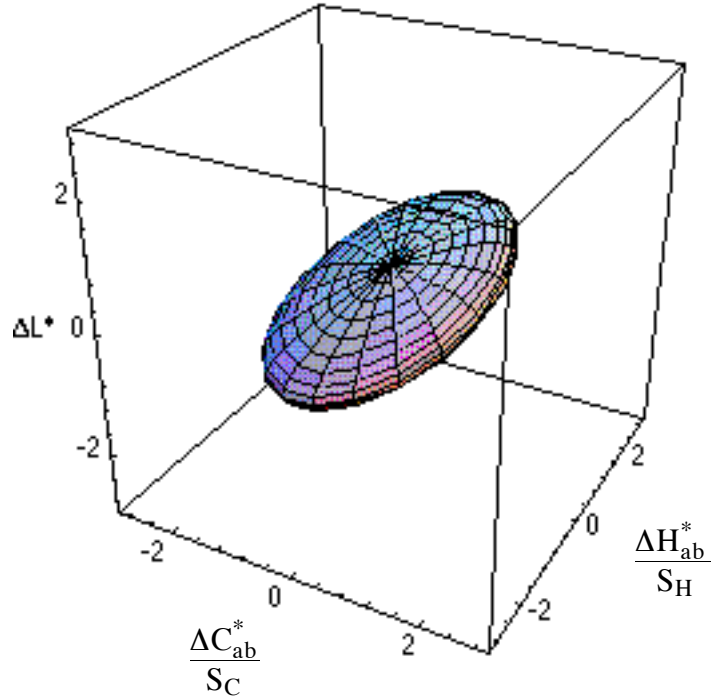


Fig. 3-6: Error ellipsoid based on transformed  $\Delta L^*$ ,  $\Delta C_{ab}^*$ ,  $\Delta H_{ab}^*$  coordinates, consistent with the  $\Delta E_{94}^*$  color-difference measure.

Since the error-propagation analysis described above is based on the first terms of the Taylor series approximation to any nonlinear transformation, the resulting statistics are necessarily approximations. This approximation was quantified, by investigating the previously computed example by simulation. This was based on the direct transformation of a set of 2000  $\{X, Y, Z\}$  coordinates to CIELAB. The normally distributed input values, generated by random number generator, had mean values and covariance matrices equal to those used in the computed example. The resulting sample covariance matrix was

$$\hat{\Sigma}_{L^* C^*/S_C H^*/S_H} = \begin{bmatrix} 0.095 & 0.025 & 0.187 \\ & 0.268 & 0.111 \\ & & 0.685 \end{bmatrix}.$$

This compares favorably with the calculated matrix of Eq. (3-25), as does the computed sample mean,  $\overline{\Delta E_{94}^*} = 0.898$ , with the previously calculated value of 0.885.

### 6. Detector Error Specification

The above computed example illustrates how the error propagation analysis can be applied to color-signal transformations and CIELAB error statistics can be predicted from the input signal,  $\{X, Y, Z\}$ , mean vector, and covariance matrix. These techniques can also be used to propagate errors from CIELAB (back) to tristimulus values or camera signals, if the matrix operations and the nonlinear transformations are invertible. This will now be outlined.

Assume that for a measurement system there is an error budget such that no more than a given average error,  $\Delta E_{ab}^*$ , in CIELAB is allowable due to stochastic error in the input tristimulus-value signals. The calculations of  $\Delta E_{ab}^*$  and  $\Delta E_{94}^*$  cannot be inverted. One can choose, however, to evaluate the propagation of CIELAB errors with a given form of covariance matrix. In addition, due to the nonlinear step in the transformation, the error propagation will depend on the mean value of the signal to be evaluated, as was the case for the transformation  $\{X, Y, Z\} \rightarrow \{L^*, a^*, b^*\}$ . As an example, the same mean signal will be used as for the previous case, and for simplicity, let the acceptable errors have a mean  $E[\Delta E_{94}^*] = 0.5$ , and assume independent errors in  $L^*$ ,  $a^*$ , and  $b^*$ . From Eq. (3-20), setting the covariance terms to zero,

$$\Sigma_{\Delta L^* \Delta C_{ab}^*/S_C \Delta H_{ab}^*/S_C} = \frac{(E[\Delta E_{94}^*])^2}{3} \mathbf{I} = 0.083 \mathbf{I} . \quad (3-26)$$

As in Eq. (3-5),

$$\Sigma_{\Delta L^* \Delta C_{ab}^* \Delta H_{ab}^*} = \mathbf{P}^{-1} \Sigma_{\Delta L^* \Delta C_{ab}^*/S_C \Delta H_{ab}^*/S_C} [\mathbf{P}^{-1}]^T$$

where  $\mathbf{P}$  is given in Eq. (3-23). The next steps are the transformation from  $\{\Delta L^*, \Delta C_{ab}^*, \Delta H_{ab}^*\}$  to  $\{\Delta L^*, \Delta C_{ab}^*, \Delta h_{ab}\}$  and then to  $\{L^*, a^*, b^*\}$ . Since the matrices  $\mathbf{J}_{L^* C_{ab}^* h_{ab}^*}$ ,  $\mathbf{J}_{L^* a^* b^*}$  and  $\mathbf{J}_{f(t)}$  are easily inverted, the error covariance matrix for the input signals as,

$$\Sigma_{\mathbf{t}} = \mathbf{J}_{f(t)}^{-1} \mathbf{J}_{L^* a^* b^*}^{-1} \mathbf{J}_{L^* C_{ab}^* h_{ab}^*}^{-1} \Sigma_{\Delta L^* \Delta C_{ab}^* \Delta H_{ab}^*} [\mathbf{J}_{L^* C_{ab}^* h_{ab}^*}^{-1} \mathbf{J}_{L^* a^* b^*}^{-1} \mathbf{J}_{f(t)}^{-1}]^T. \quad (3-27)$$

For the example signal, the calculated tristimulus-value covariance matrix is

$$\Sigma_{\mathbf{t}} = 10^{-5} \begin{bmatrix} 3.28 & 2.36 & 0.322 \\ & 2.21 & 0.477 \\ & & 0.908 \end{bmatrix} \quad (3-28)$$

and the rms signal error of

$$\sigma_X = 0.0057, \sigma_Y = 0.0047, \sigma_Z = 0.0030.$$

Equation (3-28) represents the propagation of the covariance matrix of Eq. (3-26) to an equivalent input colorimeter/camera signal matrix. This means that, for independent CIELAB errors, to achieve an average  $\Delta E_{94}^*$  value of 0.5, the source error covariance elements must be no greater than those given in Eq. (3-28).

## B. CCD Imager Noise Model

The previous section discussed ways in which stochastic error can be analyzed as it is propagated through a signal path. The sources of error in electronic image detection will now be modeled. This will set the stage for the case of multispectral image acquisition and signal processing from detected image to colorimetric representation to be addressed in Chapter V.

Charge-Coupled Device (CCD) detectors arrays use analog shift registers to read out a signal charge for each pixel. The one- or two-dimensional array and associated electronics are referred to as the CCD imager. There are several sources of image noise in CCD imagers (McCurnin *et al.* 1993, Holst 1996), but for present purposes the net stochastic variations will be described as being of three types.

Figure 3-7 shows a simple model for the CCD imager, whereby a certain fraction,  $\eta$ , of the incident photons are detected. Ignoring dark noise for the moment, this mechanism can be written as

$$o = i\eta \quad (3-29)$$

where  $o$  and  $i$  are the exposure and detected signals, respectively. If the mean input exposure is  $\mu_i$ , then the mean output, Poisson-distributed signal charge, in electrons, is

$$\mu_o = \eta\mu_i, \quad (3-30)$$

where  $\eta$  is the effective quantum efficiency<sup>†</sup> which is a function of wavelength. Note that

---

<sup>†</sup> This includes the primary quantum efficiency and any net loss mechanisms that reduce the mean number of signal charge electrons that are read out, amplified, quantized, etc.

it is assumed that, over the visible wavelength range, a single free electron is generated for each absorbed photon. The arrival statistics of uniform exposure (per area and over time) are governed by Poisson statistics, and for this discrete probability distribution the variance is equal to the mean,  $\sigma_i = \mu_i$ . If  $\eta$  is interpreted as the binomial probability that an incident photon is detected, then the detected electrons are also distributed as Poisson random variables, for  $\eta \leq 1$ . Therefore, for the detected signal,  $\sigma_o^2 = \mu_o$ . This component of image noise is usually referred to as shot, or photon noise. Since it will be observed even with perfect image detection, it is a lower noise level to which actual imager performance can be compared.

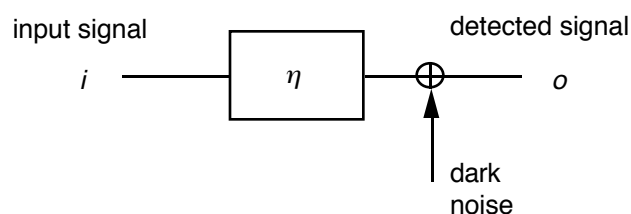


Fig. 3-7: Model for electronic image detection.

Another noise component included in our analysis is dark noise, so-called because it is characterized by signal fluctuations in the absence of light exposure. There are several physical origins of this noise source, such as spontaneous thermal generation of electrons, and it is modeled as a constant-variance, zero-mean random variable added to the detected signal. If both dark and shot noise are included as statistically independent stochastic sources, the resulting noise variance is

$$\sigma_o^2 = \sigma_d^2 + \eta\mu_i \quad (3-31)$$

where the dark noise variance is  $\sigma_d^2$ . Note that for average signal levels where shot noise is dominant, the variance is proportional to the mean signal and the rms noise is  $\sigma_o \cong \sqrt{\eta\mu_i}$ . The noise model described by Eq. (3-31) is often used for electronic image capture.

Equation (3-31) assumes that a fixed fraction of incident photons are detected for each detector in the imaging array. A third source of image noise arises, however, because the detector sensitivity varies from pixel-to-pixel. This can result in a varying signal offset, or bias but is usually characterized by a variation in  $\eta$  about its nominal value. This photoresponse nonuniformity (Holst 1996) is often described as a variation in the detector gain (electrons/photon) across the image field. Many imaging systems correct for this fixed-pattern noise by a pixel-to-pixel calibration to a uniform, or flat-field image. This significantly reduces the influence of this noise source but relies on the fixed-pattern detector gains being stable between periodic calibration procedures. In addition, the finite arithmetic precision and signal quantization usually result in a residual fixed-pattern noise component being observed.

The fixed-pattern gain variation can be modeled by letting  $\eta$  be a random variable with a mean and variance equal to  $\mu_\eta$  and  $\sigma_\eta^2$ , respectively. Thus both variables in the RHS of Eq. (3-29) are random variables, if variation across the imaging array is included. Since the detected signal is no longer a simple Poisson process, its variance is not necessarily equal to its mean value. Allowing the fixed-pattern gain (i.e.,  $\eta$ ) to vary as an approximately normal random variable from pixel-to-pixel it was found, as shown in Appendix D, that

$$\mu_o = \mu_\eta \mu_i \tag{3-32a}$$

$$\sigma_o^2 = \mu_\eta + \sigma_\eta^2 \mu_\eta^2 (1 - f^2), \quad (3-32b)$$

where  $f = \sigma_\eta / \mu_\eta$ , the fractional rms fixed-pattern gain noise. Note that when  $\sigma_\eta = 0$  equation (3-32b) reverts to the simple Poisson case, as it should. If the fixed pattern gain variation can be expressed as a fixed fraction of the input signal,  $\sigma_\eta^2 = f^2 \mu_\eta^2$ , and the dark noise is included, from Eqs. (3-32a) and (3-32b)

$$\sigma_o^2 = \sigma_d^2 + \mu_o + \mu_o^2 f^2 (1 - f^2). \quad (3-33).$$

Equation (3-33) shows the signal variance in electrons as comprising of three components, The first term of the RHS is the dark noise whose variance is independent of the mean. The second term is the familiar shot-noise variance proportional to the mean signal. The third term is a component that is proportional to the square of the mean signal.

After image capture, the pixel values are usually expressed in terms of encoded signal digital counts (e.g. 0-255) or on a scale covering to the minimum and maximum exposure over which the signal is quantized. This is helpful because it allows the comparison of imaging performance as the dark, shot, and fixed-pattern noise components vary. The noise variance (and rms noise) can be put on a [0-1] scale if both sides of Eq. (3-33) are divided by the maximum signal charge in electrons. This was done for Fig. 3-8 which shows the rms imager noise plotted as a function of both fixed pattern gain noise,  $f$ , and mean signal level. For this example, the maximum signal is 60,000 electrons and the dark current taken as 30 electrons, or 0.5% of the maximum. As  $f$  increases, the rms noise

---

† The maximum charge is often set at less than the imager full-well charge to avoid signal clipping and detector blooming, since the maximum scene exposure is difficult to predict with certainty.

changes from being primarily shot noise to being dominated by the fixed-pattern component.

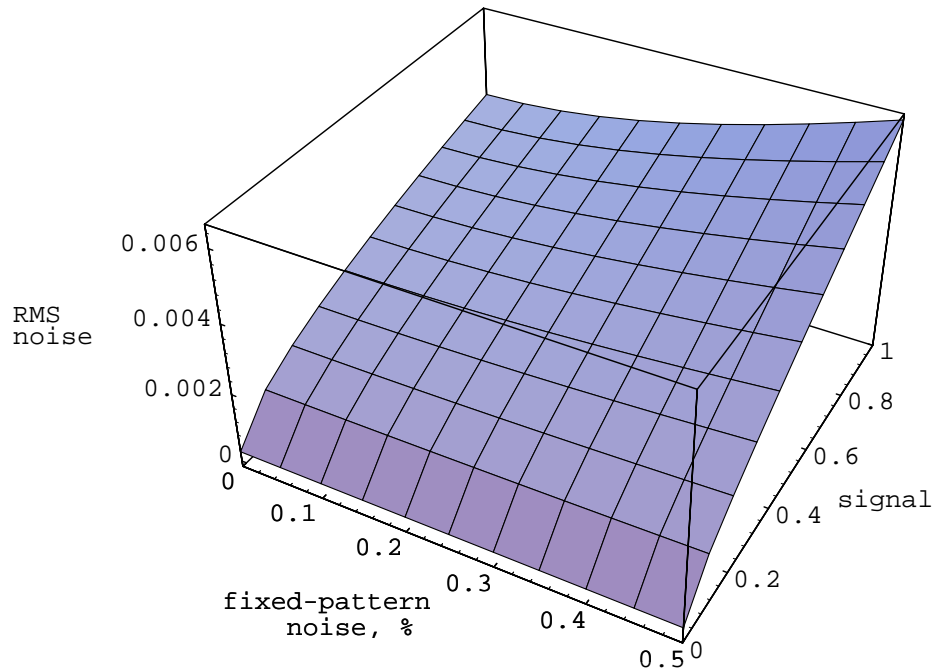


Fig. 3.8: RMS imager noise model as a function of mean signal and fixed-pattern gain noise. The maximum signal,  $e_{max}$  was 60,000 electrons, rms dark noise = 0.5% of  $e_{max}$ . Fixed pattern noise,  $f$ , varies from 0 - 0.5%. The signal and noise are shown on [0-1] scale.

### C. Image noise propagation for 3-Channel CCD Cameras

As an example of how to combine the error-propagation analysis results of Section 3.A in the context of an imager model, of Section 3.B, consider a trichromatic camera. It is assumed that the camera is used to record scene information, and that colorimetric image information, such as CIELAB coordinates is needed to facilitate image exchange or printing. The camera spectral sensitivity characteristics are shown in Fig. 3-8, for the  $R$ ,  $G$ , and  $B$  signals.

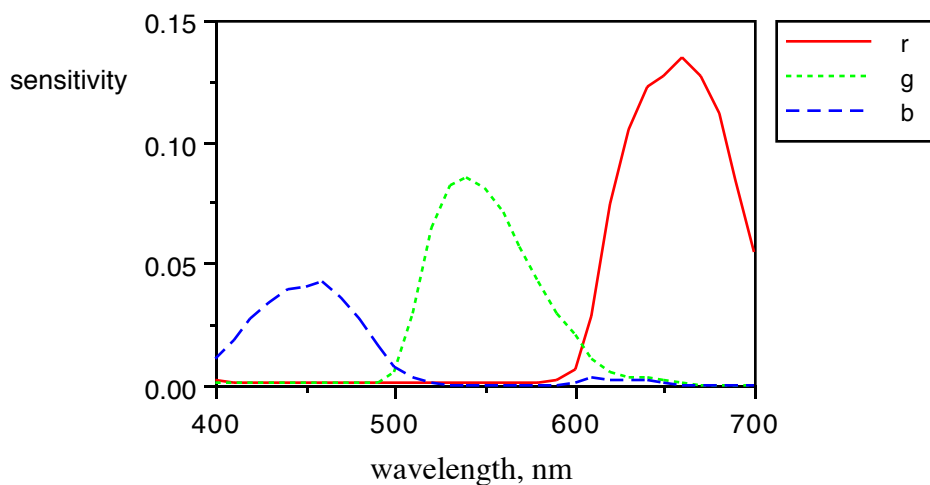


Fig. 3-9: Spectral sensitivity functions of detector and optics in arbitrary units.

To transform the camera signals to approximations of CIE tristimulus values ( $X, Y, Z$ ) a matrix operation is often used (Quiroga *et al.* 1994)

$$\mathbf{t} = \mathbf{M} \mathbf{s} \quad (3.34)$$

where  $\mathbf{s}^T = [R \ G \ B]$ ,  $\mathbf{t}^T = [X \ Y \ Z]$ ,  $\mathbf{M}$  is a ( $3 \times 3$ ) matrix of weights. In most practical cases, as in this example, the imager spectral sensitivities cannot be expressed as a linear combination of CIE color matching functions, therefore Eq. (3.34) allows only an approximation to the tristimulus values. The matrix  $\mathbf{M}$  will be a function of the illuminant power spectral distribution and imager spectral sensitivities, and is chosen to minimize a particular weighting of colorimetric difference between the estimated and true tristimulus values.

As discussed in the previous section, imaging detectors are subject to stochastic error

due to, for example, photon arrival statistics (shot noise), thermally generated electrons, readout electronics and signal amplification. The detected signals,  $\mathbf{s}$ , will therefore include variation from many sources, and can be modeled as a set of random variables. The transformed signal,  $\mathbf{t}$ , contains a corresponding error that will be a function of the variation in  $\mathbf{s}$ , and the matrix transformation,  $\mathbf{M}$ . Results for the error-propagation analysis of section 3A provide a way of predicting the statistics of the noise due to the image detection step in terms of the output transformed signal.

The second-order statistics of a set of detected signals subject to a stochastic error can be described by the covariance matrix,

$$\Sigma_{\mathbf{s}} = \begin{bmatrix} \sigma_{RR} & \sigma_{RG} & \sigma_{RB} \\ \sigma_{RG} & \sigma_{GG} & \sigma_{GB} \\ \sigma_{RB} & \sigma_{GB} & \sigma_{BB} \end{bmatrix}$$

where the diagonal elements are the variance values of the  $R$ ,  $G$ , and  $B$  signals. In general, the elements of  $\Sigma_{\mathbf{s}}$  will be functions of the mean detected signal. The resulting covariance matrix for the transformed signals is

$$\Sigma_{\mathbf{t}} = \mathbf{M} \Sigma_{\mathbf{s}} \mathbf{M}^T. \tag{3.35}$$

Similarly, the propagation of the signal covariance through nonlinear transformations can be approximated by applying a derivative matrix, as in Eq. (3.7). If the CIELAB coordinates are expressed as a vector,  $\mathbf{c}^T = [L^* \ a^* \ b^*]$ , and the Jacobian Matrix of the multivariate transformation is written, as in Eq. (3.16)

$$\mathbf{J} = \begin{bmatrix} 0 & \partial L^*/\partial Y & 0 \\ \partial a^*/\partial X & \partial a^*/\partial Y & 0 \\ 0 & \partial b^*/\partial Y & \partial b^*/\partial Z \end{bmatrix}$$

then

$$\Sigma_c \approx \mathbf{J} \Sigma_t \mathbf{J}^T. \quad (3.36)$$

For this example, it will be assumed that the detector noise is characterized by a dark noise and shot noise components. Note that these characteristics can be estimated from the published information for many detectors, which often includes values for RMS dark electrons, RMS read noise, and shot-noise estimates based on full-signal charge. It is assumed that the fixed-pattern noise from variation in the sensor sensitivity is compensated for, and that the three image (*RGB*) layers are fully populated having been fully sampled, or by previous interpolation.

Let the shot-noise levels correspond to a maximum signal of 60,000 electrons/pixel and the RMS dark noise is taken as equivalent to 50 electrons, 0.08% of the maximum signal. These noise characteristics are shown in Fig. 3.10, and expressed on the scale of [0-1]. The color-correction matrix, was calculated to transform the detected signals to estimates of tristimulus values. Given the spectral sensitivities of Fig. 3.9 and a D65 illuminant, the matrix

$$\mathbf{M} = \begin{bmatrix} 0.321 & 0.666 & 0.425 \\ 0.106 & 1.140 & 0.125 \\ -0.039 & -0.076 & 4.399 \end{bmatrix}, \quad (3.37)$$

is based on a set of 24 measurements of a MacBeth ColorChecker chart, and can be applied as in Eq. (3.34).

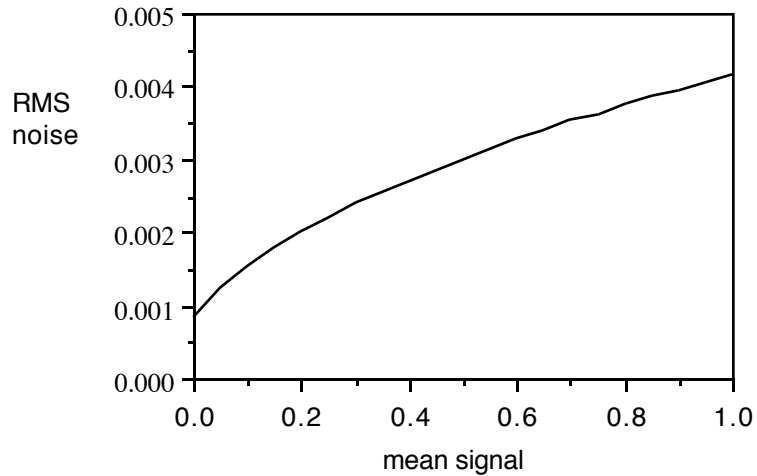


Fig. 3-10: RMS noise characteristics for model imager, where signal and noise are expressed on a [0-1] scale.

For this example, it is assumed that the camera signals include independent noise fluctuations, whose RMS values vary with mean signal level as in Fig. 3.10. The signal covariance,  $\Sigma_s$ , is diagonal. The results of applying Eqs. (3.36) and (3.37) are given in Table 3-3, and predict areas in CIELAB with higher noise. The noise of the Black sample can be attributed to the high gain from the matrix  $\mathbf{M}$  element, 4.399. This is because of the relatively low spectral sensitivity of the blue detection channel. The transformation from tristimulus values to CIELAB further emphasizes the dark signal fluctuations, due to the cube-root transformation and its derivative.

Table 3-3: Measured CIELAB coordinates for the 24 patches of the MacBeth ColorChecker and the calculated CIELAB RMS errors following imager noise model.

Name	$L^*$	$a^*$	$b^*$	$\sigma_{L^*}$	$\sigma_{a^*}$	$\sigma_{b^*}$
Dark skin	37.9	14.7	14.9	0.28	0.63	1.69
Light skin	66.2	15.5	14.7	0.20	0.43	0.91
Blue sky	51.1	-6.48	-23.5	0.24	0.46	0.83
Foliage	44.4	-11.2	24.9	0.26	0.48	1.66
Blue flower	57.6	14.6	-24.8	0.21	0.47	0.77
Bluish green	73.0	-21.6	0.54	0.19	0.33	0.77
Orange	59.4	21.5	53.2	0.21	0.47	1.81
Purplish blue	41.0	9.58	-43.3	0.27	0.58	0.82
Moderate red	50.8	42.2	10.6	0.22	0.54	1.13
Purple	32.5	28.5	-19.1	0.30	0.74	1.16
Yellow green	74.3	-22.3	60.9	0.19	0.33	1.33
Orange yellow	71.4	8.13	65.5	0.19	0.40	1.56
Blue	29.5	12.5	-52.7	0.34	0.76	0.92
Green	57.6	-31.1	38.6	0.23	0.33	1.42
Red	43.1	66.4	29.4	0.22	0.61	1.95
Yellow	81.8	-2.33	80.3	0.18	0.35	1.51
Magenta	52.7	54.5	-12.9	0.20	0.53	0.87
Cyan	51.7	-11.8	-28.1	0.24	0.44	0.80
White	96.1	-3.65	1.82	0.16	0.33	0.65
Neutral 8	81.1	-3.61	-0.85	0.18	0.36	0.71
Neutral 6.5	66.2	-3.16	-0.64	0.20	0.40	0.82
Neutral 5	50.6	-2.66	-0.85	0.24	0.47	1.00
Neutral 3.5	33.7	-2.35	-0.67	0.31	0.63	1.45
Black	19.0	-0.80	-0.98	0.50	1.02	2.50

#### D. Conclusions

From the general analysis of error propagation, the first two statistical moments of stochastic errors can be analyzed in many current color-spaces and through many color-image processing transformations. In addition to the magnitude of the signal variance, the propagation of the covariance between sets of signals has been described. The methods used have been implemented using matrix-type operations, but there are several

requirements for their success. The errors to be analyzed must result from continuous stochastic sources. If so, then expressions for the linear matrix transformation, Eq. (3-5), is exact. The expressions for nonlinear transformations, however, are based on truncated series approximations. The partial derivatives included in these expressions should be continuous. Note, however, as shown for the tristimulus values-CIELAB path, that approximately continuous transformations can also be analyzed.

The accuracy of the linear approximations can be evaluated by examining the higher-order derivatives. For example, the magnitude of the second term of the RHS of Eqs. (3-2) or (3-3) should be much less than the first,  $f_x' \sigma_x^2$ , in order to use the linear approximation of Eqs. (3-4) and (3-7). Since both  $f_x'$  and  $f_{xx}''$  are functions of  $\mu_x$ , it is useful to identify values of the argument(s) for which the condition does not hold, e.g.,  $f_x' \approx 0$ . If the first derivative is small compared to the second, and the error distribution is approximately Gaussian, then Eq. (3-3) can be used. This form can also be used for error distributions which are similar in shape to the normal, e.g., lognormal and Laplacian. For other distributions, such as the uniform, chi-square or exponential, Eq. (3-3) should be used.

By applying the error propagation techniques, variation due to measurement precision can be compared with the effects of experimental variables using error ellipses and ellipsoids. These are based on the calculated or observed covariance matrices and underlying probability density functions, and require the analysis of covariance. The inverse of many color-signal transformations of current interest can also be addressed. As demonstrated, a given tolerance of average  $\Delta E_{ab}^*$  or  $\Delta E_{94}^*$  can be related to an equivalent uncertainty in tristimulus values, other sets of detected signals, or image pixel values.

Modeling of the noise characteristics of color-measurement and imaging devices can be combined with error-propagation analysis to predict signal uncertainty in color-exchange

signals. Since physical devices include correlated noise sources, and signal-processing often combines signals, analysis of signal covariance is included. By applying these methods, design and calibration strategies can include not only the minimization of mean color errors, but also the signal variation. Uncertainty from signal detection, operating conditions, aging and manufacturing tolerances can be analyzed if they are well described as stochastic processes. Noise levels modeled in this way can also be compared with errors due to limited precision used in signal storage and image processing.

## **IV. EXPERIMENTAL: MULTISPECTRAL DIGITAL IMAGE CAPTURE**

As discussed in Chapter II, an experimental multispectral camera was assembled using a Kodak Professional DCS 200m (monochrome) digital camera and set of seven interference filters from Melles Griot. An additional filter-image was captured for a total of eight records per multispectral image. This eighth filter was a broadband infrared blocking filter, Schott glass KG5 (1mm.). This was added during the experiment due to the apparent low contrast of the f7 digital images, with the thought that they may be corrupted by unwanted infra-red detection<sup>†</sup>. The camera and filter set were mounted in a copy stand to capture several images of flat test targets and artwork. The objective was to investigate the extent to which the sequentially captured digital images could be used as a multispectral description of the illuminated object. The evaluation closely paralleled the analysis of both the mean signal and image noise that was presented in Chapters II and III. Of specific interest was the extent to which the straightforward matrix-vector description of ideal image capture, and CCD imager noise would need to be adapted to describe, e.g., the spectral transmittance of actual interference filters, and copy stand illumination nonuniformity across the image field. In addition, signal quantization was expected to introduce additional signal uncertainty.

### **A. Equipment**

The experimental layout is shown schematically in Fig. 4-1, where the sample was illuminated by the copy stand lamps at 45°. There were two lamps on each side, separated vertically by 22 cm about the center of the sample, for a total of four. Each lamp used a 250-watt Sylvania PKT bulb, and was 47 cm. from the sample. The direction of the lamps

---

<sup>†</sup>subsequent image processing results did not favor f8 over f7 data, however.

was adjusted to minimize the exposure nonuniformity as detected by the digital camera. This resulted in each set being pointed at a position approximately 15 cm from the center of the sample. Not shown is the Apple Macintosh computer, to which the camera was connected via an SCSI cable. The image files were acquired into Adobe Photoshop 2.0 software.

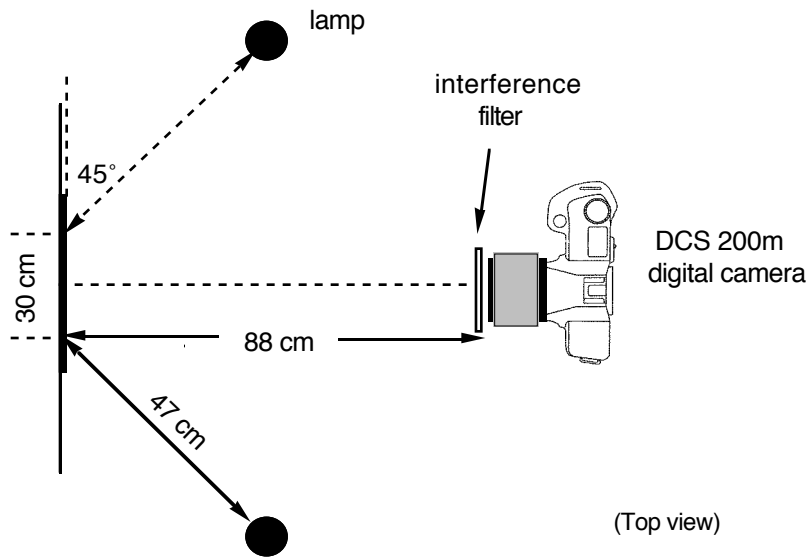


Fig. 4-1: Experimental multispectral camera layout.

The Kodak Professional DCS 200m digital camera is a conventional 35mm Nikon N8008s camera that has been modified by the attachment of an electronic camera back so a CCD imager is in place of the photographic film. In addition, magnetic storage is added below the camera, so that multiple images can be acquired. The camera is shown in Fig. 4-2. The imager size is smaller than a frame of 35mm film, so that when the camera is used with a Nikon 28 mm lens, the scene is captured with an approximately normal (50mm lens) perspective. This was the lens used. The effective sensitivity of the camera is influenced by the ISO setting. If used with photographic film, this would adjust the exposure metering system to match the film speed. In the electronic version of the camera, however, this ISO value sets an effective camera gain (digital signal value/exposure level). The values of 100, 200, and 400 are available, with 200 being recommended (Kodak 1994).

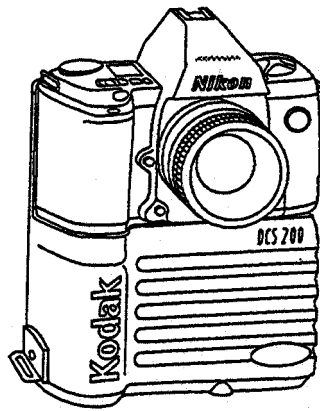


Fig. 4-2: Kodak Professional DCS 200m digital camera.

The camera has both automatic focus and exposure controls that operate in the same way that the camera would if it had the standard camera back and film. Since both of these are optimized for normal (broad-spectrum) visible images, they would not necessarily give accurate settings when used with the narrow-band interference filter set. To avoid this

source of variability, manual settings were used for both camera focus and exposure. The camera captures digital images that are 1524 pixels x 1012 pixels, with each pixel value encoded as an 8-bit [0-255] number. The distance from the camera to the sample was adjusted so that a sample 33 cm x 23 cm was covered by an area 1340 pixels x 930 pixels. The sampling interval was 0.25 mm at the object. The distance from sample to the front surface of the lens was 88 cm. For each image captured in the set, the filter was held in contact with the metal ring of the camera lens. For each image captured in a set of seven, the filter was held close to the front surface of the camera lens.

### **B. Spectral Measurements of Camera Components**

Before any image capture was performed with the filter sets, the spectral characteristics of each of the components were measured. The spectral power distribution of the source was measured by replacing the digital camera with the PhotoResearch SpectraView PR-703/PC spectroradiometer. Ten measurements were made for the light reflected from a barium sulphate reference target placed at the center of the image field. The resulting spectral radiance measurement is shown in Fig. 4-3. This graph is shown in scaled form in Fig. 2-7, for comparison with CIE illuminants A and D<sub>65</sub>.

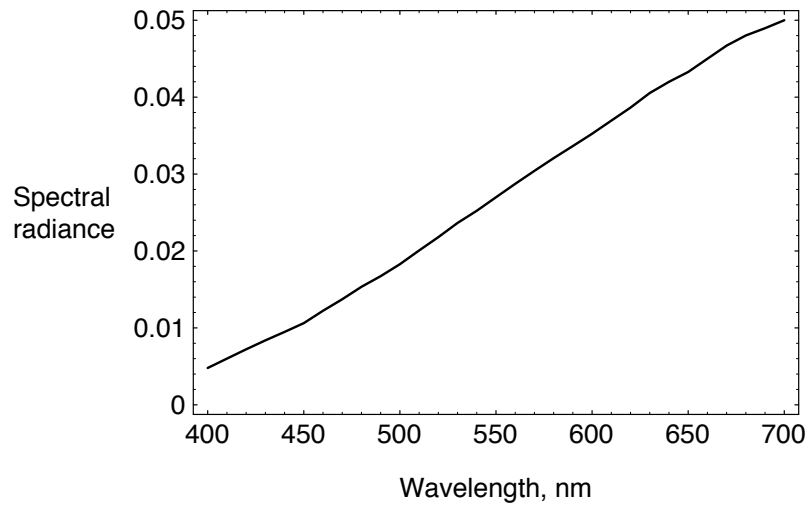


Fig. 4-3: Measured spectral radiance for the copy stand source, in units of  $\text{w/sr m}^2/\text{nm}$ .

The spectral transmittance functions of the set of interference filters was then measured by repeating the above measurement with each of the seven filters in the optical path, close to the front surface of the SpectraView lens. Each of these measurements were then divided, wavelength-by-wavelength, by the source radiance to give the measured spectral transmittance. These are shown in Fig. 4-4. As noted earlier, the curve shapes are similar with filters centered at approximately 50nm intervals.

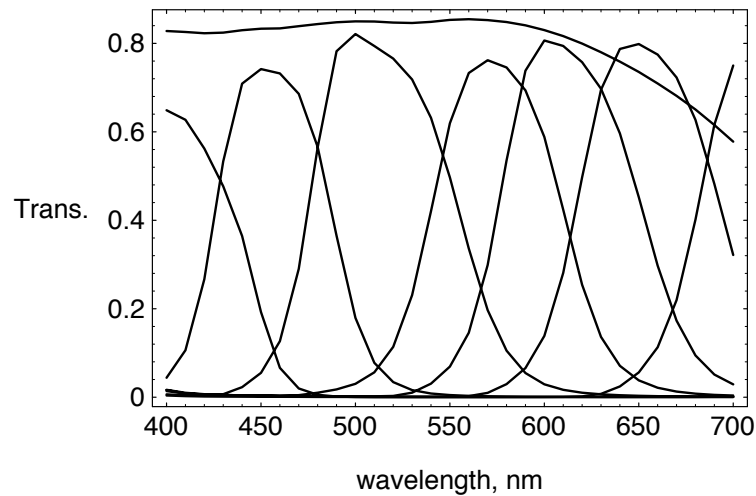


Fig. 4-4: Measured spectral transmittance characteristics, on a [0-1] scale, for the set of interference filters. The eighth broadband response is that of an infrared blocking filter.

Measurement of the spectral sensitivity of the digital camera was accomplished using a calibrated light source, part of the Model 740A-D Optical Radiation measurement system from Optronic Laboratories, Inc. The procedure, described in Appendix F, yields an effective spectral sensitivity in terms of digital count/ $\mu\text{m}^2/\text{nm}$ . It can be compared with the expected detector absolute quantum efficiency in shape, as a normalized curve. This is shown in Fig. 4-5, where the measured spectral sensitivity was scaled so that the integrated curve was equal to that calculated from nominal quantum efficiency and lens spectral transmittance data<sup>†</sup>.

Figure 4-5 indicates that the digital camera response is far from uniform over the visible wavelength range. Most CCD imagers show a rising intrinsic quantum efficiency from about 400nm to the mid-infrared 2.0  $\mu\text{m}$  (Dereniak and Crowe 1984). The high sensitivity above 700 nm needs to be reduced for visible imaging, since it would result in a reduced contrast (visible) image similar to that due to optical flare. To solve this problem an infrared

<sup>†</sup>This information was kindly supplied by Richard Vogel of Eastman Kodak Company.

blocking filter is often used in the optical path. In the case of the DCS 200m camera, it is attached to the front surface of the detector array. This causes the spectral sensitivity of the camera to decrease above 600nm. In particular, the low response above 650nm is the reason that the experimental camera exposure time had to be significantly increased for filter 7. This was done to avoid a reduced signal-to-noise ratio and increased signal quantization errors. This is a common technique (Tominaga 1996), however some systems apply an analog gain to compensate for a low signal prior to quantization (Martinez *et al.* 1993). This would be useful for applications where extending the exposure time is undesirable due to camera or subject motion.

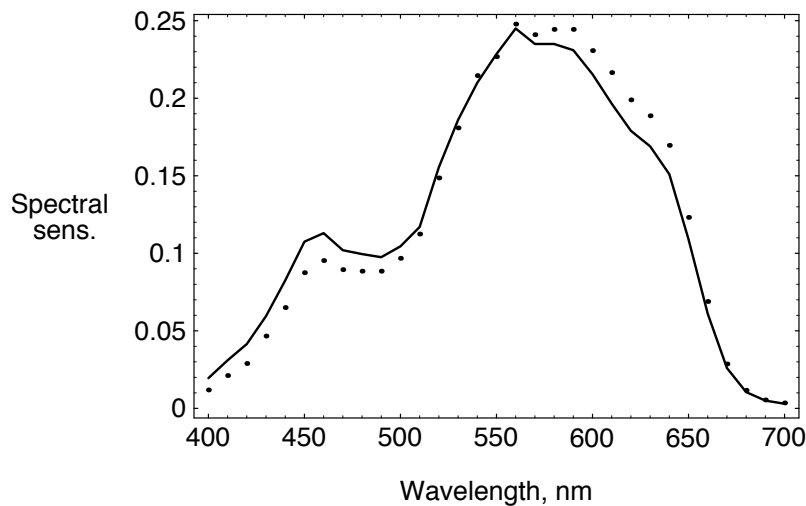


Fig. 4-5: Comparison of the measured (symbol) digital camera quantum efficiency (on a 0-1 scale) with that calculated (line) from nominal data supplied from Eastman Kodak Company.

### C. Photometric, Dark Signal and Illumination Compensation

Any analysis of the experimental multispectral camera requires information about the relationship between the output digital signal and the input exposure. This can vary between cameras, since although the primary photon-detection mechanism is approximately proportional (linear), the subsequent signal processing influences the overall input-output characteristic. The basic signal processing steps are shown Fig. 4-6. The detector absorbs energy from the incident exposure photons and generates an electron charge. This signal is read out from the detector, amplified and stored as a quantized digital signal. Often this storage is temporary, because the digital signal values are immediately transformed, via a discrete look-up table (LUT), into another form depending on the intended use of the digital image. If this LUT is a transformation from  $p$  to  $q$  discrete values, then a change in the effective signal quantization is also accomplished in this step. A typical LUT is a transformation between 1024 (10 bits/pixel) to 256 (8 bits/pixel), with a shape designed to counteract the photometric characteristics of CRT displays (Berns *et al.* 1991).

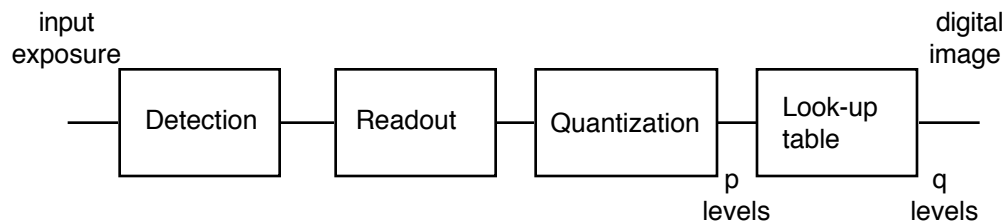


Fig. 4-6: Basics steps of image capture in a digital camera

Due to the wide range in the copy stand lamp spectral radiance and camera sensitivity over the wavelength range, as shown in Figs. 4-3 and 2-2, it was necessary to vary the camera exposure time from filter to filter. If a fixed camera exposure was used, then, for

example, the first and seventh image records would have been based on very low levels of detected signal. This would have resulted in high levels of image noise. It was decided to adjust the camera exposure time so as to yield a maximum digital signal for a white scene reference, without causing signal clipping at the maximum of level 255. In addition, since actual spectral transmittance can vary with incident angle for this type of filter, a fixed lens f/number was chosen for all exposures in a series. The camera ISO value was set so that the exposure times were within a range of  $\leq 2$  sec., to avoid any potential increase in (dark current) image noise due to long exposure times. Table 4-1 lists the camera settings used for image capture of a target made up of the Munsell 37 sample set.

Table 4-1: Camera settings used for sample target imaging.

	f1	f2	f3	f4	f5	f6	f7
Camera exposure time (sec.)	2	1/4	1/15	1/30	1/30	1/30	1/4
Camera ISO	200						
lens f/number	f/16						

To measure the camera photometric characteristics, the six neutral steps of the test chart were captured at the center of the image field with the above settings. The reason for capturing all of the data at the center, was to reduce the effect of nonuniform illumination across the image field. For each filter, six images were captured and the average digital value for the patch was recorded, for a total of 42 values. These were least-square fit with a polynomial model against calculated signal values based on the measured source illumination, sample reflectance factor, and measured filter-camera spectral sensitivity. Fig. 4.7 shows representative characteristics for the signal path for the f3 record (filter 3,

centered at 500 nm). By calculating an independent calibration curve for each record, the variation across camera exposure-time settings is taken into account and there is no reliance on the accuracy of the nominal exposure time.

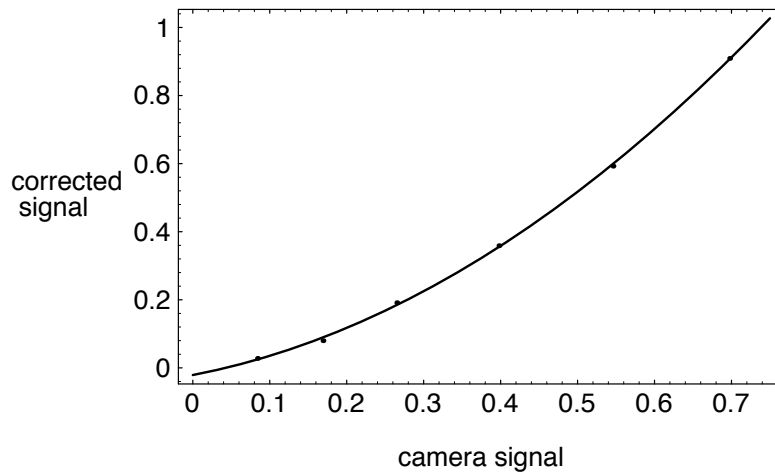


Fig. 4-7: Compensation used for the DCS camera for images captured with filter number 3.

Two potential sources of error in the multispectral image camera require compensating dark signal and illumination nonuniformity across the image field. Signal correction schemes, however, usually rely on an implicit model of how these errors are introduced. If an image is captured without light, the resulting image file will usually contain some stochastic dark noise variation from pixel-to-pixel. In addition the average signal may also vary. It is usually assumed that this dark signal constitutes a bias signal added to the detected image. Since a component of this dark signal is the spontaneous thermal generation of free electrons, it can vary with exposure interval.

A straightforward way of estimating this dark signal is to capture dark images (e.g. with camera lens cap in place) and examine the resulting surface of (low spatial-frequency)

signal values. This was done for camera settings corresponding to those used for image capture. Figure 4-8 shows such a surface expressed in digital signal counts. To compensate for this source of error, a dark signal from this surface is subtracted from the camera image signal as a function of image position. Typical dark-signal characteristics for the DCS 200M camera are shown in Fig. 4-8 (a).

Two types of illumination nonuniformity can be expected to influence the captured image: that due to the camera lens and that due to the copy stand lamps. Both of these can be compensated for by capturing a white reference image under the same conditions that are used for the sample images. A target was constructed from paper coated with a barium sulphate reference white material. Figure 4-8 (b) shows one such profile for the f3 image. An effective illumination profile was then estimated by transforming the signal values via the above photometric correction equations.

The corrected signal is expressed as

$$\hat{s}_i = \frac{\mathbf{f}_i(s(x, y) - d(x, y))}{\mathbf{f}_i((w(x, y)) - d(x, y))}, \quad \text{for } i = 1, 2, \dots, 8 \quad (4-1)$$

where  $s$  is the camera signal,  $d$  is the dark signal,  $w$  is the reference image signal,  $\mathbf{f}$  is the camera compensation equation, and  $i$ -th indicated filter-image number. It should be noted that this simple form of compensation implies that the dark signal simply adds to the signal after detection, and that the illumination profile cascades with the source.

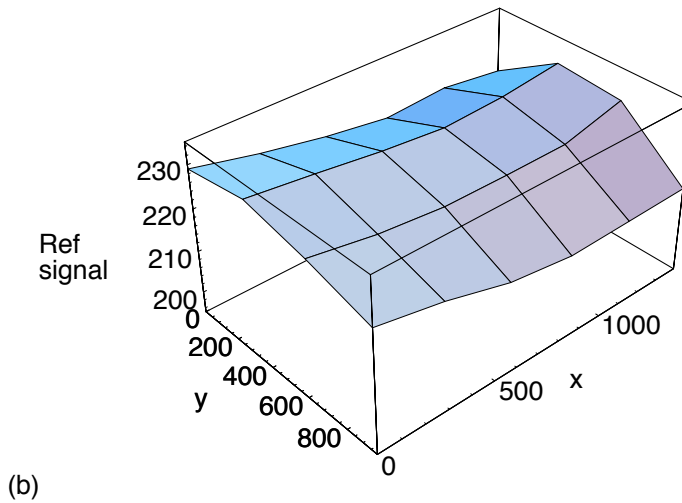
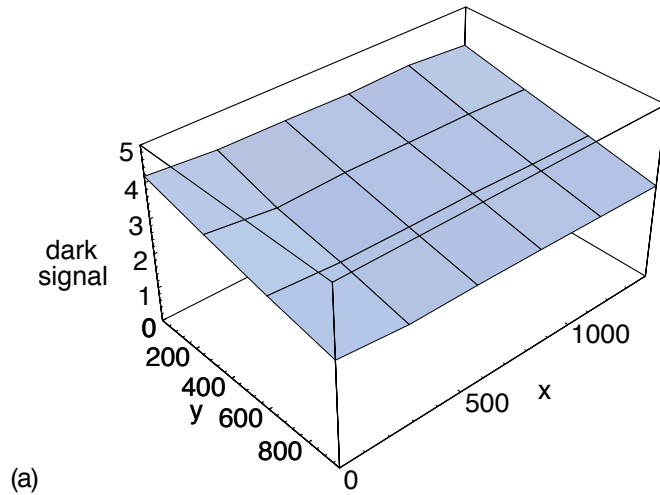


Fig. 4-8: Observed dark-signal and white reference image characteristics for f3 settings, plotted as a function of pixel location. The units are digital counts [0-255].

#### D. Experimental Image Capture

Several multispectral images were captured using the camera assembled as described above. The camera was connected to an Apple Macintosh computer via an SCSI cable. The

exchange of data was accomplished using the Kodak-supplied driver (Kodak DCS 200 Plugin 3.1) and Adobe Photoshop 2.5 software. The camera settings were chosen so as to yield a maximum digital signal without causing signal clipping, and are given in Table 4-1. The maximum signals obtained (for the white sample), however, were far from the maximum digital signal value of 255, as can be seen from the listing in Appendix G. This is due to the fact that changing the camera exposure time by one setting, e.g. from 1/60 to 1/30 sec., doubles the exposure and therefore approximately doubles the detected signal charge. With such coarse exposure adjustments, it was necessary to set the exposures lower than intended to prevent signal clipping at the next higher setting. This is a drawback to using a digital camera whose CCD image detector has different characteristics than the photographic film, around which the Nikon camera controls were designed. Results for the imaging of the Macbeth ColorChecker target will now be discussed in detail, since they demonstrate both the general level of camera performance achieved, and limitations of the system.

The eight image files were captured, as were the equivalent images of the white reference card. Dark frame images were also stored. For each of the ColorChecker files, the mean and standard deviation of the digital signal values corresponding to the area of each of the 24 test colors were computed and stored. This was also done at the same locations for the dark and white reference image sets. Appendix G lists the observed mean signals for each filter capture. Figure 4-8 shows a perspective view of dark and white reference signal values, which are also listed in Appendix G. Figure 4-9 shows prints of the captured ColorChecker chart for all eight filter-records.

Following the procedure described in the previous section, the photometric correction was derived for each filter image. The resulting equations are given in Appendix G. As a

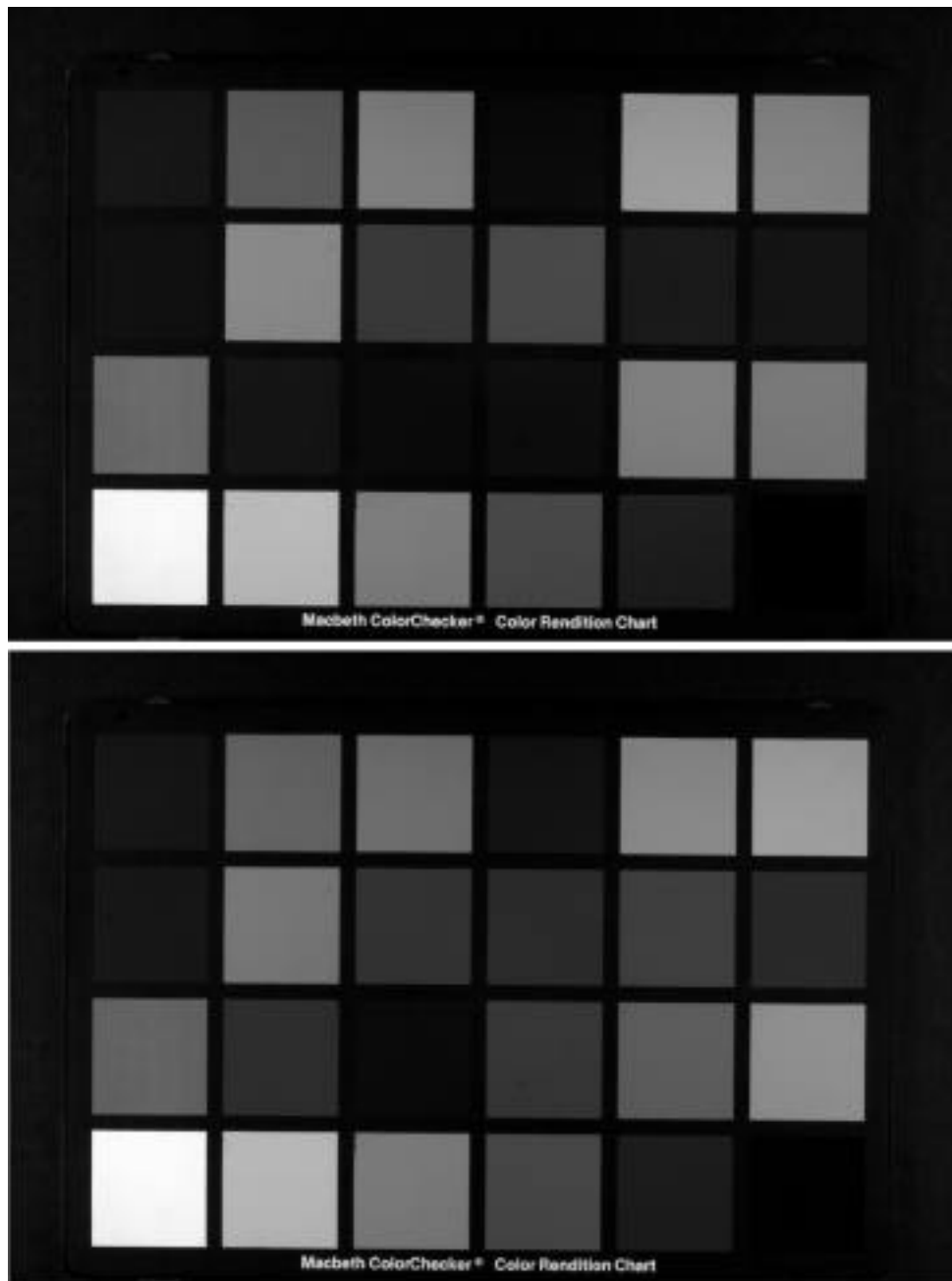


Fig. 4-9 a: Captured images of ColorChecker target with filter 1 (top) and filter 2 (bottom).

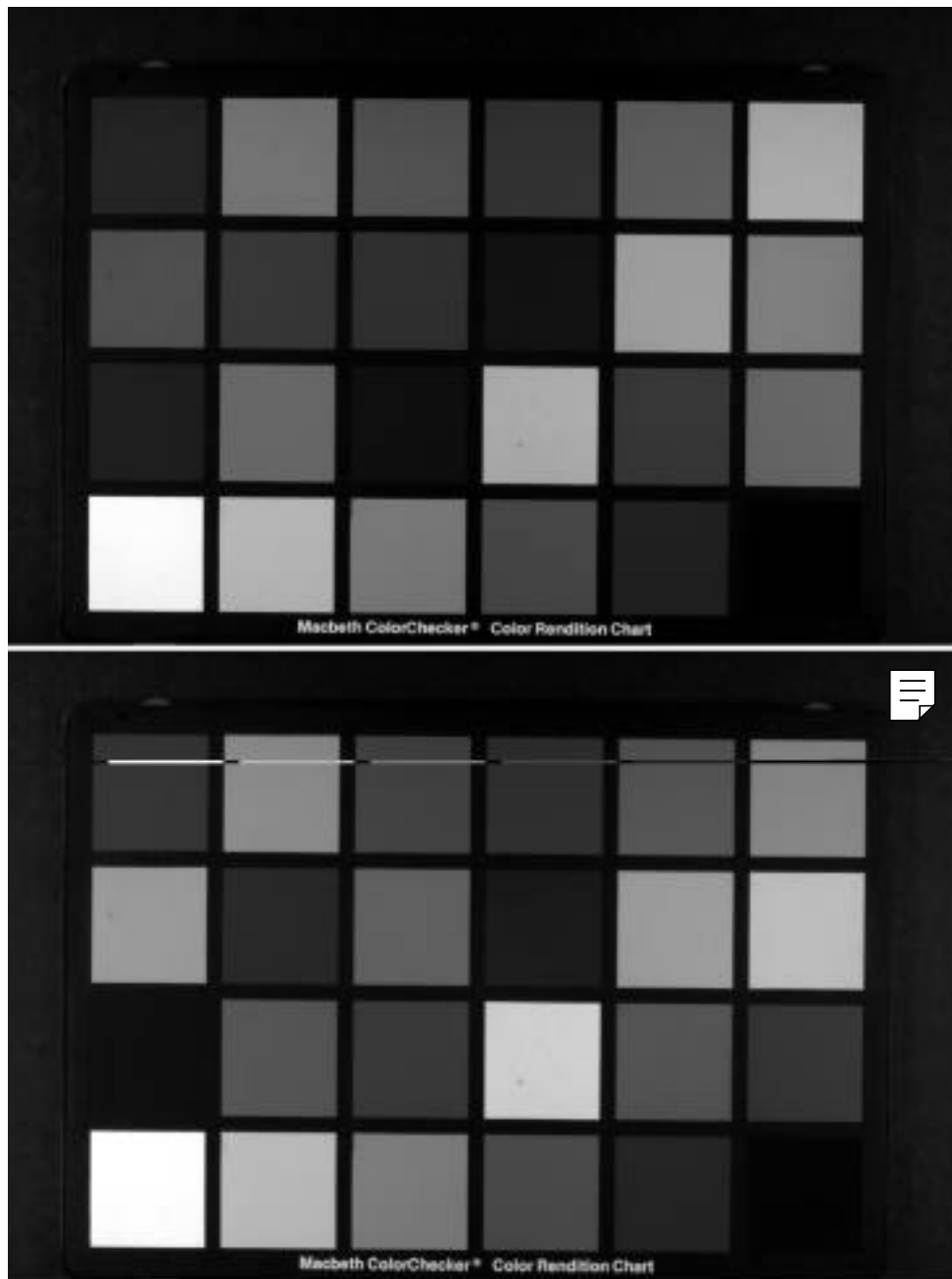


Fig. 4-9 b: Captured images of ColorChecker target with filter 3 (top) and filter 4 (bottom).

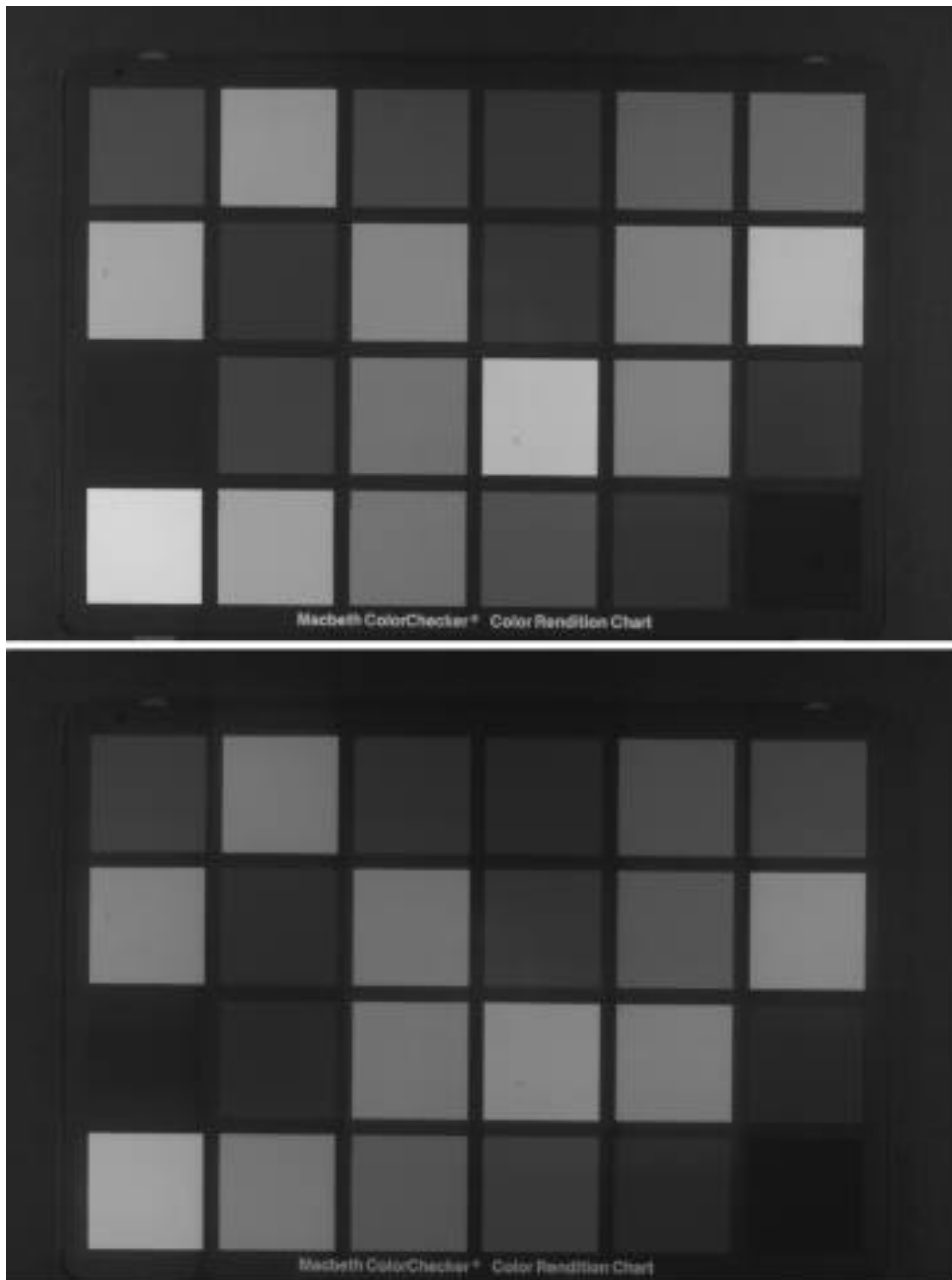


Fig. 4-9 c: Captured images of ColorChecker target with filter 5 (top) and filter 6 (bottom).

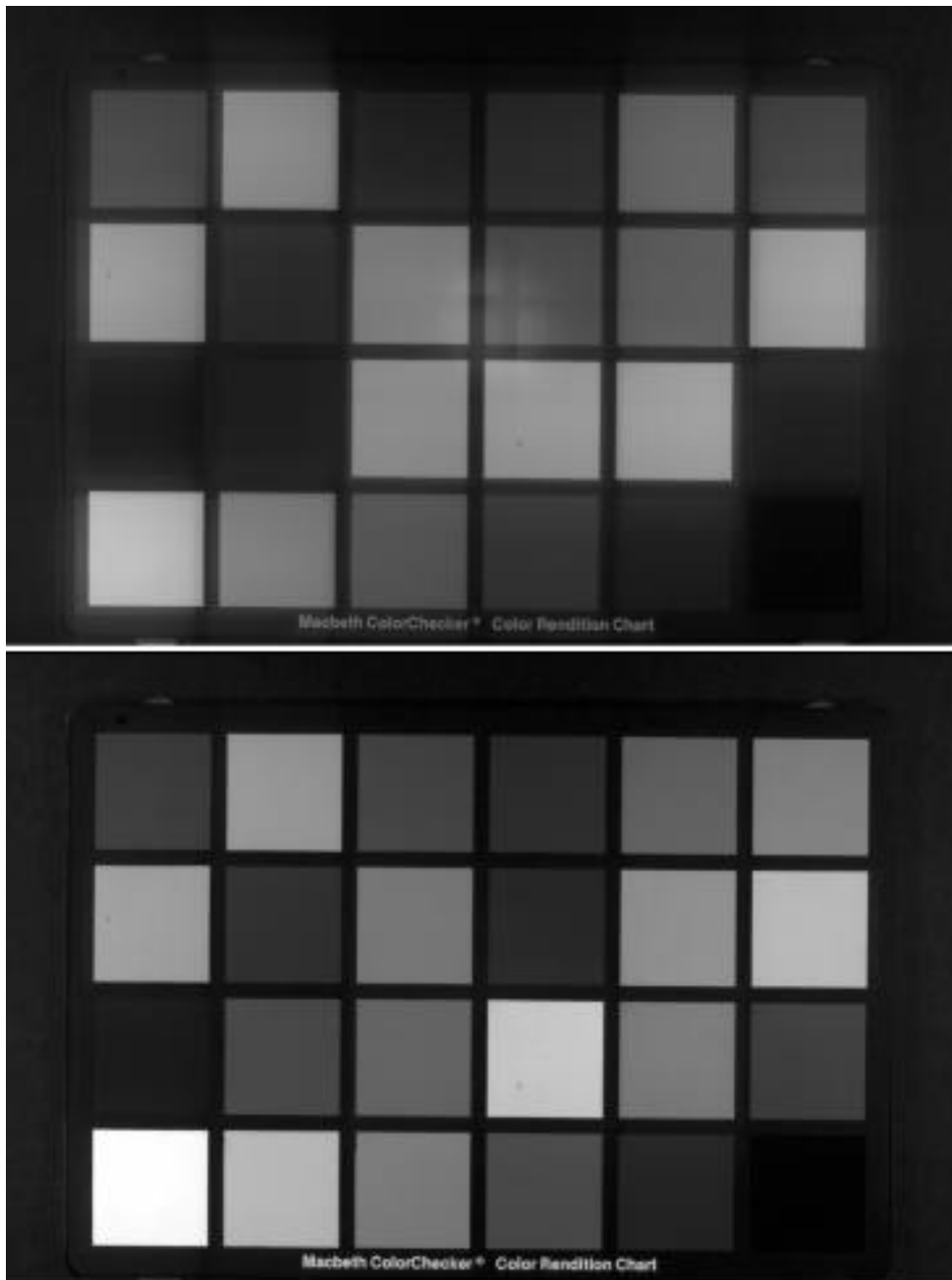


Fig. 4-9 d: Captured images of ColorChecker target with filter 7 (top) and filter 8 (bottom).

measure of the success of this procedure, Fig. 4-10 shows the corrected signal values plotted versus the ideal signal levels for filter number 3. This filter image showed the worst signal-correction performance of the eight. Note that the photometric calibration was not calculated as a fit to these signals, but rather to a set of neutral samples.

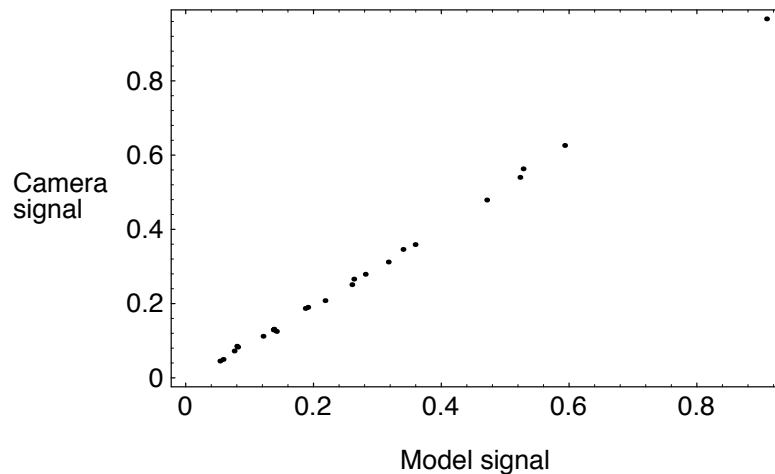


Fig. 4-10: Digital camera signals for the f3 image, after photometric calibration, versus calculated model signals.

### E. Conclusions

A multispectral camera was assembled using a monochrome digital camera, set of narrow-band interference filters, and copy-stand. The spectral sensitivity and photometric response of the camera were characterized. Following a correction of the image data for this response, account was taken for the effective illumination variation across the image field, and the dark signal. This resulted in image data suitable as input for the signal processing described in Chapter II, for spectral and colorimetric estimation. This will be described in the next chapter.

## **V. IMPLEMENTATION: SPECTRAL AND COLORIMETRIC ESTIMATION**

The accuracy of the experimental multispectral camera was assessed by both spectral reconstruction and colorimetric estimation from captured images. The intent was to determine the extent to which this could be done using the transformations, matrices and model equations, that were developed in Chapter II. This set the stage for additional investigations into possible improvements of the system. An optimized PCA transformation based on the actual camera signals was implemented, followed by a simple technique for improving the input signal-to-noise-ratio. Based on the results of Chapter II, the two interpolation methods, MDST and cubic spline, were not applied to the task of spectral reconstruction from the experimental camera.

### **A. Estimation for each pixel.**

The captured signal values for the ColorChecker target were corrected for both the camera photometric response and effective illumination variation across the field. Then sets of contiguous (20 x 20) pixels were used to estimate the spectral reflectance and colorimetric coordinates. The modified PCA method was applied using the **A** matrix of Eq. (2-9), for eight basis vectors and seven camera signals. The average error (n=400) in the estimated spectral reflectance factor plotted versus wavelength, averaged over the 24 color samples, is shown in Fig. 5-1.

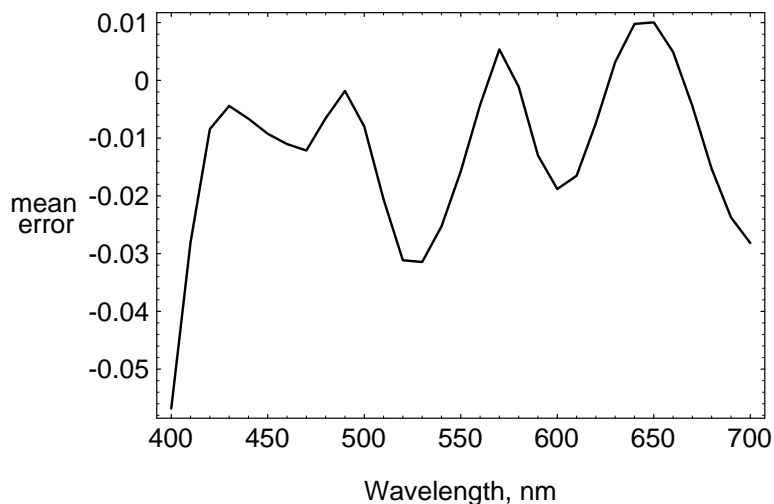


Fig. 5-1: Mean error in the estimated spectral reflectance factor, based on modeled signal path and set of 400 pixel values. Seven camera signals and eight basis vectors were used.

Example estimates of spectral reflectance factor based on a single set of (7) pixel values, for the Cyan and Orange samples are shown in Fig 5-2. It was observed that the estimates from the set of pixel values were similar and not centered about the true measured vector. This is consistent with the mean errors summarized in Fig. 5-1.

The colorimetric estimation was evaluated by calculating the CIELAB coordinates corresponding to the 400 estimated spectral reflectance vectors for each sample color. CIE illuminant  $D_{65}$  was chosen for this calculation, as was the  $10^\circ$  observer. An average error,  $\Delta E_{ab}^*$  was then calculated for the set of 400 estimates per color sample, listed in Appendix H. The errors are seen to be much greater than those expected based on an ideal camera and listed in Appendix A, for the Munsell 37 sample set. This can be ascribed to the image noise levels, particularly at low average signal levels, as shown later in Fig. 6-2.

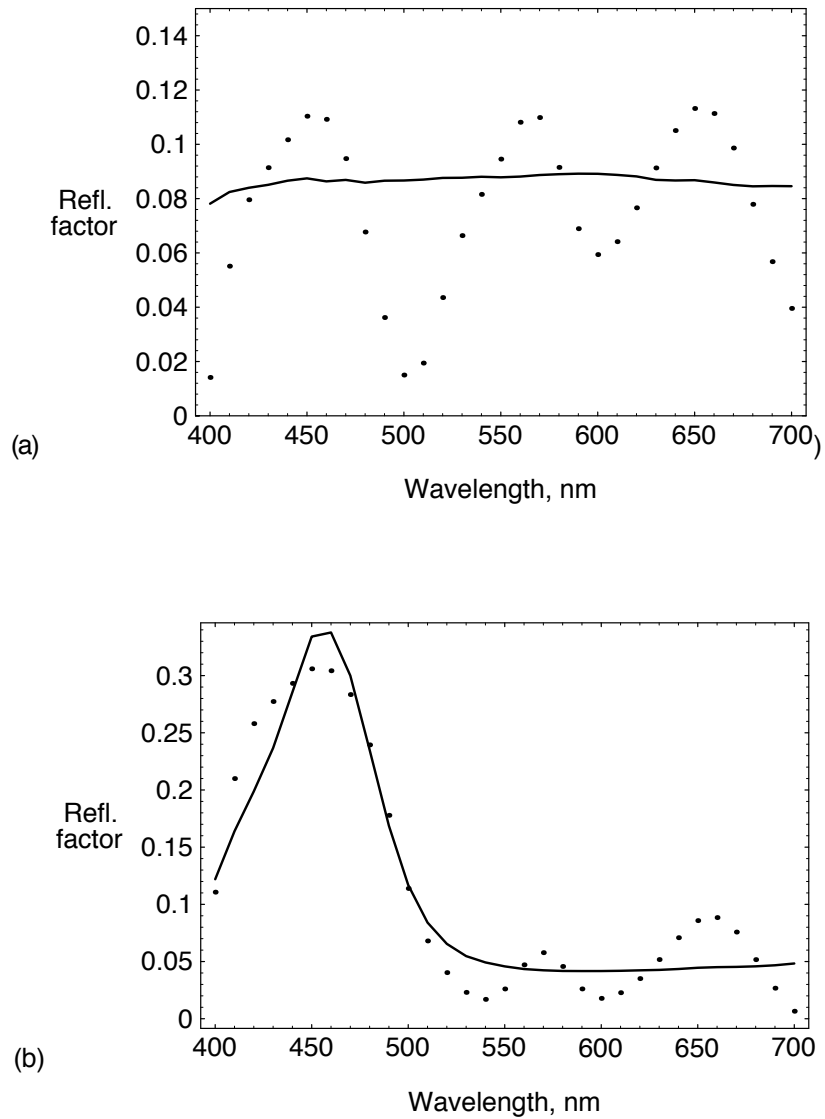


Fig. 5-2: Example estimated spectral reflectance factor for the Neutral 3.5 (a) and Blue (b) samples, following PCA reconstruction based on a single pixel set of seven values. The lines indicate the measurements and the symbols show the estimates.

The two direct colorimetric transformations, given in Eqs. (2-11) and (2-12) were also used to estimate the CIELAB coordinates from each set of pixel values. The results are also listed in Appendix H. As for the PCA-derived values, large errors were computed for these methods.

Since these errors are large compared with those computed from model equations, a simple modification of the signal processing was carried out. In most color-imaging systems, a general image-processing path is identified following an analysis of the likely (model) behavior of each element in the system. This, for example, would identify the form of a needed matrix or non-linear transfer characteristic, and the order in which they operate on the signal values. Prior to processing of images, however, the actual parameter values to be used are derived based on the imaging of a test target, or other standard image data. In this way, for example, elements of a color-correction matrix are calculated so that, for the test data set, improved results might be obtained.

This procedure was followed for the most accurate of the methods under investigation, the modified PCA technique. To do so meant computing an optimized matrix, **A**, based on a set of captured signals. This was done based on independent digital images of a set of Munsell color samples. The resulting matrix used for the spectral reconstruction via Eq. (2-5) and (2-7) was

$$\mathbf{A} = \begin{bmatrix} -1.20 & 0.45 & -3.99 & 5.38 & -7.02 & 2.96 & -1.91 \\ -0.53 & -1.49 & -0.92 & 0.25 & 0.37 & 1.26 & 0.55 \\ -1.20 & -0.30 & 0.89 & 2.90 & -1.99 & 0.55 & -0.87 \\ -0.65 & -0.25 & 2.19 & -2.04 & -0.23 & -0.50 & 1.44 \\ 1.54 & -1.56 & -0.76 & 2.67 & -1.76 & -0.89 & 0.82 \\ -0.98 & 1.15 & -0.28 & -0.96 & 2.58 & -2.79 & 1.23 \\ 1.5 & -2.26 & 2.6 & -4.46 & 4.46 & -1.85 & 0.092 \\ -0.038 & 0.23 & -0.86 & 2.60 & -3.69 & 2.04 & -0.28 \end{bmatrix}. \quad (5-1)$$

This resulted in an approximately 21% reduction in the average CIELAB color-error, as listed in Appendix H. Table 5-1 presents a summary of the above results. The observed errors remained significantly larger than those computed from ideal or model signals. This was largely attributed, particularly for low signal values, to the 8-bit quantization scheme used in the camera, which will be discussed in detail in the next chapter.

Table 5-1: Summary of average  $\Delta E_{ab}^*$  errors following PCA and the direct colorimetric transformations based on ColorChecker pixel data. Column 5 is optimized for the camera signals. CIE illuminant D<sub>65</sub> and the 10° observer were used for the calculation, with each value based on a sample of 400 pixels. Resulting mean errors are averaged over all 24 sample colors.

	PCA	3x3 matrix	3x28 matrix	PCA <sub>opt.</sub>
Ave. $\Delta E_{ab}^*$	5.1	6.7	12.5	4.0
Max.	11.0	16.1	36.3	6.8

### B. Improving system accuracy

As stated above, the 8-bit camera-signal quantization scheme, combined with imager noise, introduced large errors into the signals used for image processing. The measure of system accuracy has been taken as the mean error in the estimated colorimetric estimate based on the sets of recorded pixel values. An alternative measure of colorimetric accuracy was also investigated, however, based on reducing the influence of these errors. Instead of processing the individual pixel values and computing the mean color error after image processing, estimates were computed based on the *mean* camera signal values. While the resultant color-errors would not be a measure of the accuracy of the multispectral image data, they would indicate the level of system performance possible when the effective

image noise is reduced, at the expense of spatial sampling. It should be noted that no additional *a priori* information is needed for this estimation method, nor does it completely eliminate the effect of signal quantization and noise.

From digital image files for the ColorChecker test chart, the average digital signal values were computed for each of the signals, at each of the 24 locations of the test colors. These are given in Appendix G. The image data included the previously used image areas, but extended around them so that the sample size was 1000 pixels. These data were then used to estimate the sample spectral reflectance vector using the modified PCA method.

Examples of two resultant reconstructed reflectance-factor vectors are shown in Fig. 5-3. An obvious improvement over the spectral estimates given in Fig. 5-2 is evident. These two colors, however, present two different problems for the spectral reconstruction from the camera signals. The reconstruction of the Neutral 3.5 sample in Fig. 5-3 (a) shows a relatively large error. This is due to the fact that the spectral reconstruction is based on a least-square fit that estimates the scalar principal components from the camera signals. This simple matrix, however, minimizes the mean-squared difference over the entire population. For samples with low reflectance factor values, the error will usually be a higher fraction of the true value. This in turn results in higher CIELAB errors, due to the slope of the cube-root component of the transformation. In addition, since the matrix is optimized over the entire set of colors it is not guaranteed to give an unbiased estimate for each, so the entire vector can appear to be shifted from the correct spectral reflectance factor.

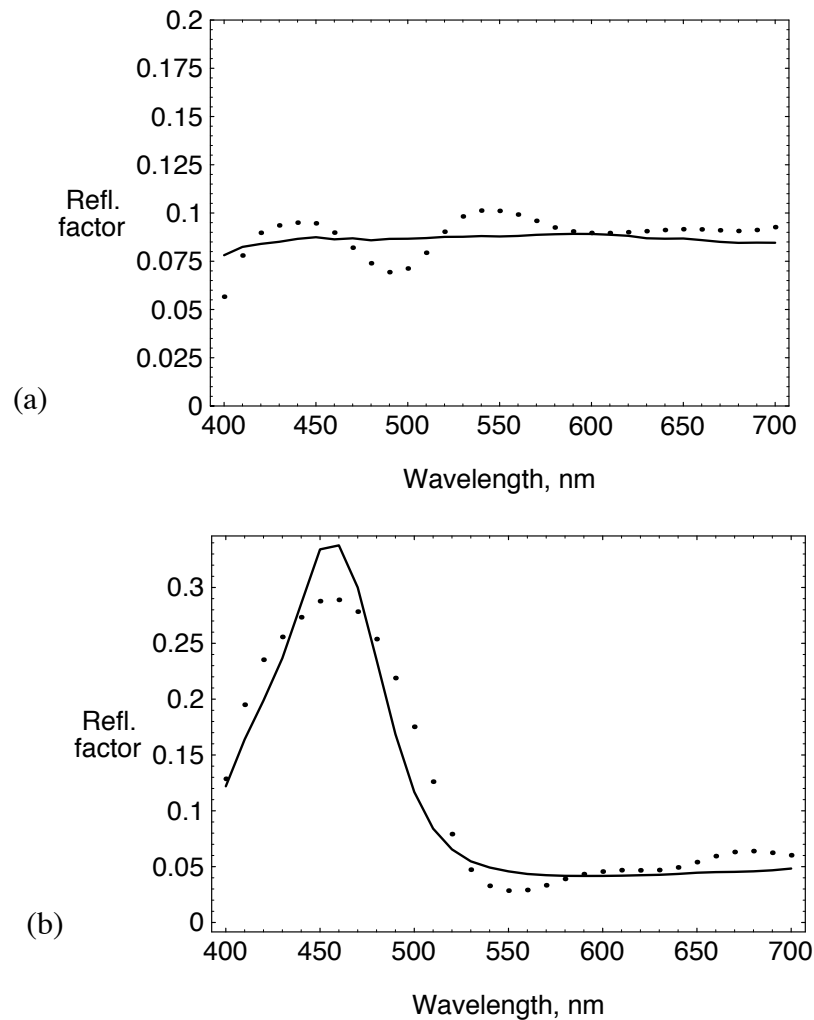


Fig. 5-3: Examples of spectral reconstruction from 7 digital average camera signals using 8 basis vectors. (a) is for the Neutral 3.5 sample, and (b) for the Blue sample. The solid line are the measured reflectance factors.

The blue sample, which showed the largest CIELAB error, has a sharp peak near 460 nm, but the reconstructed vector underestimates this peak. This is partially a result of using camera spectral sensitivities that are wide (approximately 50nm) compared to the signal variation near this peak. The acquisition of spectral information using the set of filters and camera is analogous to the scanning a sample with an detector aperture and sampling the

detected signal at roughly equal intervals. As with spatial scanning, the aperture limits the bandwidth of signal (fluctuations) that will subsequently be recorded by acting as a low-pass spectral filter. In our case the spectral aperture is approximately 50nm in width, and the sampling interval is also 50nm. One way to reduce the smoothing effect of the spectral sensitivities is to use narrower filters, but this has its limitations due to the introduction of aliasing errors into the sampled spectral signal (Gaskill 1978). Narrower spectral sensitivity functions would require a smaller sampling interval (*i.e.*, more signals placed, say, at 30-40 nm intervals). To demonstrate the contribution of the shape of the sensitivities to the underestimation of the peak, Fig. 5-4 shows several estimates.

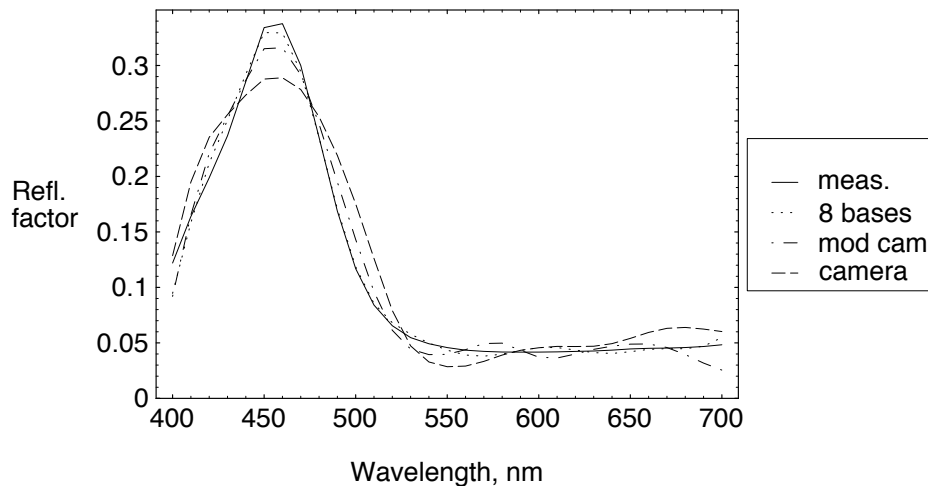


Fig. 5-4: Estimated spectral reflectance factor for the Blue color sample using 8 basis vectors, model camera-, and actual camera signal values.

The reconstruction from the eight basis vectors is seen to closely approximate the measurement, but the calculation based on an ideal camera and set of interference filters underestimates the peak and overestimates the function on either side. The reconstruction based on the actual camera signals is seen to further underestimate the measured data. This is due to all other sources of error, such as residual camera noise and photometric

calibration error due to any record-to-record camera variability. Since the spectral reconstruction from the camera signals is a weighted sum of basis vectors, stochastic noise in the signal values will introduce error that is correlated over adjacent wavelength locations. The net effect will often appear as a further smoothing of the estimate.

The CIELAB coordinates were then calculated from the reconstructed spectral reflectance vectors, for CIE illuminant D<sub>65</sub> and 10° observer. As a test of the robustness of the technique, this was done several times, using several sets of eight basis vectors. In addition to the set derived for the Munsell 37 set, one based on the actual ColorChecker samples was used. These data were expected to share general characteristics with the target but the optimum bases would differ, since one group (Munsell 37) is drawn from the glossy set of Munsell color samples, and the other (ColorChecker) is from the matte samples and would presumably represent different subsets from the ensemble of Munsell pigments. In addition, basis vectors were calculated for a set of DuPont paint samples.

Table 5-2 gives a summary of the results of the above signal processing. The filters listed for each of the sets are those that gave the best performance in terms of color-difference errors. These results express the residual error in the camera signal values, after photometric and illumination correction, in terms of a colorimetric error. It is concluded that the observed level of performance is not very sensitive to the set of basis vectors, if chosen from similar materials. From the standpoint of system design, it is of minor importance how many basis vectors are used to derive the spectral reconstruction, since they are intermediate parameters. It is natural to ask, however, about the relative influence of the number of camera signals versus basis vectors. Fig. 5-5 shows a plot of the median and maximum color-difference error as a function of the number of vectors used for the ColorChecker set. It is observed that the values of camera signals limits the accuracy of the colorimetric information beyond five signals for this set of colors.

Table 5-2: CIELAB  $\Delta E_{ab}^*$  errors for spectral reconstruction from experimental camera signals for the Macbeth ColorChecker target via 3 sets of basis vectors. The numbers, (1 2 ...) indicate which filter-signals were used, and were consistent for all sets. Eight vectors were used for all calculations.

Basis set	number of. filters	mean	median	rms	maximum
ColorChecker	8	1.68	1.74	0.86	3.44
	7 (1 2 3 5 6 7 8)	1.80	1.81	0.95	3.70
	6 (1 2 3 5 7 8)	1.82	1.77	0.90	3.40
	5 (1 2 3 7 8)	2.02	1.82	1.17	5.19
	4 (1 2 3 5)	2.30	1.20	1.34	5.90
Munsell 37	8	1.67	1.74	0.85	4.13
	7	1.77	1.77	0.91	3.86
	6	1.76	1.68	0.89	3.52
	5	1.96	1.67	1.13	5.20
	4	2.28	1.92	1.39	5.21
DuPont paints	8	1.70	1.64	0.83	4.31
	7	1.77	1.79	0.83	4.27
	6	1.79	1.68	0.83	3.57

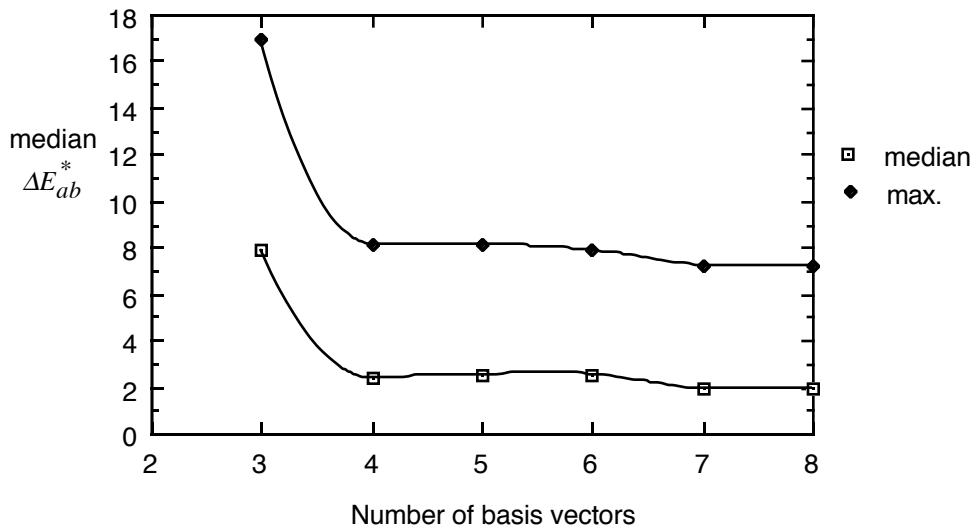


Fig. 5-5: Mean and maximum  $\Delta E_{ab}^*$  following modified PCA spectral reconstruction from camera signals, versus the number of basis vectors used. The set of seven signals was used.

### **C. Conclusions**

Substantial average color errors were observed when estimating the spectral reflectance factor and colorimetric coordinates from captured images from the experimental camera. Using an optimized signal processing path for the PCA method yielded a modest improvement. Reducing the effect of input image noise, and quantization by averaging the input signals, when combined with an optimized signal path, however, resulted in color errors of  $\Delta E_{ab}^* < 2$ , still greater than those predicted by the model calculation of Chapter II.

## **VI. IMPLEMENTATION: SIGNAL QUANTIZATION AND IMAGE**

### **NOISE**

In this chapter the precision of the multispectral camera system is investigated. Direct calculation of image noise is available through the statistics for nominally uniform areas of the input image, and corresponding estimated parameters for each pixel. In addition, attention is turned toward camera signal quantization and its contribution to the signal uncertainty.

#### **A. Observed camera-signal noise and quantization**

The camera-induced image noise characteristics were first investigated by computing the rms pixel-to-pixel signal fluctuations for the uniform areas of the color samples of the ColorChecker target. To avoid the introduction of actual image optical (signal) fluctuations, however, the rms noise was computed from digital images that were acquired with the target out of focus.

As explained in Chapter IV, a single multispectral image the camera exposure time was varied with filter-record to maximize the optical signal at the imager. This motivated a first investigation into the extent to which image exposure time, i.e., CCD imager integration time, influenced the image noise characteristics. The attempt was made to vary the exposure time over a wide range, but to compensate for this by stopping down the lens. In this way, the rms noise, could be compared for various camera settings, but at similar mean signal levels. The camera was operated without an interference filter, but with two neutral-density optical filters in front of the lens, so as to simulate signal levels equivalent to those used for multispectral imaging. The combined optical density of the two filters was 1.1. The intent was to evaluate the camera-induced noise, so the ColorChecker target was captured with the lens focused approximately 0.5 m. behind the sample. Four images were acquired and

the statistics computed. The results are shown in Fig. 6-1, and indicate that there was no appreciable or consistent increase in image noise as the exposure time was increased over a range of approximately 30:1. This was taken to indicate that the noise characteristics would not vary between filter-records.

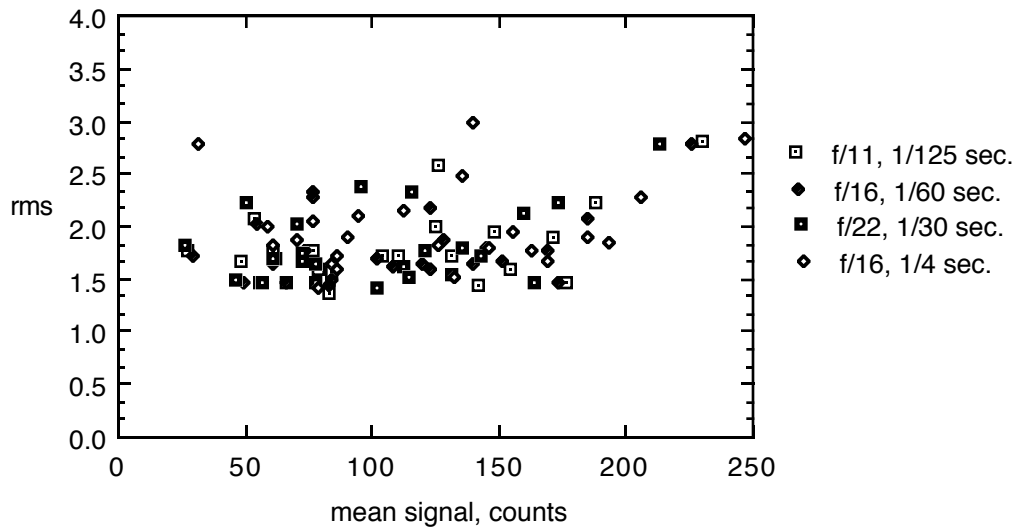


Fig. 6-1: Observed rms noise levels for capture of ColorChecker target, for several images taken varying the camera exposure and lens f/number settings.

Pooling the data from all eight image records, Fig. 6-2 shows the rms values plotted against the mean digital signal value. Comparing these data with the simple model characteristic of Fig. 3-10, or the form of Eqs. (3-31) and (3-32 b), relatively high noise levels for low average signal levels were observed. Examination of the distributions of signal levels for these dark samples, however, revealed several unpopulated signal levels. This is evidence of an effective signal quantization interval greater than that implied by the 8-bit encoding of the digital signal at low signal levels. These missing values are listed in Table 6-1, and are evident from the histograms shown in Fig. 6-3.

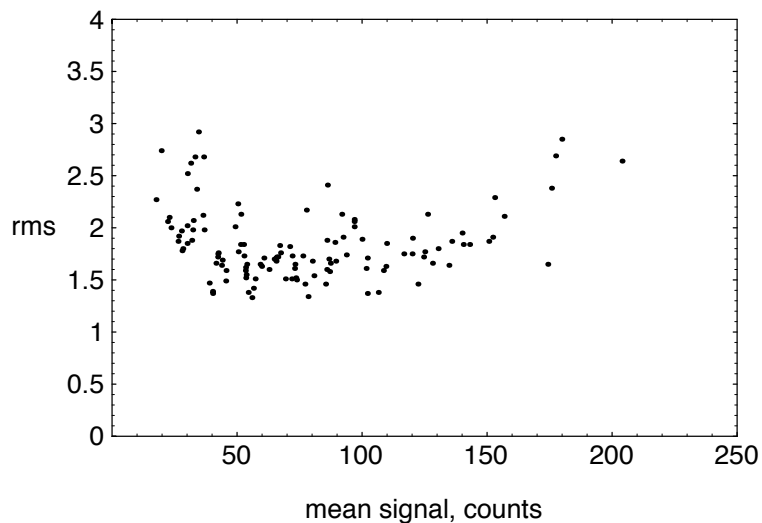


Fig. 6-2: Observed rms noise for capture of ColorChecker target, with all eight image records were pooled. Units are in digital counts [0-255].

Table 6-1: The unpopulated (8-bit encoded) digital signal levels that were observed for the camera images of several steps of a photographic step tablet.

step level	mean	unpopulated levels
1	15.1	1-6, 8-10, 12, 13, 15, 16, 18, 19, 21
2	36.3	28, 30, 31, 32, 34, 36, 38, 39
3	49.1	43, 45, 48, 51, 53
4	65.5	63, 65, 67, 71, 74,

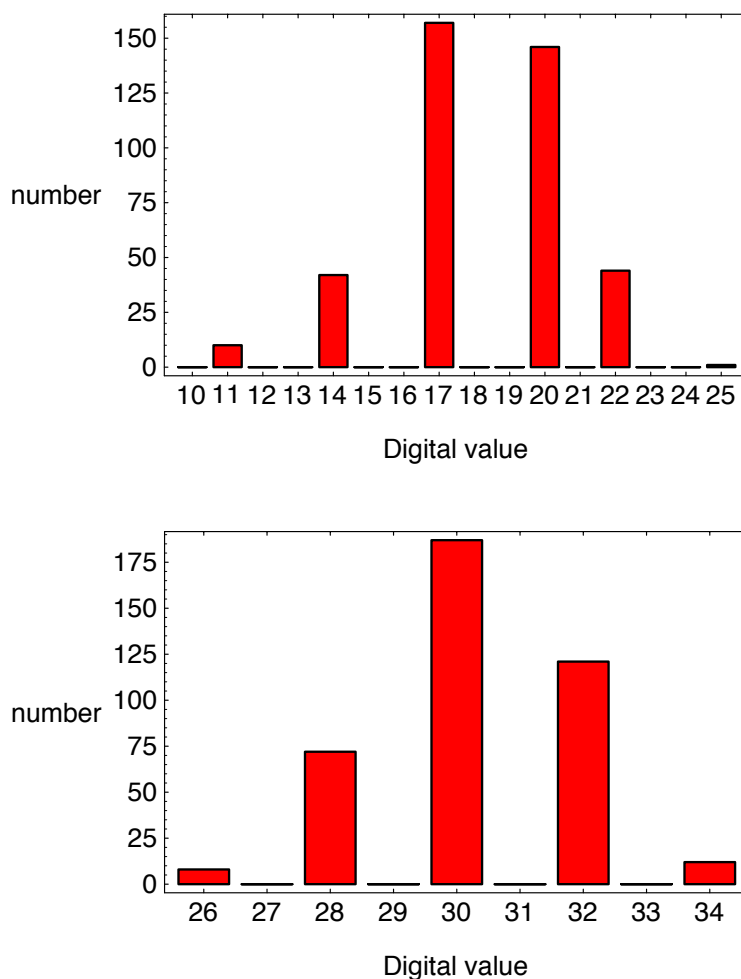


Fig. 6-3: Example histograms of pixel values for two uniform image areas ( $n = 400$ ).

Referring to the camera architecture of Fig. 4-6, it was hypothesized that the coarse image quantization was due to a discrete look-up table being applied prior to the final 8-bit quantization. If there are equal numbers of equally-spaced levels on either side of the LUT, then missing output values occur when the slope of table is greater than unity. More specifically, the quantization interval is equal to the slope, if all units are kept in terms of the nominal (8-bit) output quantization interval. Conversely, if we assume that the original quantization is uniform, then the missing values give a clue as to the form of the table

transformation, since each discrete output level is projected back to available primary quantization level. The first step is to compute the effective quantization as a function of output (8-bit) level. This was done by observing the histograms of uniform image areas captured from the step tablet. These data were fit to an equation of the form

$$\Delta = \frac{16.6}{(v + 5)^{0.56}}$$

where  $\Delta$  is the quantization interval and  $v$  is the mean signal value shown in Fig. 6-4.

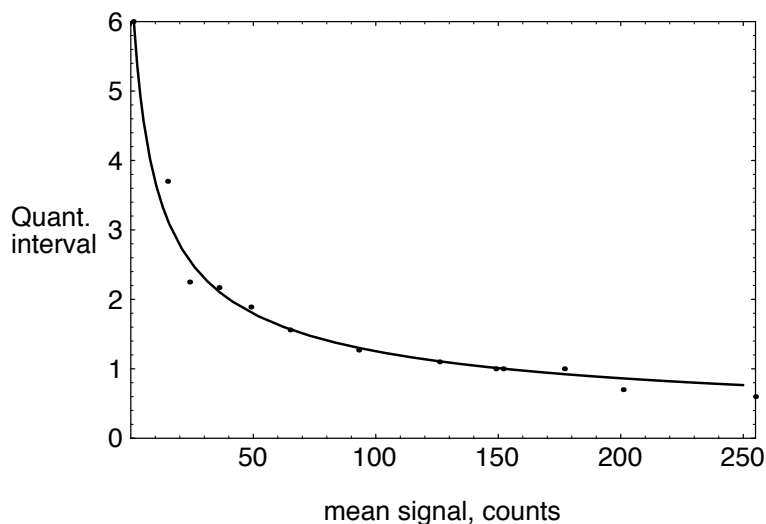


Fig. 6-4: Observed camera signal quantization interval in units of 8-bit counts.

The form of the first derivative of the quantization function (Fig. 6-4) is taken as the transformation introduced by the camera LUT. This is shown in Fig. 6-5. It should be noted that this is very similar to the camera photometric response that was evaluated directly from camera signals, as described in chapter 4. The inverse of this characteristic forms the photometric correction curve (see Fig. 4-7).

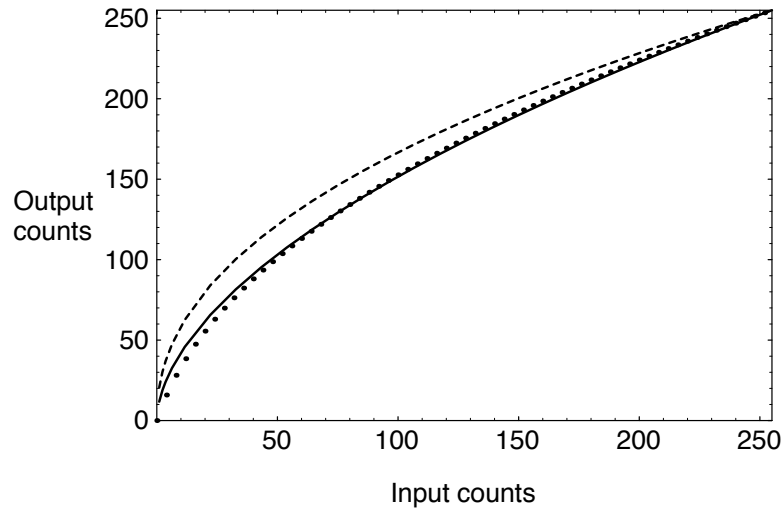


Fig. 6-5: The internal camera look-up table that was estimated from the observed signal quantization. The curve (dots) is the integral of the quantization data of Fig. 6-4. This is compared with typical camera tables that compensate for CRT characteristics for  $\gamma = 1.8$  (solid line) and 2.2 (dashed line).

The effective noise levels associated with primary signal detection and signal readout can be estimated by propagating the observed rms noise levels of Fig. 6-2 back through the inverse of Fig. 6-5, or the above photometric response. Since this is a univariate transformation, this is equivalent to dividing the observed camera rms noise by the function of Fig. 6-4. The results are shown in Fig. 6-6. These data can be used to model the intrinsic imager noise in terms of the three components of Eq. 3-33,

$$\sigma = \sqrt{0.24 + 0.015 v + 3.78 \times 10^{-6} v^2}. \quad (6-1)$$

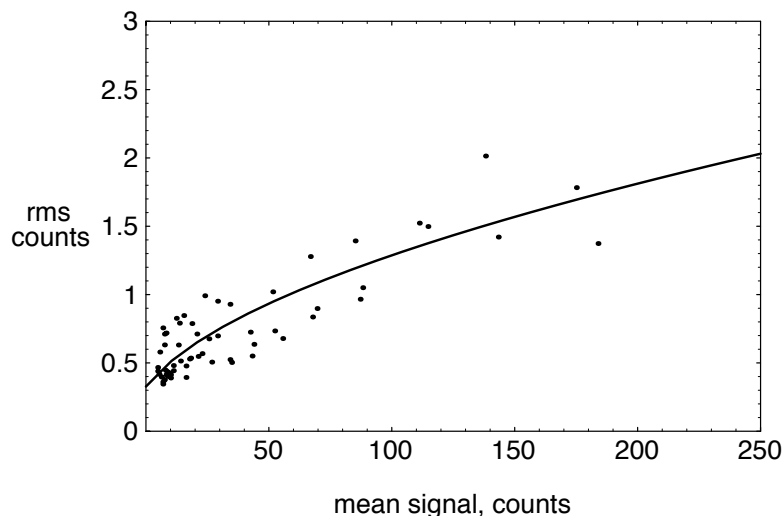


Fig. 6-6: The result of propagating the observed rms image noise to effective imager noise levels. The line indicates Eq. (6-1).

### B. Error in spectral and Colorimetric estimates

The above analysis allows the modeling of the effective noise sources of the imager, which is important if improved performance is to be addressed, as in chapter VII. Actual captured images, however, are burdened with the observed levels shown Fig. 6-2. The influence of this camera-signal noise on the estimates was computed directly from the images captured for the ColorChecker chart, as described in Chapter VI.

Following photometric, illumination, and dark signal compensation the spectral reflectance factor was estimated for each pixel in the 24 sets of 400 pixel values. The RMS variation in the estimated spectral reflectance for a set of 400 pixel values is shown in Fig. 6-7. The corresponding colorimetric errors derived from these spectral estimates and those due to the two direct transformations are listed in Tables I-1 and I-2 in Appendix I. A summary is also given in Table 6-2.

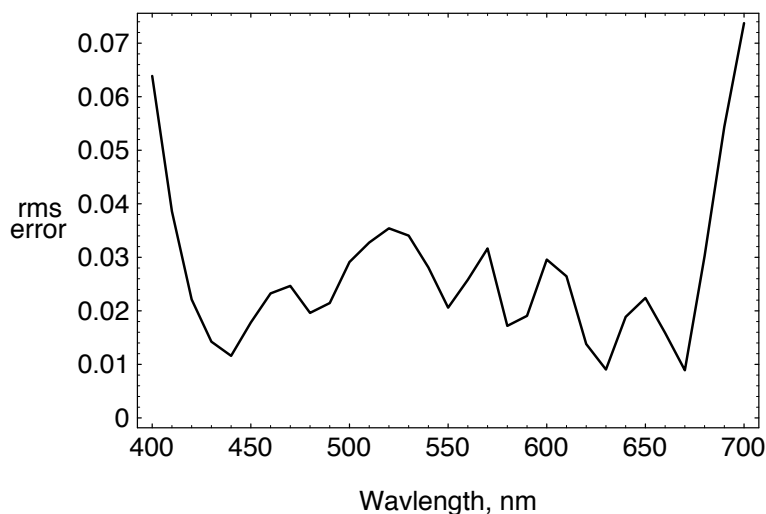


Fig. 6-7: RMS error in the estimated spectral reflectance factor, based on modeled signal path and set of 400 pixel values. Eight basis vectors and seven camera signals were used.

Table 6-2: Summary of the CIELAB errors for estimates computed from ColorChecker pixel data, for PCA and the two direct methods. Column 5 is optimized for the (mean) camera signals. CIE illuminant  $D_{65}$  and the  $10^\circ$  observer were used for the calculation, with each value based on a sample of 400 pixels. Resulting rms and average  $\Delta E_{ab}^*$  errors are averaged over all 24 sample colors.

Sample	$\sigma_{L^*}$	$\sigma_{a^*}$	$\sigma_{b^*}$	$E[\Delta E_{ab}^*]$	$E[\Delta E_{ab}^*]_{opt.}$
PCA	0.6	2.7	2.7	3.9	3.5
Simple direct	2.0	2.8	2.8	4.5	
complex direct	12.2	12.2	3.8	18.2	

These results indicate that the PCA-derived estimates exhibited the lowest average RMS error. A comparison of the two direct methods, however, indicates the noise-penalty associated with the complex model calculation. Consider the matrix of weights for the

complex direct transformation, given in Eq. (2-12b). While the use of this model was motivated by reduced model errors, as indicated in Table 2-3, the model data is effectively ‘error-free’. The introduction of even minor bias or stochastic error into the camera signals results in an amplification due to the variation in magnitude of the weighting coefficients. This results in the addition, and more importantly, subtraction of large numbers which leads to large errors in the result.

### **C. Verification of error-propagation analysis for camera signals**

The observed error in CIELAB that results from the processing of actual camera signals, summarized in Table 6-2, can be used to assess the validity of the error-propagation analysis of Chapter III. This was done for each of the ColorChecker color samples as captured by the seven-channel multispectral camera. As described above, the signal values for each of 400 pixels were processed to estimate the sample spectral reflectance factor. From these data the corresponding CIELAB coordinates were computed, assuming CIE illuminant  $D_{65}$  and the  $10^\circ$  observer. From the resultant 400 CIELAB coordinates the sample covariance matrix was calculated for each of the twenty-four colors.

The error-propagation technique was implemented by first calculating the covariance matrix for the seven camera signals,  $\Sigma_s$ , for each color sample. The image fluctuations in each signal were essentially independent, as indicated by a diagonal covariance matrix. This is as expected, since each signal resulted from an independent camera image exposure, although a fixed-pattern component could introduce covariance. The covariance matrix for the camera signals was propagated to equivalent statistics in spectral reflectance factor by

$$\Sigma_r = \Phi \mathbf{A} \Sigma_s \mathbf{A}^T \Phi^T, \quad (6-2)$$

where  $\mathbf{A}$  is give in Eq. (2-9). The square-root of the diagonal elements of  $\Sigma_r$  give the rms

error as a function of wavelength for the spectral reflectance factor, equivalent to the plot of Fig. 6-7. From  $\Sigma_r$  the covariance matrix for the tristimulus values was calculated using ASTM weights,  $\mathbf{M}$ . As in Eq. (3-10) the tristimulus values covariance matrix is given by

$$\Sigma_t \cong \mathbf{M}\Sigma_r\mathbf{M}^T, \quad (6-3)$$

where the matrix of spectral weights is

$$\mathbf{M} = \begin{bmatrix} \bar{x}_1 & \bar{y}_1 & \bar{z}_1 \\ \vdots & \vdots & \vdots \\ \bar{x}_n & \bar{y}_n & \bar{z}_n \end{bmatrix}.$$

This was followed by the transformation to CIELAB. As in Eq. (3-16) the CIELAB covariance matrix is given by

$$\Sigma_{L^*a^*b^*} \cong \mathbf{N}\mathbf{J}_{f(t)}\Sigma_t\mathbf{J}_{f(t)}^T\mathbf{N}^T, \quad (6-4)$$

where

$$\mathbf{J}_{f(t)} = \frac{1}{3} \begin{bmatrix} \mu_X^{-2/3}X_n^{-1/3} & 0 & 0 \\ 0 & \mu_Y^{-2/3}Y_n^{-1/3} & 0 \\ 0 & 0 & \mu_Z^{-2/3}Z_n^{-1/3} \end{bmatrix}, \text{ and } \mathbf{N} = \begin{bmatrix} 0 & 116 & 0 \\ 500 & -500 & 0 \\ 0 & 200 & -200 \end{bmatrix}.$$

Combining Eqs. (6-2)-(6-4),

$$\Sigma_{L^*a^*b^*} \cong \mathbf{N}\mathbf{J}_{f(t)}\mathbf{M}\Phi\Lambda\Sigma_s\mathbf{A}^T\Phi^T\mathbf{M}^T\mathbf{J}_{f(t)}^T\mathbf{N}^T. \quad (6-5)$$

While the RHS of Eq. (6-5) includes ten matrix-multiply operations, it should be noted that several can be pre-computed if the calculation is to be performed for several color samples. For example the linear operations,  $\mathbf{M}\Phi\mathbf{A}$  and  $\mathbf{A}^T\Phi^T\mathbf{M}^T$  could be computed once and stored. The nonlinear steps involving  $\mathbf{J}_{f(\mathbf{t})}$  and its transpose must be calculated for each sample.

Equation (6-5) was evaluated for each of the ColorChecker color samples, based on the observed camera-signal covariance matrix,  $\Sigma_s$ . Good agreement was found between the sample covariance matrix calculated from the sets (n=400) of pixel data, and the results of the error-propagation. For example, for the Cyan sample the sample covariance matrix was

$$\Sigma_{L^*a^*b^*} = \begin{bmatrix} 0.17 & -0.47 & 0.26 \\ -0.47 & 4.58 & -1.75 \\ 0.26 & -1.75 & 1.71 \end{bmatrix}.$$

The equivalent second-order statistics computed via Eq. (6-5) are

$$\Sigma_{L^*a^*b^*} = \begin{bmatrix} 0.17 & -0.48 & 0.27 \\ -0.49 & 4.66 & -1.79 \\ 0.27 & -1.80 & 1.73 \end{bmatrix}.$$

A measure of the variation (in 3-space) expressed by the covariance matrix is the generalized variance, which is the determinant of the covariance matrix (Jackson 1991). The volume associated with the error-distribution is proportional to the square-root of the generalized variance. Table 6-3 shows the % difference in the two calculations of rms CIELAB fluctuations and generalized standard deviation. The small differences indicate agreement for all ColorChecker color samples. Ignoring signal quantization, the 400 signal values for each color represent a sample from the population values, if the fluctuations are seen as stochastic. Therefore the covariance matrix computed directly from these values, is

actually an estimate based on a sample size of 400, and subject to a sampling error which will depend on the underlying distribution of pixel values.

Table 6-3: Comparison of the standard deviation in the CIELAB coordinates for sample pixel data (n= 400) and error-propagation methods. The fourth column is for the generalized  $\sigma$ , and the difference is calculated by  $(\sigma_{error\ prop.} - \sigma_{pixel}) / \sigma_{pixel}$ .

Color	% RMS difference			
	$\sigma_{L^*}$	$\sigma_{a^*}$	$\sigma_{b^*}$	gen. $\sigma$
Dark skin	-0.8	-1.9	-0.8	-1.5
Light skin	-0.9	-0.8	-0.1	1.0
Blue sky	-0.2	-0.1	0.4	0.2
Foliage	0.2	0.2	-0.9	-1.1
Blue flower	0.6	0.9	0.2	0.8
Bluish green	-0.4	0.3	-0.8	0.4
Orange	0.1	-1.5	-1.5	-3.0
Purplish blue	0.9	2.0	1.3	1.9
Moderate red	-1.0	-1.2	-1.9	-1.4
Purple	0.1	-0.9	-0.9	-1.8
Yellow green	-0.5	0.1	-0.6	-0.2
Orange yellow	-0.8	-1.3	-4.5	-5.4
Blue	-0.1	-1.4	-0.3	-0.8
Green	0.1	-0.3	-0.4	-0.2
Red	-1.0	-1.7	-1.3	-2.4
Yellow	0.4	-0.5	-2.8	-3.5
Magenta	0.9	0.6	0.4	0.4
Cyan	0.7	0.9	0.5	0.7
White	0.2	-0.5	0.2	-0.2
Neutral 8	-0.8	-2.0	-1.0	-1.6
Neutral 6.5	0.1	0.6	-0.4	0.6
Neutral 5	-0.5	-0.7	-0.2	-0.6
Neutral 3.5	0.7	-0.2	0.4	-0.1
Black	-2.8	-2.1	-3.1	-4.8

#### **D. Conclusions**

The rather coarse camera-signal quantization lead to several unpopulated low signal levels. This in turn increased the apparent rms noise. Despite this, the modified PCA and simple direct signal paths yielded moderate rms noise levels, particularly when compared with the mean (bias) errors reported in Chapter V. A substantial increase in colorimetric image noise was propagated for the complex direct transformation, as a consequence of the extended form and coefficients of the defining equations.

A comparison of second-order image noise statistics derived from processed pixel data and error-propagation indicated good agreement for all ColorChecker color samples. This was taken as indicating that the multivariate error-propagation analysis can be applied over a wide range of image acquisition and image processing applications.

## VII. MODELING IMPROVED CAMERA PERFORMANCE

In the previous chapter it was demonstrated how the experimental camera could be used to derive both spectral and colorimetric image information. The observed imager noise and signal quantization, however, place limitations on both the system accuracy and precision. This will now be addressed in a systematic way by assessing the errors due to both imager noise and signal encoding. The objective is to provide insight as to the influence of specific design choices, such as number of bits used to encode the signals, on system performance. After addressing signal quantization errors, the multivariate error propagation of Chapter III is applied to the system model and signal processing described in Chapter II. In addition, these results will then be discussed for the multispectral imaging of metameric color samples.

### A. Quantization

Image quantization is the encoding of each sample of a continuous sampled signal, e.g. radiance, as one of a limited number of discrete values. This represents a loss of information, in that an error is introduced when the quantized signal is interpreted as, or compared with, the original sampled image. The simplest and most common procedure is uniform quantization. Here each sample is compared to a set of levels that are equally spaced over the available signal range, and assigned to the nearest one. Nonuniform quantization is also common, however, as part of image compression (Pratt 1978) or as a companding step to compensate for later elements in an imaging system, such as the photometric response of a CRT display (Berns *et al.*1993 ). Nonuniform quantization is usually implemented in two steps; a primary uniform quantization followed by a discrete transformation, as shown in Fig. 4-6.

Image quantization has historically been analyzed as both a source of stochastic and deterministic error. These two views of the same signal transformation arise from differing imaging objectives. For systems where objectives can be cast in terms of signal detection and statistical information preservation, such as medical imaging, reconnaissance, and astronomy, then the error introduced by quantization is often seen as an added signal-independent stochastic source with an approximately uniform probability distribution. The width of this distribution is equal to the quantization interval (Oppenheim and Schaffer 1975, Burns 1989, Holst 1996) corresponding to the range of a rounding error, i.e.  $-\frac{\Delta v}{2} \leq e \leq \frac{\Delta v}{2}$ . For a random variable of uniform or rectangular distribution, and width parameter  $\Delta v$ , the variance is given by (Dougherty 1990)

$$\sigma^2 = \frac{\Delta v^2}{12}.$$

The rms quantization noise is found from the square-root of the RHS of this equation,

$$\sigma = \frac{\Delta v}{\sqrt{12}}. \quad (7-1)$$

For the case of uniform quantization using  $b$  bits ( $2^b$  discrete levels) to encode each pixel, the interval has a width  $(v_{max} - v_{min})/2^b$ . Eq. (7-1) then becomes

$$\sigma = \frac{(v_{max} - v_{min})}{2^b \sqrt{12}}, \quad (7-2)$$

where the available signal range is  $v_{max} - v_{min}$ . As an example, the quantization noise introduced by 8-bit encoding is  $0.0011(v_{max} - v_{min})$ , or 0.29 digital counts on a [0-255] scale.

Viewing error introduced by signal quantization as a stochastic noise source ignores the fact that all the resulting pixel values are rounded to a *finite number* of levels. When viewed, a quantized image, particularly in slowly-varying regions or graphical elements, shows the discrete levels as artifacts that detract from the image information. Consequently, it is the effective quantization interval that is often compared with (visually) detectable intensity or color-differences (Stokes *et al.* 1992, Sezan *et al.* 1987). For many applications the requirement that each quantization interval is not visible, i.e., not introduce visible artifacts, is more stringent than one based on a comparison of the rms quantization noise with image fluctuations from other sources, such as scene content and image detection.

When image signals are quantized prior to other signal processing, the resultant error can be propagated through the signal path in a similar way to that used for stochastic error propagation. Now however, the errors form a finite set, are deterministic, and represent a bias that will usually depend on the signal levels. For an  $m$ -record image acquisition, the set of quantization intervals for a given signal location (in  $m$ -space) is that spanned by incrementing and decrementing each of the  $m$  signals by one interval, and comparing it with a reference location. This results in  $3^m - 1$  intervals. For a given system the effective quantization intervals can easily be computed by processing them as ordinary pixel values.

#### 1. Three-channel Camera/colorimeter

Consider the simple three-record colorimeter which detects sample tristimulus values,  $X$ ,  $Y$ ,  $Z$  as described in Chapter III.A.5. For a given signal quantization scheme and reference color, the set of  $3^3 = 27$  signal values is

$$\{(X_{ref}, Y_{ref}, Z_{ref}), (X_{ref} + \Delta_X, Y_{ref}, Z_{ref}), (X_{ref} - \Delta_X, Y_{ref}, Z_{ref}), \\ (X_{ref} + \Delta_X, Y_{ref} + \Delta_Y, Z_{ref}), \dots, (X_{ref} + \Delta_X, Y_{ref} + \Delta_Y, Z_{ref} + \Delta_Z)\},$$

where  $(X_{ref}, Y_{ref}, Z_{ref})$  are the reference signal values and  $(\Delta_X, \Delta_Y, \Delta_Z)$  are the quantization intervals for each signal. Each of the above set of signals can be transformed into a secondary color-space and the set of 26 differences (from the reference signal) computed. This was done for the transformation from tristimulus values to CIELAB. Figure 7-1 shows the results of uniform quantization using various numbers of encoding bits for the achromatic (neutral) axis in CIELAB. The quantization color-difference is presented as the average  $\Delta E_{ab}^*$ , which will be a function of the reference  $L^*$  value because of the nonlinear transformation between  $X, Y, Z$  and  $L^*, a^*, b^*$  as in Eq. (3-13).

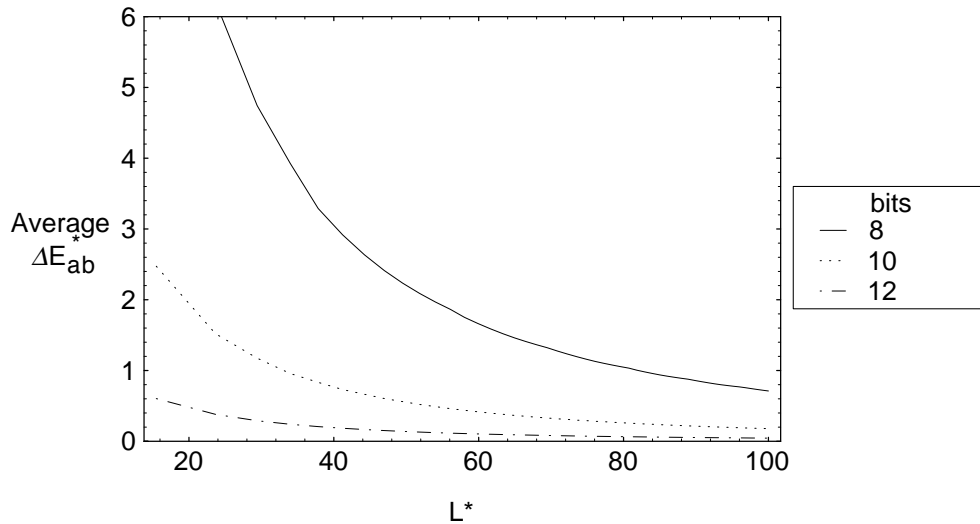


Fig. 7-1: Average quantization interval color-difference,  $\Delta E_{ab}^*$ , that results from the uniform quantization of tristimulus values, 8, 10 and 12-bit encoding for achromatic colors.

To minimize the visibility of quantization intervals it can be useful to quantize a set of color signals in an approximately perceptual color-space such as CIELAB, which implies a

nonuniform spacing of levels. This can be accomplished by preceding the uniform quantizing step by a continuous transformation, e.g., via a nonlinear analog amplifier. Alternatively, one can first quantize the continuous input signal using a  $m$  levels and then perform a discrete look-up table (LUT) transformation from  $m$  to  $n$  levels, as shown in Fig. 7-2. The output quantization intervals can be interpreted in terms of corresponding input signals by projecting each output level back to the continuous input. The effective quantization intervals take the form of the discrete derivative of the discrete transformation. If  $m \gg n$  then the resulting  $m$ -level quantization will be approximately equally spaced in the transformed signal-space.



Fig. 7-2: Nonuniform quantization scheme using a uniform quantizer and a discrete  $m$ -to- $n$  look-up table transformation.

Consider quantizing a signal,  $x$ , so that 256 levels are equally space as a power function

$$y = x^p,$$

where  $p$  is a constant. The average quantization interval for the achromatic,  $L^*$ , axis was calculated for several values of  $p$ ,  $\{1/3, 1/2.2, 1/1.8\}$ . The cube-root function corresponds to the nonlinear step in the  $XYZ \rightarrow$  CIELAB transformation, and the other two exponents are similar to those commonly used to compensate for CRT display characteristics, i.e.,  $\gamma = 1.8, 2.2$ . These results can then be compared with those shown previously for  $p = 1$ ,

as shown in Fig. 7-3, for 10-bit (1024 levels) quantization. The cube-root transformation is seen as equalizing the quantization interval in CIELAB, as might be expected, since the  $L^*$  value depends solely on the single tristimulus value,  $Y$ .

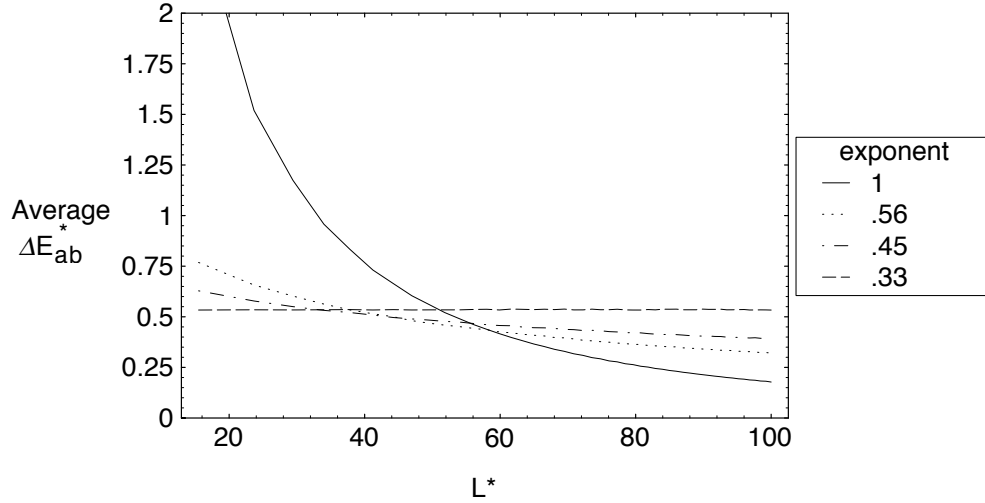


Fig. 7-3: Average quantization interval color-difference,  $\Delta E_{ab}^*$ , that results from the nonuniform, power-law quantization of tristimulus values and 10-bit encoding for achromatic colors.

The above analysis can be generalized for a camera with spectral sensitivities that are not color-matching functions. Returning to the example camera with spectral sensitivities given in Fig. 3-9. To calculate the colorimetric coordinates of image signals, they are subjected to the matrix transformation,

$$\mathbf{t} = \begin{bmatrix} 0.321 & 0.666 & 0.425 \\ 0.106 & 1.140 & 0.125 \\ -0.039 & -0.076 & 4.399 \end{bmatrix} \begin{bmatrix} R \\ G \\ B \end{bmatrix}$$

where  $\mathbf{t} = [X, Y, Z]^T$ . The previous calculations were repeated where the signal

quantization takes place prior to applying the matrix. The results, given in Fig. 7-4, show similar characteristics to those of Fig. 7-3.

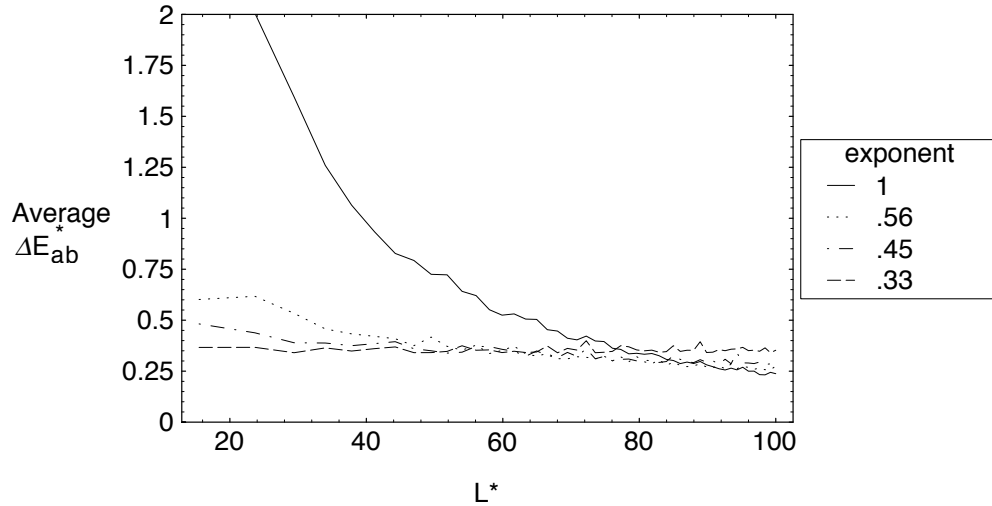


Fig. 7-4: Average quantization interval color-difference,  $\Delta E_{ab}^*$ , for the example camera when the signals are quantized according to a power-law using 10-bit encoding. The transformation requires the matrix operation, and the results are for the achromatic colors.

## 2. Multispectral Camera

The influence of camera signal quantization on system performance for a multispectral camera can be addressed in the same way as for three-channel image capture. Now, however, the set of quantization intervals about a given color is much larger. For the seven-filter camera,  $3^7 - 1 = 2186$  intervals need to be investigated. This was done in a computed experiment as outlined in Fig. 7-5. The camera signals for each of the twenty-four ColorChecker samples was calculated assuming the copy stand source, whose spectral power distribution is shown in Fig. 2-7, and the camera-filter sensitivities of Fig. 2-2. These signals were then quantized, either uniformly ( $p = 1$ ) or as a cube-root function ( $p = 1/3$ ). The remaining signal path included a modified PCA spectral reconstruction and

transformation to CIELAB, for illuminant  $D_{65}$  and  $10^\circ$  observer. The computed average color-difference due to the signal quantization are given in Table 7-1. By introducing the cube-root transformation, the average and median  $\Delta E_{ab}^*$  was reduced by about 0.11. This had less effect when ten or twelve-bit encoding was used. As might be expected, increasing the bits/signal used (thereby increasing the number of levels by a factor 2 per bit) reduced the CIELAB quantization intervals by about the same factor.

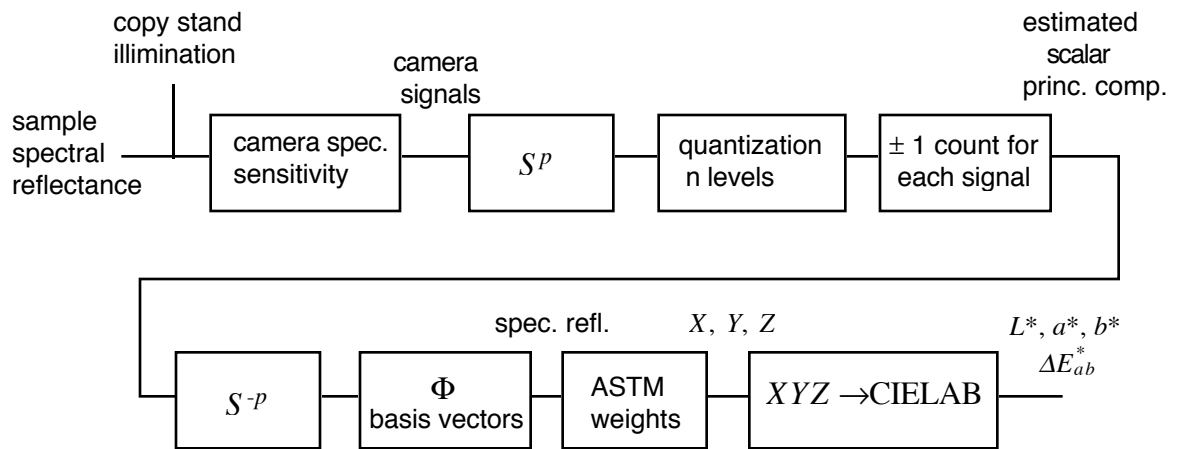


Fig. 7-5: Analysis of signal quantization for the multispectral camera and spectral reconstruction via the modified PCA method.

Table 7-1: Quantization interval as CIELAB color-difference values, for several levels of signal encoding and signal selections. Calculation was based on simulation of multispectral capture of ColorChecker sample colors and modified PCA spectral reconstruction. See text and Appendix I for more details.

signals	bits/signal	exponent	mean	median	max.
7 (1 2 3 4 5 6 7)	8	1	1.08	1.03	2.38
	8	1/3	0.95	0.91	2.12
	10	1	0.27	0.26	0.59
	10	1/3	0.28	0.23	0.53
7 (1 2 3 5 6 7 8)*	10	1/3	0.28	0.27	0.63
5 (1 2 3 5 7)	10	1	0.29	0.29	0.54
5 (1 2 3 7 8)*	10	1	0.37	0.35	0.67
	12	1	0.09	0.09	0.17

\* These were the 5 and 7-signal sets which minimized the average color-error as computed from the average experimental camera signals (see Table 5-2).

### B. Imager Noise

The multivariate error propagation analysis developed in Chapter III provides a way of estimating the first two statistical moments of the stochastic error that is introduced into the image signals at any subsequent point in the signal path. The analysis is applied here to help set imager noise limits, based on the required system precision. The computed example of section III-5 was presented in detail, but this was for a single (mean) color-sample and assumed no specific physical source of the stochastic error. A model for CCD imager noise is available, however, as also described in section III-B. Moreover, imager noise characteristics that were observed followed the form of this model as summarized in Chapter III, when account is taken of the signal quantization. The imager noise model will now be applied to the multispectral camera and signal processing path. Consider an electronic detector whose noise characteristics are governed by dark signal and shot-noise

components. A common noise figure for such detectors is the ratio of maximum signal to rms dark noise, the so-called dynamic range. Note that this is a form of maximum signal-to-noise ratio,  $\frac{\mu}{\sigma_{dark}}$ , where  $\mu$  is the (mean) signal. As an example, let the dynamic range be equal to 1200, and the maximum charge be 60,000 electrons. In addition, it is assumed that the imager noise fluctuations between signals are independent. This detector is used in a multispectral camera with the illumination and spectral sensitivities observed for the experimental camera described in Chapter IV. The rms noise can be expressed as a function of the signal level for each signal,

$$\sigma^2 = \sigma_{dark}^2 + k \mu \quad (7-3)$$

where  $\sigma_{dark} = 1/1200$  and  $k = 1/\sqrt{60,000}$ .

It is possible to investigate the effect of this imager noise on the resultant estimated spectral reflectance and derived colorimetric coordinates, by identifying the signal path. The case to be addressed here is that identified as the set of five signals that minimized the average CIELAB color-error computed from the experimental signals, the set {1, 2, 3, 7, 8}. The camera signal covariance matrix is has (5x5) diagonal form, with the diagonal elements given by Eq. (7-3). Following the modified PCA spectral reconstruction method described in Chapter II, the scalar principal components are calculated by

$$\alpha = \begin{bmatrix} -0.76 & -0.63 & -0.89 & -1.41 & -1.80 & -0.65 & -1.56 & -1.74 \\ 1.29 & 2.12 & -1.00 & -1.01 & 1.66 & -1.49 & 1.75 & -0.66 \\ -0.06 & 3.18 & 2.13 & -4.75 & 3.04 & -3.50 & 1.22 & -0.27 \\ -0.31 & -0.55 & 0.56 & -0.10 & 0.001 & 0.024 & 1.03 & -1.23 \\ 0.87 & 0.24 & -0.83 & 0.31 & -0.349 & 0.43 & 0.26 & -0.63 \end{bmatrix} \begin{bmatrix} s_1 \\ s_2 \\ s_3 \\ s_7 \\ s_8 \end{bmatrix}, \quad (7-4)$$

where the matrix transformation is found as a least-square fit between the between camera signals and principal components computed via Eq. (2-8).

The spectral reconstruction is computed as

$$\mathbf{r} = \Phi \mathbf{A} \mathbf{t},$$

where  $\mathbf{r}$  is the 31-element spectral reflectance column vector (400-700 nm in 10nm increments) and  $\Phi$  is the matrix of basis vectors. The corresponding covariance matrix for the estimated spectral reflectance is given by

$$\Sigma_{\mathbf{r}} = \Phi \mathbf{A} \Sigma_{\mathbf{t}} \mathbf{A}^T \Phi^T$$

where  $\Sigma_{\mathbf{t}}$  is the covariance matrix for the five camera signals. The multispectral capture and reconstruction of the ColorChecker color samples were simulated in this way. Figure 7-6 shows the results of spectral reconstruction and noise propagation for the cyan color sample. The rms noise vector is the square-root of the diagonal elements of  $\Sigma_{\mathbf{r}}$ .

If the spectral reflectance image information is processed to yield the corresponding CIELAB coordinates, the noise statistics can also be computed. For the cyan sample of Fig. 7-6, the corresponding mean and rms tristimulus values,  $X$ ,  $Y$ ,  $Z$ , are

$$\begin{aligned} \mu_{\mathbf{t}} &= [0.15, 0.21, 0.39] \\ \sigma_{\mathbf{t}} &= [0.0020 \quad 0.0015 \quad 0.0021]. \end{aligned}$$

Transformation to CIELAB coordinates, for CIE illuminant  $D_{65}$  and  $10^\circ$  observer, results in

$$\begin{bmatrix} L_{ab}^* & a^* & b^* \end{bmatrix} = \begin{bmatrix} 53.35 & -30.50 & -22.98 \end{bmatrix}$$

$$\begin{bmatrix} \sigma_{L^*} & \sigma_{a^*} & \sigma_{b^*} \end{bmatrix} = \begin{bmatrix} 0.16 & 1.08 & 0.38 \end{bmatrix}$$

$$E[\Delta E_{ab}^*] = 0.96$$

where the statistics are on a per pixel basis. The resulting statistics for all color samples in the set are given for this case of detector noise and signal processing in Appendix L. Table 7-2 summarizes the resulting CIELAB stochastic errors for several levels of detector noise.

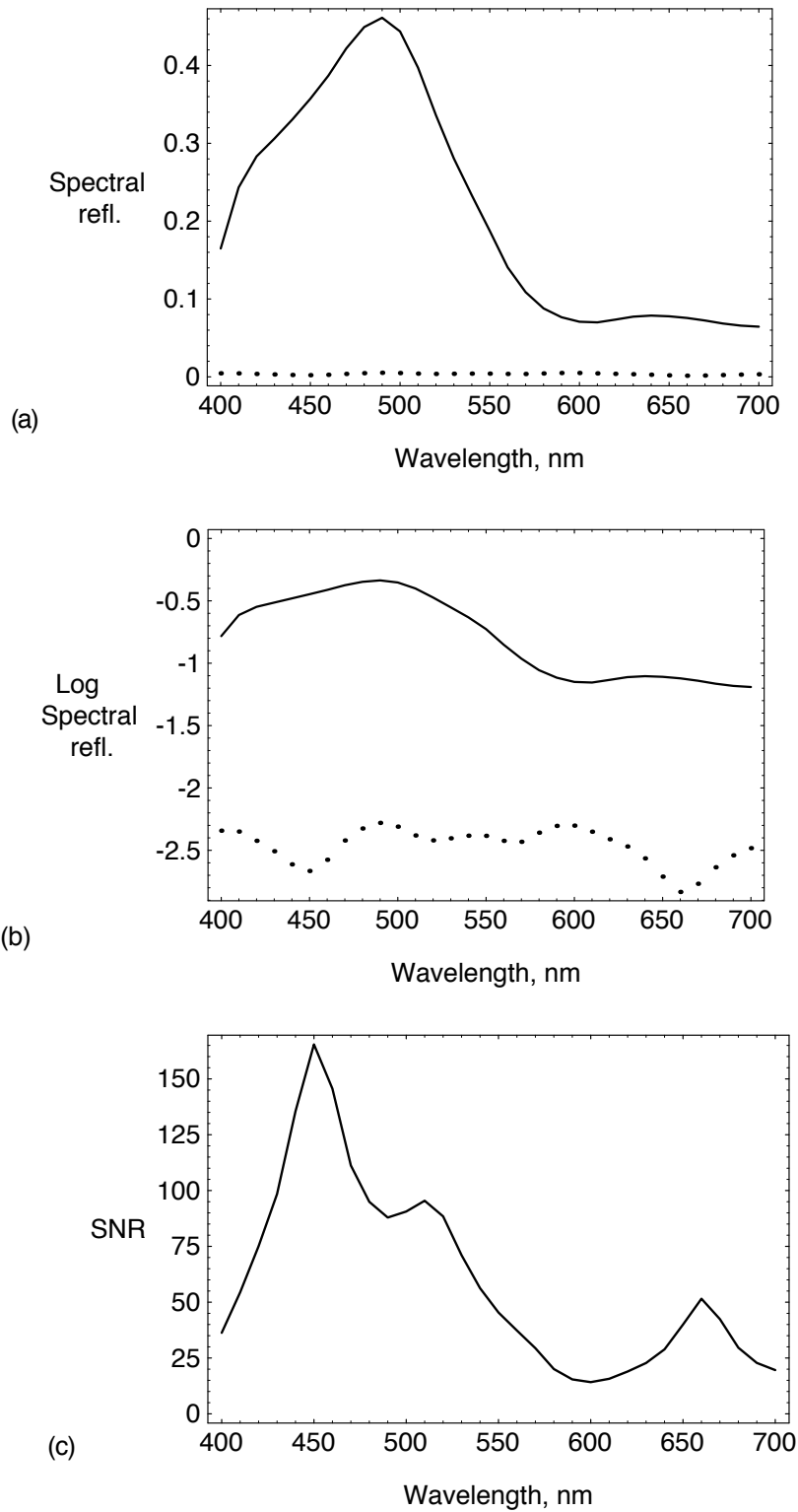


Fig. 7-6: Example of spectral reconstruction of the ColorChecker Cyan color.(a) and (b) show signal (solid) and rms noise (symbol). (c) shows the signal-to-noise ratio.

Table: 7-2: Average of calculated stochastic error statistics for ColorChecker samples, due to detector noise (dark- and shot-noise model). The imager dynamic range is (max. signal/ $\sigma_{\text{dark}}$ ) and the maximum signal is in electrons. The CIELAB transformation, following spectral reconstruction, is for CIE illuminant D<sub>65</sub>, and 10° observer. The last column is the mean color-difference.

camera signals	dynamic range	max. signal	average over colors			
			$\sigma_{L^*}$	$\sigma_{a^*}$	$\sigma_{b^*}$	$E[\Delta E_{ab}^*]$
7 (1 2 3 5 6 7 8)	1200	60,000	0.15	0.66	0.56	0.89
6 (1 2 3 5 7 8)	1200	60,000	0.22	1.35	0.55	1.27
5 (1 2 3 7 8)	1200	60,000	0.18	0.91	0.46	0.90
4 (1 2 3 5)	1200	60,000	0.18	0.54	0.47	0.74
5	600	60,000	0.23	0.17	0.60	1.17
	1200	100,000	0.15	0.75	0.38	0.75
	1200	150,000	0.13	0.66	0.34	0.67
	1800	150,000	0.12	0.58	0.29	0.58
7	1200	100,000	0.13	0.55	0.47	0.77
	1200	150,000	0.11	0.48	0.41	0.71
	1800	150,000	0.10	0.42	0.36	0.65

It is shown that as the detector noise levels increase, so do the CIEAB errors, as expected. An interesting observation is the fact that changing the number of camera signals used in the spectral reconstruction does not necessary increase or decrease the resultant image CIELAB noise significantly. This is due to the changing camera matrix,  $\mathbf{A}$ , that changes as the signals on which the spectral reconstruction is based are varied. To understand this consider the seven-signal reconstruction using signals (1, 2, 3, 5, 6, 7, 8). The  $\mathbf{A}$  matrix is

$$\mathbf{A}_7 = \begin{bmatrix} -0.868 & -0.456 & -1.93 & 1.26 & -3.13 & 1.62 & -1.98 \\ -0.810 & -1.17 & -1.63 & 1.35 & -0.121 & 0.315 & 1.53 \\ -1.27 & -0.434 & 1.23 & 2.44 & -1.9 & 1.34 & -1.51 \\ -0.565 & -0.54 & 2.59 & -2.76 & 0.645 & -1.74 & 2.21 \\ 1.98 & -1.89 & -0.872 & 3.19 & -2.37 & -1.05 & 1.13 \\ -1.16 & 1.28 & -0.316 & -1.39 & 4.12 & -4.88 & 2.22 \\ 1.91 & -2.87 & 3.39 & -6.56 & 7.58 & -3.9 & 0.546 \\ -0.0699 & 0.420 & -1.40 & 4.37 & -6.59 & 4.01 & -0.721 \end{bmatrix}.$$

The equivalent matrix that is required for a 6-signal spectral reconstruction is

$$\mathbf{A}_6 = \begin{bmatrix} -1.02 & -0.43 & -2.6 & -2.71 & -1.52 & 2.79 \\ -0.824 & -1.43 & -2.86 & -1.79 & 1.22 & 5.14 \\ -1.38 & -0.745 & -0.676 & -3.73 & -1.64 & 8.06 \\ -0.432 & -0.227 & 4.59 & 2.25 & 2.22 & -8.55 \\ 2.16 & -2.86 & -4.33 & -8.86 & -0.621 & 14.7 \\ -0.639 & 0.628 & -0.668 & -0.911 & -0.0353 & 1.57 \\ 2.23 & -2.1 & 8.4 & 12. & 0.719 & -21.2 \\ -0.412 & 0.173 & -4.1 & -7.22 & -0.0289 & 11.6 \end{bmatrix}.$$

While these two signal processing paths gave very similar spectral reconstructions and colorimetric accuracy, presence of large, particularly off-diagonal terms such as 12.0 (7, 4) and -21.2 (7, 6) results an increase in the resultant error in the final signal. In this case the mean color-difference increased by about 40%.

### C. Application to Metamer Characterization

As a final application of the previously developed modeling of both signal processing and noise propagation, consider the imaging of metameric samples. These are color samples that, although not identical in their spectral reflectance factor, appear\* to have the

---

\* are colorimetrically identical, having the same tristimulus values, X, Y, Z.

same color under a given illuminant. A three-channel colorimetric camera or colorimeter would see the samples as having the same color, if imaged under the specific illuminant. A multispectral camera, however, would be intended to identify spectral mismatches. The objective here is to investigate the extent to which the multispectral camera might be expected to detect small color-differences, given the limitations of spectral reconstruction error and image noise.

To this end, eleven of the color samples from the Munsell 37 set were chosen as references. A tristimulus matching algorithm based on Kubelka-Munk turbid media theory (Berns *et al.* 1988) was then used to design a set of ten metamers for each of the reference samples. The metamers were designed as mixtures of colorants from a data-base of DuPont acrylic-enamel paints, and characterized by a spectral reflectance-factor vector. Each set of metamers matched the corresponding reference sample tristimulus values under illuminant  $D_{65}$  and the  $2^\circ$  observer. Fig. 7-7 shows the reflectance factors for an example reference (5BG3/6) and set of computed metamers.

Since the sets of metamers are not spectral matches to the reference samples, they cannot be expected to match under another illuminant or for another observer. Table 7-3 lists the average CIELAB color difference between reference and metamer that would be observed under illuminant A for the  $2^\circ$  observer. The fifth column is based on an average of ten metamers.

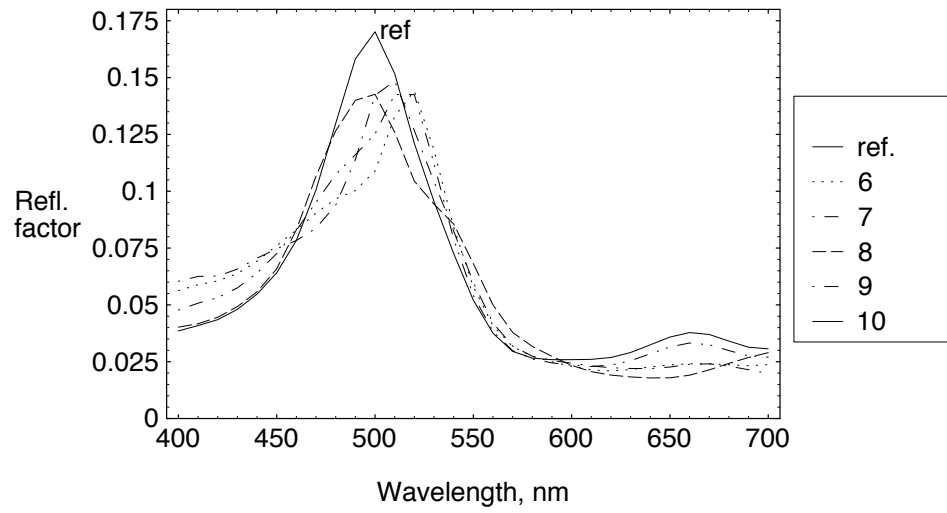
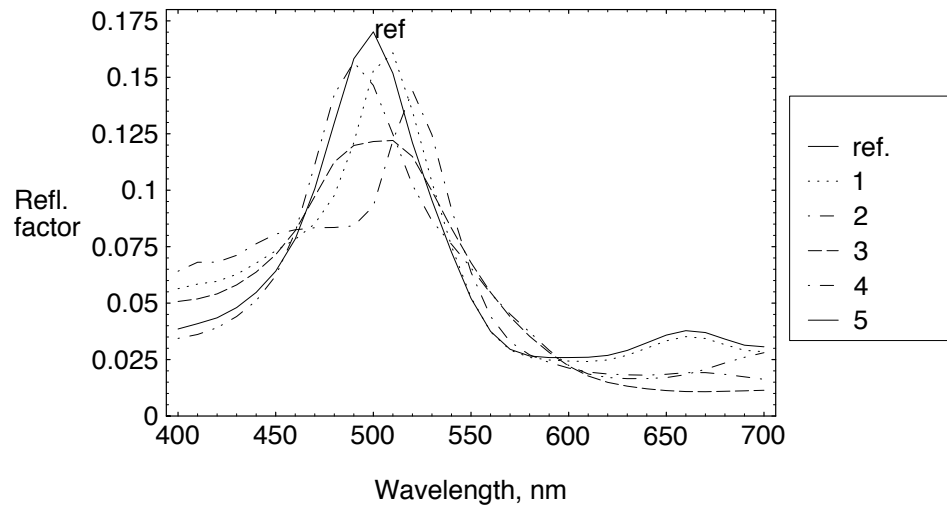


Fig. 7-7: Reflectance factors for one reference (5BG3/6) and the set of computed metamers.

Table 7-3: CIELAB coordinates for the reference samples, and average color difference between each and its set of metamers under illuminant A, and the 2° observer.

Sample	$L^*$	$a^*$	$b^*$	$\overline{\Delta E_{ab}^*}$
N1.5	14.68	-0.02	-0.20	3.19
N3.5	35.74	-0.03	0.32	4.75
N4.5	46.41	-0.13	0.31	5.55
N5.5	57.03	-0.17	0.31	4.76
N7.0	72.54	-0.36	0.29	3.42
N8.5	86.96	-0.14	0.42	1.21
5G3/6	28.81	-29.11	2.89	3.25
5BG3/6	27.33	-30.05	-13.63	2.55
5B3/6	27.25	27.01	-28.95	3.42
5RP5/12	57.26	52.29	5.88	4.21
5YR3/6	53.45	20.69	35.77	5.53

The imaging and capture of the sets of metamers was modeled in two computed experiments. In each case model camera signals were calculated using the analysis used in Chapter 2, and device noise model of Chapter 4. A signal processing path was then chosen for spectral reconstruction and transformation to CIELAB coordinates. The statistical moments of both the signal and noise were propagated through this path. A statistical test was then applied to the resulting CIELAB coordinates to determine whether the derived metamer pixel coordinates were significantly different from those for the reference sample.

The first experiment was aimed at assessing to what extent the camera could differentiate between the metamers and the corresponding reference samples, if all were captured under the illuminant ( $D_{65}$ ) under which they were visually identical. If perfect spectral reconstruction were achieved and no detector noise introduced, all metamers would clearly be seen as different from their corresponding reference samples, when expressed as

CIELAB coordinates for a different illuminant. Errors in the mean signals, representing bias, and stochastic variation combine, however, to make some small color differences undetectable. In the same way, some detected differences that are introduced due to the above system limitations should be ignored.

Since the signal and noise propagation techniques developed for the system result in both mean vector and covariance matrix, the evaluation of the derived output values can be cast as a multivariate statistical test for a difference in the mean CIELAB coordinates. This test, based on a multivariate analysis of variance, (MANOVA), (Johnson and Wichern 1992). Statistical tests of this nature are usually applied using *sample* statistics, i.e, the sample mean and covariance. Under the current analysis, however, the *population* statistics are calculated via the signal and noise propagation analysis. One interpretation of this would be that no statistical test is necessary, since the mean vectors are known. In this case any difference, no matter how small, should be taken as real (significant). The approach taken here was to apply the test to statistics based on a small image area, e.g., a ten-pixel neighborhood. The calculated CIELAB moments for each reference and metamer pair were taken as those observed in a small area of the image corresponding to an object in the scene. The modeled moments were taken as these estimates of the mean and covariance, allowing the test to be applied.

The first experiment was designed to evaluate the extent to which the model multispectral camera could detect color differences between metamers. For each of the metamers and reference samples the eight camera signals were computed for an illuminant, D<sub>65</sub>, under which they had identical tristimulus values. The modified PCA method was then used to estimate the spectral reflectance factor for each sample. The CIELAB coordinates were then computed for illuminant A and the 2° observer for each reference and

metamer. In addition, the detector image noise was modelled and propagated from camera signal to CIELAB. The results of applying the MANOVA test for significance in the mean metamer coordinates from those for the corresponding reference are given in Table 7-4. The test was based on sampling a ten-pixel neighborhood and a probability level of 0.99. The fourth column gives the percentage of metamers for which the null hypothesis, that there was no difference, was rejected. Since, under illuminant A the metamers have different coordinates than the corresponding reference sample, a high rate of rejection indicates that the multispectral camera could correctly identify these differences. From these results it can be concluded that more than five camera signals are needed to reliably detect color-differences of this type. In addition, for the noise levels included, a dynamic range of 1200, and shot-noise equivalent to a maximum signal of 100,000 electrons are required.

Table 7-4: Results of the multivariate test (0.99 level) for significance difference between the mean reference and corresponding metamer CIELAB coordinates for illuminant D<sub>65</sub>, based on the camera model in experiment 1.

camera signals	dynamic range	max. signal	% rejected
7 (1 2 3 5 6 7 8)	600	60,000	78.2
	1200	100,000	96.4
	1800	150,000	99.1
5 (1 2 3 7 8)	600	60,000	52.7
	1200	100,000	62.7
	1800	150,000	74.6

The above results appear to indicate that a camera with these characteristics could be used to evaluate these small color-differences. It should be noted, however, that (mean)

estimation errors due only to the filter choice and basis vector reconstruction will tend to increase the percentage of samples for which the null hypothesis is rejected. The second computed experiment was aimed at identifying whether samples would provide color matches. For each of the metamers and reference spectral reflectance factors, the camera signals were computed for illuminant A. The same signal processing path was used, except that CIELAB coordinates were computed for illuminant D<sub>65</sub>, under which the metamers and corresponding reference sample would be expected to have the same coordinates. The results of the MANOVA tests for this experiment are shown in Table 7-5. In contrast to the first experiment, a low rate of rejection would indicate positive outcome. From the relative high rejection ratio, except for one case, it can be concluded that this is a challenging task for this type of camera, but that more than five camera signals are needed. These statistical tests were performed in the same way for a signal based on a ten-pixel image area.

Table 7-5: Results of the multivariate test (0.99 level) for significance difference between the mean reference and corresponding metamer CIELAB coordinates for illuminant A, based on the camera model in experiment 2.

camera signals	dynamic range	max. signal	% rejected
7 (1 2 3 5 6 7 8)	600	60,000	4.5
	1200	100,000	1.82
	1800	150,000	10.9
5 (1 2 3 7 8)	600	60,000	30.0
	1200	100,000	49.1
	1800	150,000	62.7

## VIII. DISCUSSION: SUMMARY CONCLUSIONS AND RECOMMENDATIONS FOR FURTHER STUDY

A model multispectral camera and matrix-vector description of image capture have been described. These were then used to develop several approaches to the processing of the camera signals for spectral reconstruction. Interpolation methods were seen to yield poorer results than either the modified PCA method or the complex form of direct colorimetric transformation.

From the general analysis of error propagation in Chapter III, the first two statistical moments of stochastic errors can be analyzed in current color-spaces and through many color-image processing transformations. In addition to the magnitude of the signal variance, the propagation of the covariance between sets of signals has been described. By applying these error propagation techniques, variation due to measurement precision can be compared with the effects of experimental variables. This is based on the calculated or observed covariance matrices and underlying probability density functions. The inverse of many color-signal transformations of current interest can also be addressed in the same way. As demonstrated, a given tolerance of average  $\Delta E_{ab}^*$  or  $\Delta E_{94}^*$  can be related to an equivalent uncertainty in tristimulus values, other sets of detected signals, or image pixel values

Modeling of the noise characteristics of color-imaging devices can be combined with the above error-propagation analysis to predict signal uncertainty at any point in a system. Since physical devices include correlated noise sources, and the processing often combines signals, analysis of signal covariance is again included. By applying these methods, the statistical performance of multispectral and three-channel image acquisition systems can be predicted.

The experimental multispectral camera was assembled using a set of interference filters and a digital camera. This was used to capture sets of images and successfully estimate both spectral reflectance factor and colorimetric specification. The accuracy achieved in these experiments was within an average error of  $\Delta E_{ab}^* \leq 2$  (maximum  $< 3.5$ ) for several sets of basis vectors for the ColorChecker test target. This required the use of five or more camera signals. These results are similar to those achieved in previous studies (Saunders *et al.* 1990) and are within reach of the required color-accuracy identified by several workers (Stokes *et al.* 1992, Jung 1993). While model (ideal) camera calculations show increasing accuracy using up to eight basis vectors for the modified PCA method, processing of actual camera signals did not benefit from more than four bases.

The experimental camera was also analyzed from the standpoint of its image-noise characteristics. Despite somewhat coarse signal quantization at low signal values, a model of the intrinsic stochastic noise associated with the imager was developed. This was later used to model the propagation of this signal uncertainty through the signal path. It was concluded that the resultant CIELAB fluctuations were not a strong function of the number of camera signals used, for the case of uncorrelated errors. An effective maximum shot-noise equivalent to 60,000-100,000 detected photons would limit the mean error  $\Delta E_{ab}^* \leq 1$ .

A direct comparison of the second-order statistics of camera image noise was made with those computed using the multivariate error-propagation analysis. The latter was shown to accurately predict the results of actual signal processing.

Signal quantization was also addressed in terms of the error introduced into the spectral reconstruction and subsequent colorimetric transformation. It was concluded that for an average CIELAB error  $\Delta E_{ab}^* \leq 1$ , 10-bit quantization was sufficient, but 8-bit encoding leads to average errors of about 1 and maximum value of 2. Nonlinear quantization in the form of

a power-law showed minor improvements.

The use of an electronic camera designed for general digital photography and photojournalism, and the set of interference filters indicated how sequential-frame multispectral images can be acquired. The system was far from rugged, however, since each filter was manually placed in front of the camera lens. It is natural to consider using an automated filter wheel to improve the efficiency of image capture and reduce the risk of filter damage. A potentially more flexible approach would be to employ a tunable liquid crystal filter (CRI 1992, Sharp and Johnson 1996a, 1996b). Recently developed devices have been reported with switching times of less than a millisecond. With this performance, the limiting factor for speed of image capture would be the access to memory used for image storage in the camera.

Further investigation of image noise in multispectral image acquisition could benefit from an extension of the methods applied here to functions of spatial frequency. The well-established techniques of noise-power spectrum estimation and modeling could then be used to express image noise in terms comparable to the required signal bandwidth. One can think of the rms noise value as a relative noise measure. When placed in the context of the signal bandwidth it becomes more meaningful. For example, an rms CIELAB error of 3 may be acceptable for an application aimed at identifying a scene illuminant, when it can be done from object(s) sampled by fifty or more pixels. One way to compare signal and noise components is to express the noise as a variance (rms) per unit area of the image when possible. This is consistent with a frequency-domain description provided by the noise-power spectrum when given as variance per  $\text{cy/mm}$ , as is often done.

This has long been understood by those addressing the fundamental limits to imaging efficiency where, e.g., input exposure is at a premium (Dainty and Shaw 1974). This leads

naturally to the development of signal-to-noise ratio requirements being expressed as an effective quantum-limited performance in noise-equivalent quantum (NEQ) exposure (Shaw 1963, 1975, Shaw and Burns 1984, Burns 1990).

While there is no single noise criterion for multispectral systems, it is possible to investigate the requirements of several color-imaging applications. The requirements for museum imaging, artwork printing, color-appearance modeling or trichromatic device characterization will likely differ in terms of system precision. Few will require cooled detectors and 14-bit signal encoding. A possible approach is to project the required output characteristics backwards to the sources of bias and stochastic error, as was illustrated for the colorimeter example in Chapter III.

It is also useful to consider how the multispectral image capture and processing might be incorporated into current and future standards for color image communication. The approach suggested by Keusen (1997) calls for storing multispectral images so that three of the image records correspond to signals required for the more common three-channel color imaging such as  $X$ ,  $Y$ ,  $Z$  or  $L^*$ ,  $a^*$ ,  $b^*$ , referenced to a standard illuminant. At each pixel these would be the scalar weights associated with orthogonal basis vectors for the three CIE color matching functions and illuminant, or simply a linear combination of the colorimetric coordinates. Other image records would allow spectral reconstruction based on higher-order basis vectors in the same way as demonstrated in this work. Related investigation of alternative basis vectors has recently been reported (Praefcke 1995)

For some procedures, implementing image processing algorithms that are compliant with established file formats and transforms requires approximations and therefore introduces error. Comparison of the magnitude of this error with that due to other sources is valuable, particularly when selecting which of several implementations to pursue. For example, the methods used here could be compared with a series of allowable image

transforms that make up the device profiles under the framework being developed by the International Color Consortium (ICC) (1996). The most recent revision (3.3) of the ICC Profile Format Specification accommodates up to 15-channel image information in the list of Color Space Signatures. The reference for the definition of color signal transformations, the Profile Connection Space (PCS), is  $X, Y, Z$  or  $L^*, a^*, b^*$ . The standard does provide, however, for DeviceLink profiles for transformations directly between devices. In this case the PCS can be taken from the full set of Color Space Signatures. In addition, the standard includes the use of various Named Color Profiles to denote variations for a single device. It may be possible to employ this framework to allow multiple image processing paths from a single stored multispectral image file for various appearance model parameters.

Since the allowed signal processing steps in the ICC profiles include one-dimensional look-up tables,  $(3 \times 3)$  matrices, and  $n$ -dimensional look-up tables, several steps used in the spectral reconstruction and colorimetric transformations appear to fall within the standard. Matrices larger than  $(3 \times 3)$ , however, are currently missing from the specification. A detailed investigation of ICC-compatible implementations and arithmetic precision, however, remains to be done, as does the cascading of several image transformations to and from color-exchange spaces.

---

**IX. REFERENCES**

- , Colorimetry, 2nd ed., CIE Publ. No. 15.2, Central Bureau of the CIE, Vienna, 1986.
- , ICC Profile Format Specification Version 3.3, Internat. Color Consortium, Nov. 1996.  
Available from internet web site <http://www.color.org>.
- , Industrial color-difference evaluation, Technical Report Number CIE 116-1995, CIE Central Bureau, Vienna, 1995.
- , Kodak Professional DCS 200 Digital Camera User's Manual, Eastman Kodak Company, Rochester, NY, 1994.
- , Munsell Book of Color, Munsell Color Company, Baltimore, Md., 1976.
- , Standard Test Method for Computing the Colors of Objects by Using the CIE System, E308 - 90, American National Standards Institute, NY, 1990.
- , Varispec Filters, Cambridge Research and Instrumentation, Inc., Cambridge Mass., 1992.
- Ahumada, A. J. , Putting the visual system noise back in the picture. *J. Opt. Soc. Am. A*, **4**, 2372-2378 (1987).
- Allen, E., Matrix algebra for colorimetrists, *Color Engineering*, **4**, 24-31 (1966).
- Allen, E., Colorant formation and shading, in Optical Radiation Measurements, Volume 2, Color Measurement, F. Grum and C. J. Bartleson, Eds., Academic Press, New York (1980).
- Barlow, H. B., What causes trichromacy? A theoretical analysis using comb-filtered spectra, *Vision Res.*, **22**, 635-643 (1982).
- Beiser, L., Laser beam and electron beam extremely wideband information storage and retrieval, *Photogr. Sc. and Eng.*, **10**, 222- (1966).
- Bendat, J. S., and A. G. Piersol, Random Data: Analysis and Measurement Procedures, Wiley-Interscience, New York, 1971, pp. 296.

- Benzschawel, T., M. H. Brill and T. E. Cohn, Analysis of human mechanisms using sinusoidal spectral power distributions, *J. Opt. Soc. Am. A*, **3**, 1713-1725 (1986).
- Berns, R. S., M. D. Fairchild and M. M. Bering, Quantification of illuminant metamerism for four colorant systems via metameric mismatch gamuts, *Color Res. Appl.* **13**, 346-357 (1988).
- Berns, R. S. and K. H. Petersen, Empirical modeling of systematic spectrophotometric errors, *Color Res. and Appl.*, **13**, 243-256 (1988).
- Berns, R. S., R. J. Motta, M. E. Gorzynski, CRT colorimetry, part I theory and practice, *Color Res. Appl.*, **18**, 229-314, (1993).
- Berns, R. S., Spectral modeling of a dye diffusion thermal transfer printer, *J. of Elect. Imaging*, **2**, 359-370 (1993).
- Berns, R.S. and L. Reniff, An abridged technique to diagnose spectrophotographic errors, *Color Res. and Appl.*, **22**, 51-60 (1997).
- Box, G. E. P., W. G. Hunter and J. S. Hunter, Statistics for Experimenters, John Wiley, New York, 1978, pp. 87-89.
- Buchsbaum, G., and S. D. Bedrosian, Number of simultaneous colors versus gray levels: a quantitative relationship, *Proc. IEEE*, **72**, 1419-1421, (1984).
- Buchsbaum, G. and A. Gottschalk, Chromaticity coordinates of frequency-limited functions, *J. Opt. Soc. Am.*, **1**, 885-887, (1984).
- Burns, P. D., Analysis of the signal and noise characteristics of laser printers, *J. Imaging Sc.*, **31**, 74-81 (1987a).
- Burns, P. D., Analysis of DQE and NEQ measurement errors for medical imaging systems, *Proc. SPIE*, **767**, 259-270 (1987b).
- Burns, P. D., Image Modulation and Noise Characteristics of Charge-Coupled Device Imagers, *Proc. SPIE*, **1071**, 144-152 (1989).
- Burns, P. D., Signal-to-Noise Ratio Analysis of Charge-Coupled Device Imagers, *Proc. SPIE*, **1242**, 187-194 (1990).

- 
- Burns, P. D., Multispectral image capture, presentation to Color Science faculty and students, Center for Imaging Science, RIT, 11 Feb. 1994.
- Burns, P. D. and R. S. Berns, Error Propagation Analysis in Color Measurement and Imaging, *Color Res. Appl.*, in press.(1997).
- Chang, Y, P. Liang and S. Hackwood, Unified study of color sampling, *Appl. Opt.*, **28**, 809-813, (1989).
- Chollet, F. and M. Sanchez, Effet de couleur-magnitude dans les observation détoiles á lastrolobe (Color-magnitude effect in star observations with astrolabes), *Astron. Astrophys.*, **234**, 576-582, (1990).(in French)
- Cohen, J., Dependency of the spectral reflectance curves of the Munsell color chips, *Psychonomic Sc.*, **1**, 369-370 (1964).
- Coleman, C. I., High DQE image detectors, *Photogr. Sc. and Eng.*, **21**, 49-59 (1977).
- Conte, S. D., and C. de Boor, Elementary Numerical Analysis 2nd Edition., McGraw-Hill Book Company, New York, 1972, pp. 273-240.
- Dainty, J. C. and R. Shaw, Image Science, Academic Press, London, 1974, pp. 152- 182.
- Dereniak, E. L., and D. G. Crowe, Optical Radiation Detectors, John Wiley and Sons, New York, 1984, Chapt. 9.
- Doener, E. C., Wiener spectrum analysis of photographic granularity, *J. Opt. Soc. Am.*, **52**: 774, (1962).
- Dougherty, E. R., Probability and Statistics for Engineering, Computer and Physical Sciences, Prentice Hall, Engelwood Cliffs, N.J., 1990, pp. 116.
- Engelhardt, K. and P. Seitz, Optimum color filters for CCD digital cameras, *Appl. Opt.*, **32**, 3015-3023 (1993).
- Erb, W. and M. Krystek, Truncation error in colorimetric computations, *Color Res. Appl.*, **6**, 17-22 (1983).
- Fairchild, M. D., and L. Reniff, Propagation of random errors in spectrophotometric colorimetry, *Color Res. Appl.*, **16**, 361-367 (1991).

- 
- Felgett, P. B., Concerning photographic grain, signal-to-noise ratio and information, *Phil. Trans. Roy. Soc.*, **A247**, 369 (1955).
- Gan, Q., K. Kotani and M. Miyahara, Quantizing accuracy for high quality color image processing, (from Internat. Workshop on Image Processing Theory), *J. on Comm.*, **45**, 69-71 (1994).
- Gaskill, J. D., Linear Systems, Fourier Transforms and Optics, John Wiley and Sons, New York, 1978, pp. 269-271.
- Gentile, R. S., J. P. Allebach and E. Walowitz, Quantization of color images based on uniform color spaces, *J. of Imaging Tech.*, **16**, 11-21 (1990).
- Grosjean, D., E. Grosjean and E. L. Williams, Fading of artists colorants by a mixture of photochemical oxidants, *Atmospheric Environment*, **27A**, 765-722 (1993).
- Gschwind, R., Restoration of faded colour photographs by digital image processing, *J. Photogr. Sc.*, **38**, 193-196 (1990).
- Hiroaki, I., W. Dai and Y. Higaki, A study on colorimetric errors caused by quantizing chromaticity information, *Proc. 9th Annual Instrumentation and Measurement Conf.*, **IMTC-92**, 374-378, 1992, ( also *IEEE Trans. Instrumentation and Measurement*, **41**, 845-849 (1992) ).
- Hirose, Y., Perceptual characteristics of image noise in color hardcopy images, *Proc. SPIE*, **1912**, 464-473 (1993).
- Holst, G. C., CCD Arrays, Cameras and Displays, JCD Publishing, Winter Park, Florida, 1996, pp. 113-117.
- Horn, B. K. P., Exact reproduction of colored images, *Computer Vision, Graphics, and Image Processing*, **26**, 135-167 (1984).
- Huck, F. O., C. L. Fales, N. Halyo and W. Sams, Image gathering and processing: Information and fidelity. *JOSA A*, **2**, 1644-1665 (1985).
- Hung, P., Color rendition using three-dimensional interpolation. *Proc. SPIE*, **1909**, 111-115 (1988).

- 
- Hung, P-C., Colorimetric calibration for scanners and media., *Proc. SPIE*, **1448**, 164-174 (1991).
- Hung, P-C., Colorimetric calibration in electronic imaging devices using look-up-table model and interpolations, *J. Electronic Imaging*, **2**, 53-61 (1993).
- Ikeda, H., A study on colorimetric errors caused by quantizing chromaticity information, *IEEE Trans. Instr. and Meas.*, **41**, 845-849 (1992).
- Jaaskelainen, T., J. Parkkinen and S. Toyooka, Vector-subspace model for color representation. *J. Opt. Soc. Am. A*, **7**, 725-730 (1990).
- Jackson, J. E., A User's Guide to Principal Components, John Wiley and Sons, New York, 1991.
- Janesick, J. R., T. Elliott, S. Collins, M. M. Blouke, and J. Freeman, Scientific charge-coupled devices, *Opt. Eng.*, **26**, 692-714, (1987).
- Johnson, R. A., and D. W. Wichern, Applied Multivariate Statistical Analysis, Prentice-Hall, Engelwood Cliffs, NJ, pp 61-62, 1992.
- Juday, R. D., Colorimetric principles as applied to multichannel imagery, Report number TM-58215, NASA, Washington DC, 1979.
- Jung, N., Noise margins of colour image drum scanners, *J. Photogr. Sc.*, **41**: 98-99 (1993).
- Kang, H. R., Color scanner calibration, *J. Imag. Sc. and Tech.*, **36**, 162- (1992).
- Kasson, J. M., S. I. Nin, W. Plouffe and J. L. Hafner, Performing color space conversions with three-dimensional linear interpolation. *J. Electron. Imaging*, **4**, 226-250 (1995).
- Kawata, S., K. Sasaki and S. Minami, Component analysis of spatial and spectral patterns in multispectral images. I. Basis, *J. Opt. Soc. Am. A.*, **4**, 2101-2106, (1987).
- Keusen, Th., Multispectral color system with an encoding format compatible with the conventional tristimulus model, *J. Imaging Sc. and Tech.*, **40**: 510-515, (1996).

- Kollarits, R. V., and D. C. Gibbon, Improving the color fidelity of cameras for advanced television systems, *Proc. SPIE*, **1656**, 19-29 (1992).
- Lagutin, V. I., Estimating errors in determining color coordinates (in Russian), *Izmeritelnaya Tekhnika*, **2**, 27-29 (1987), translated in *Measurement Techniques*, **30**, 150-3 (1987), Plenum Publishing Corp..
- Linfoot, E. H., Equivalent quantum efficiency and information content of photographic images, *J. Photogr. Sc.*, **9**, 188 - (1961).
- MacAdam, D. L., Chromatic significance of spectrophotometric errors, *J. Opt. Soc. Am.*, **47**, 766 (1957).
- Maloney, L. T., Evaluation of linear models of surface spectral reflectance with small numbers of parameters, *J. Opt. Soc. Am. A*, **10**, 1673-1683 (1986).
- Marimont, D. and B. A. Wandell, Linear models of surface and illuminant spectra, *J. Opt. Soc. Am. A*, **9**, 1905-1913 (1992).
- Martinez, K., and A. Hamber, Towards a colorimetric digital image archive for the visual arts, *Proc. SPIE*, **1073**, 114-121 (1989).
- Martinez, K., J. Cupitt and D. Saunders, High resolution colorimetric imaging of paintings, *Proc. SPIE*, **1901**, 25-36 (1993).
- McCamy, C. S., H. Marcus and J. G. Davidson, A color-rendition chart, *J. Appl. Photogr. Eng.*, **2**, 95-99, (1976).
- McCurnin, T. W. L. C. Schooley and G. R. Sims, Charge-Coupled Device Signal Processing Models and Comparisons, *J. Electronic Imaging*, **2**, 100-107 (1993).
- Miller, M., Maya masterpiece revealed at Bonampak, *National Geographic*, Feb. 1995, pp 50-69 (1995).
- Nimeroff, I., Propagation of errors in spectrophotometric colorimetry, *J. Opt. Soc. Am.*, **43**, 531-533 (1953).
- Nimeroff, I., Propagation of errors in tristimulus colorimetry, *J. Opt. Soc. Am.*, **47**, 697-702 (1957).

- Nimeroff, I., Comparison of uncertainty ellipses calculated from two spectrophotometric colorimetry methods by an automatic-computer program, *J. Opt. Soc. Am.*, **56**, 230-237 (1966).
- Nimeroff, I, J. R. Rosenblatt and M. D. Dannemiller, Variability of spectral tristimulus values, *J. Opt. Soc. Am.*, **52**, 685-692 (1962), also published by the same title in *J. of Research of Nat. Bureau Standards*, **65A**, 475-483 (1961).
- Ohta, O., Maximum errors in estimating spectral-reflectance curves from multispectral image data, *J. Opt. Am.*, **71**, 910-913, (1981).
- Oppenheim, A. V., and R. W. Schaffer, Digital Signal Processing, Prentise Hall, Englewood Cliffs, New Jersey, 1975, pp. 409-413.
- Papoulis, A., *Probability, Random Variables and Stochastic Processes*, McGraw-Hill, New York, 1965, pp. 151-152, 126-133.
- Parkkinen, J. P. S., J. Hallikinen and T. Jaaskelainen, Characteristic spectra of Munsell colors, *J. Opt. Soc. Am. A*, **6**, 318-322 (1989).
- Pratt, W. K., Digital Image Processing, J. Wiley and Sons, New York, 1978, pp. 140-146.
- Praefcke, W. and Th. Keusen, Optimized basis functions for coding reflectance spectra minimizing the visual color difference, *Proc. of the third IS&T/SID Color Imaging Conference*, Scottsdale, Arizona, 1995, pp. 37-40.
- Press, W. H., B. P. Flannery, S. A. Teukolsky and W. T. Vetterling, Numerical Recipes in C, Cambridge Univ. Press, Cambridge Eng., 1988, pp. 94-98.
- Quindos, L. S., A. Bonet, N. Diaz-Caneja, P. L. Fernandez, I. Gutierrez, J. R. Solana, J. Sota and E. Villar, Study of the environmental variables affecting the natural preservation of the Altamira cave paintings located at Santillana del Mar, Spain, *Atmospheric Environment*, **21**, 551-560, (1987).
- Quiroga, J. A., J. Zoido, J. Alonso, and E. Bernabeu, Colorimetric matching by minimum-square-error fitting, *Appl. Opt.*, **33**, 6139-6141 (1994).

- 
- Reniff, L., Transferring the 45/0 spectral reflectance factor scale, *Color Res. Appl.*, **19**, 332-340, (1994).
- Réti, I., I. Giczi and K. Muray, Filter matching for imaging colorimetry, *Opt. Eng.*, **32**, 2578-2580 (1993).
- Robertson, A. R., Colorimetric significance of spectrophotometric errors, *J. Opt. Soc. Am.*, **57**, 691-698 (1967)
- Romero, J., L. Jiménez del Barco and E. Hita, Mathematical reconstruction of color-matching functions, *J. Opt. Soc. Am. A*, **9**, 25-29 (1992).
- Rose, A. , *Vision: Human and Electronic*, Plenum, New York, 1974.
- Rossman, K., Spatial fluctuations of x-ray quanta and the recording of radiographic mottle, *Am. J. Roent.*, **90**, 863 (1963).
- Saunders , D., The Detection and Measurement of Colour Changes in Paintings by Digital Image Processing, *Proc. SPIE*, 1075, 405-415 (1989).
- Saunders, D., and A. Hamber, From Pigments to Pixels: Measurement and Display of the Colour Gamut of Paintings, *Proc. SPIE*, 1250, 90-102 (1990).
- Schreiber, W. F., Fundamentals of Electronic Imaging Systems, 2nd Ed., Springer-Verlag, Berlin, 1990, pp. 97-8.
- Searle, R. R., Matrix Algebra Useful for Statistics, John Wiley, New York, 1982, pp. 338.
- Sezan, M. I., K-L. Yip and S. J. Daly, Uniform perceptual quantization: applications to digital radiography, *IEEE Trans. Systems, Man and Cybernetics*, **SMC-17**, 622-634 (1987).
- Shannon, C. E., and W. Weaver, *The Mathematical Theory of Communication*, Univ. of Illinois Press, Urbana Illinois, 1948.
- Sharp, G. D., and K. M. Johnson, A new RGB tunable filter Technology, *Proc. SPIE Electronic Imaging Conf.*, (1996a).

- 
- Sharp, G. D., and K. M. Johnson, High brightness saturated color shutter technology, *Proc. SID Annual Conference*, (1996b).
- Shaw, R., The equivalent quantum efficiency of the photographic process, *J. Photogr. Sc.*, **11**, 199-204 (1963).
- Shaw, R., Comparative signal-to-noise ratio analysis of particle development in electrophotography and silver halide photography, *J. Applied Photog. Eng.*, **1**, 1-4 (1975).
- Shaw, R., and P. D. Burns, Noise requirements for the recording medium of a laser printing device, *Proc. Non-Impact Printing Tech. Conf.*, SPSE, pp. 127-130, 1984.
- Shipley, T., and G. L. Walker, Chromatic significance of spectrophotometric errors, *J. Opt. Soc. Am.*, **46**, 1052-1060 (1956)
- Sluban, B. and J. H. Nobbs, The Colour Sensitivity of a Colour Matching Recipe, *Color Res. Appl.*, **20**, 226-234 (1995).
- Stearns, E. I., Influence of spectrophotometer slits on tristimulus calculations, *Color Res. Appl.*, **6**, 78-84 (1981).
- Stearns, E. I., A new look at calculation of tristimulus values, *Color Res. Appl.*, **6**, 203-206 (1981).
- Stearns, E. I., The determination of weights for use in calculating tristimulus values, *Color Res. Appl.*, **6**, 210-212 (1981).
- Stearns, E. I., and R. E. Stearns, An example of a method for correcting radiance data for bandpass error, *Color Res. Appl.*, **13**, 257-259 (1988).
- Stiles, W. S. Stiles, G. Wyszecki and N. Ohta, Counting metameric object-color stimuli using frequency-limited spectral reflectance functions, *J. Opt. Soc. Am.*, **67**, 779-784 (1977).
- Stokes M, Fairchild M D, Berns R S, Precision requirements for digital color reproduction *ACM Transactions and Graphics*, **11**: 406-422 (1992).

- 
- Suzuki, S., T. Kusunoki and M. Mori, Color characteristic design for color scanners, *Appl. Opt.*, **29**, 5187-5192 (1990).
- Taylor, B. N. and C. E. Kuyatt, Guidelines for evaluating and expressing the uncertainty of NIST measurement results, NIST Tech. Note 1297, US Dept. of Commerce, Washington, 1993, p. 8.
- Tominaga, S., Multichannel vision system for estimating surface and illumination functions, *J. Opt. Am. A.*, **13**, 2163-2173, (1996).
- Trussell, H. J., Applications of set theoretic methods to color systems, *Color Res. Appl.*, **16**, 31-41 (1991).
- Trussell, H. J., A review of sampling effects in the processing of color signals, *Proc. IS&T and SID 2nd Color Imaging Conference, Color Science, Systems and Applications*, pp 26-29 (1994).
- Vrhel, M. J., R. Gershon and L. S. Iwan, Measurement and analysis of object reflectance spectra, *Color Res. Appl.*, **19**, 4-9 (1994).
- Vrhel, M. J. and H. J. Trussell, Filter considerations in color correction, *IEEE Trans. Image Proc.*, **3**, 147-161, (1994).
- Wolter, K. M., Introduction to Variance Estimation, Springer-Verlag, New York, 1985, pp. 221-229.
- Wong, P. W., Quantization noise, fixed-point multiplicative roundoff noise, and dithering, *IEEE Trans. Acoustics Speech and Signal Proc.*, **38**, 286-300, (1990).
- Wyszecki, G., and W. S. Stiles, Color science concepts methods, quantitative data and formulae, 2nd ed, John Wiley and Sons, NY, 2nd ed., pp 117-126, 1982.
- Wyszecki, G., and W. S. Stiles, *Color Res. Appl.*, **7**, pp. 328-330, (1982).

## X. APPENDICES

**Appendix A:  $\Delta E_{ab}^*$  for PCA spectral reconstruction errors for Munsell 37 data set**

Table A-1: PCA reconstruction errors for the Munsell-37 set, where  $p$  is the number of components used. Columns 5-8 are  $\Delta E_{ab}^*$  values following reconstruction using 6 and 8 principle components based on the variance (cols. 5, 6), and second moment about the zero vector (cols. 7, 8). CIE illuminant A and the  $2^\circ$  was used for the calculation.

sample	CIELAB coordinates			$\Delta E_{ab}^*$			
	L*	a*	b*	Cov. about mean		Cov. about zero vector	
				p = 6	p = 8	p = 6	p = 8
N1.5	14.7	0.0	-0.2	0.7	0.6	0.6	0.1
N3.5	35.7	0.0	0.3	0.8	0.1	0.8	0.1
N4.5	46.4	-0.1	0.3	0.9	0.0	0.8	0.1
N5.5	57.0	-0.1	0.4	1.0	0.0	0.9	0.1
N7.0	72.5	-0.3	0.4	0.8	0.0	0.8	0.1
N8.5	87.0	-0.1	0.5	0.2	0.1	0.2	0.2
N9.5	96.4	-0.1	1.3	0.5	0.1	0.5	0.2
5G6/10	58.8	-46.9	8.0	1.5	0.1	1.5	0.2
5G8/6	78.8	-28.8	7.8	0.8	0.0	0.8	0.1
5G3/6	28.9	-26.6	4.5	0.6	0.3	0.6	0.0
5BG5/10	47.7	-49.8	-17.7	0.1	0.3	0.1	0.3
5BG8/4	80.6	-21.1	-5.7	0.1	0.1	0.1	0.1
5BG3/6	27.8	-29.5	-11.8	0.2	0.2	0.2	0.1
5B5/10	47.9	-43.4	-39.5	1.1	0.2	1.1	0.4
5B8/4	79.8	-17.3	-14.9	0.2	0.0	0.2	0.1
5B3/6	28.1	-28.2	-27.3	0.1	0.1	0.2	0.4
5PB5/12	48.7	-17.5	-49.0	1.2	0.4	1.2	0.5
5PB2/8	17.5	-14.8	-39.8	1.0	0.3	1.1	0.7
5PB8/6	81.9	-6.9	-17.3	0.8	0.1	0.8	0.1
5P5/10	53.8	20.3	-26.6	0.9	0.0	0.9	0.1
5P8/4	82.9	6.2	-9.4	0.1	0.1	0.1	0.2
5P2/8	19.3	21.0	-22.0	2.9	0.3	2.9	0.5
5RP5/12	57.3	46.7	4.9	1.3	0.2	1.3	0.3
5RP2/8	22.5	32.4	-3.8	2.7	0.3	2.8	0.3
5RP8/4	84.3	14.0	2.3	0.6	0.1	0.6	0.1
5R4/14	48.8	58.6	45.2	2.0	0.4	1.9	0.6
5R8/6	84.8	24.5	19.4	0.6	0.0	0.6	0.1
5R2/6	23.6	26.3	14.1	1.4	0.3	1.2	0.4
5YR6/14	67.6	39.3	89.0	8.3	0.1	8.4	0.4

(continued on next page)

---

5YR8/6	85.1	20.6	35.8	0.3	0.1	0.3	0.1
5YR3/6	33.1	20.6	35.6	0.4	0.7	0.6	0.2
5Y9/6	93.0	6.5	46.2	0.2	0.3	0.2	0.3
5Y4/6	42.3	7.1	44.9	1.1	0.6	1.2	0.1
5Y8/14	84.8	11.3	99.9	4.6	0.2	4.6	0.1
5GY7/12	70.7	-17.4	78.5	2.1	0.1	2.2	0.5
5GY8/4	82.0	-5.1	26.9	0.5	0.3	0.5	0.3
5GY3/6	30.3	-11.2	32.4	0.4	0.8	0.6	0.2
<hr/>							
mean				1.2	0.2	1.2	0.2
max.				8.3	0.8	8.4	0.7
RMS				1.5	0.2	1.5	0.2

---

## APPENDIX B: CIELAB Color-difference results for simulated Multispectral Camera Image Acquisition

Table B-1: Average CIELAB errors calculated from model Image Acquisition.

sample	PCA	MDST	Spline	simple	complex
N1.5	0.2	0.1	0.1	3.5	4.0
N3.5	0.3	0.2	0.1	0.7	0.4
N4.5	0.3	0.3	0.2	1.1	1.3
N5.5	0.4	0.3	0.2	1.4	1.6
N7.0	0.3	0.5	0.4	1.3	0.9
N8.5	0.1	0.9	0.8	1.5	0.9
N9.5	0.1	1.3	1.1	2.6	1.5
5G6/10	1.1	14.4	18.3	2.8	0.2
5G8/6	0.5	8.7	11.2	1.3	0.8
5G3/6	0.5	7.9	10.1	4.1	1.0
5BG5/10	0.1	13.4	15.6	4.7	0.4
5BG8/4	0.1	5.3	6.3	1.0	1.1
5BG3/6	0.3	7.3	8.5	4.0	1.2
5B5/10	1.1	8.0	7.8	4.5	1.0
5B8/4	0.1	3.8	3.9	0.6	0.6
5B3/6	0.3	5.1	4.8	3.8	0.5
5PB5/12	0.8	3.5	5.9	8.5	0.3
5PB2/8	1.1	4.0	6.2	10.6	0.7
5PB8/6	0.4	1.7	1.7	1.9	0.2
5P5/10	0.6	7.0	10.8	2.7	0.1
5P8/4	0.1	2.8	3.8	2.4	0.3
5P2/8	2.7	6.4	10.4	2.5	0.0
5RP5/12	0.6	14.0	16.5	1.6	0.1
5RP2/8	1.4	6.3	10.7	2.9	0.1
5RP8/4	0.3	4.6	5.0	1.2	0.6
5R4/14	0.9	15.4	17.7	3.2	0.1
5R8/6	0.4	8.0	7.7	1.2	0.5
5R2/6	1.2	8.2	8.7	4.6	0.4
5YR6/14	1.7	14.5	11.2	6.5	0.2
5YR8/6	0.6	6.0	4.8	1.5	1.2
5YR3/6	0.5	6.7	5.7	4.1	0.7

(continued)

---

5Y9/6	0.1	1.1	2.9	3.0	0.6
5Y4/6	0.2	1.8	0.8	0.9	0.3
5Y8/14	1.6	3.0	5.1	5.6	0.1
5GY7/12	1.5	7.4	14.0	3.4	0.0
5GY8/4	0.2	3.6	5.3	2.8	1.0
5GY3/6	0.7	3.4	5.9	1.6	0.4
<hr/>					
mean	0.6	5.6	6.8	3.0	0.7
rms	0.6	4.3	5.1	2.1	0.7
max.	2.7	15.4	18.3	10.6	4.0

---

### APPENDIX C: Moments of Functions of Random Variables

We are given functions of two random variables,  $f(x, y)$  and  $g(x, y)$ , where the corresponding means, variances, and covariance are  $\mu_x, \mu_y, \sigma_x^2, \sigma_y^2, \sigma_{xy}$ . In the following expressions, we only retain up to the second-order moments of  $x$  and  $y$ , however the approach is general and if necessary can be extended to higher-order terms in the series.

#### A. Mean

The expansion of  $f$  in a Taylor series about  $\mu_x$  and  $\mu_y$  (Ref. 31) is,

$$f(x,y) = f(\mu_x, \mu_y) + f'_x(x-\mu_x) + f'_y(y-\mu_y) + \frac{1}{2} [f''_{xx}(x-\mu_x)^2 + 2f''_{xy}(x-\mu_x)(y-\mu_y) + f''_{yy}(y-\mu_y)^2] + \dots \quad (C-1)$$

where

$$f'_x = \left. \frac{\partial f(x,y)}{\partial x} \right|_{\mu_x, \mu_y}, \quad f''_{xy} = \left. \frac{\partial^2 f(x,y)}{\partial x \partial y} \right|_{\mu_x, \mu_y}.$$

Taking expectations yields the mean value,

$$E[f(x,y)] = f(\mu_x, \mu_y) + \frac{1}{2} [f''_{xx}\sigma_x^2 + 2f''_{xy}\sigma_{xy} + f''_{yy}\sigma_y^2]. \quad (C-2)$$

The second term can be thought of as a bias.

#### B. Variance

The variance of  $f$  can be expressed as

$$\sigma_f^2 = E[f^2] - E[f]^2. \quad (C-3)$$

First we express  $f^2$  in terms of the series in Eq. (C-1),

$$f^2(x,y) = f^2(\mu_x, \mu_y) + f'_x(x-\mu_x)^2 + f'_y(y-\mu_y)^2 + 2 f(\mu_x, \mu_y) \left[ f'_x(x-\mu_x) + f'_y(y-\mu_y) + \frac{f''_{xx}(x-\mu_x)^2}{2} + f''_{xy}(x-\mu_x)(y-\mu_y) + \frac{f''_{yy}(y-\mu_y)^2}{2} \right] + 2 f'_x f'_y (x-\mu_x)(y-\mu_y) \dots$$

Taking expectations,

$$E[f^2(x,y)] = f^2(\mu_x, \mu_y) + f_x'^2 \sigma_x^2 + f_y'^2 \sigma_y^2 + f(\mu_x, \mu_y) [f''_{xx} \sigma_x^2 + f''_{yy} \sigma_y^2 + 2f''_{xy} \sigma_{xy}] + 2 f'_x f'_y \sigma_{xy} \quad (C-4)$$

Substituting Eqs. (C-2) and (C-4) into (C-3),

$$\sigma_f^2 = f_x'^2 \sigma_x^2 + f_y'^2 \sigma_y^2 + 2 f'_x f'_y \sigma_{xy} \quad (C-5)$$

### C. Covariance

The covariance of two functions of random variables,  $f(x, y)$  and  $g(x, y)$ , can be expressed as

$$\sigma_{fg} = E[fg] - E[f] E[g] \quad (C-6)$$

The two functions can be expanded as in Eq. (C-1), so

$$\begin{aligned} E[f] E[g] = f(\mu_x, \mu_y) g(\mu_x, \mu_y) + \frac{1}{2} f(\mu_x, \mu_y) [g''_{xx} \sigma_x^2 + 2g''_{xy} \sigma_{xy} + g''_{yy} \sigma_y^2] \\ + \frac{1}{2} g(\mu_x, \mu_y) [f''_{xx} \sigma_x^2 + 2f''_{xy} \sigma_{xy} + f''_{yy} \sigma_y^2]. \end{aligned} \quad (C-7)$$

Likewise, if we multiply the series expansions of  $f$  and  $g$  and take expectations

$$\begin{aligned} E[fg] = f(\mu_x, \mu_y) g(\mu_x, \mu_y) + \frac{1}{2} f(\mu_x, \mu_y) [g''_{xx} \sigma_x^2 + 2g''_{xy} \sigma_{xy} + g''_{yy} \sigma_y^2] \\ + \frac{1}{2} g(\mu_x, \mu_y) [f''_{xx} \sigma_x^2 + 2f''_{xy} \sigma_{xy} + f''_{yy} \sigma_y^2] \\ + f'_x g'_x \sigma_x^2 + (f'_x g'_y + f'_y g'_x) \sigma_{xy} + f'_y g'_y \sigma_y^2. \end{aligned} \quad (C-8)$$

Substituting Eqs. (C-7) and (C-8) into (C-6)

$$\sigma_{fg} = f'_x g'_x \sigma_x^2 + (f'_x g'_y + f'_y g'_x) \sigma_{xy} + f'_y g'_y \sigma_y^2. \quad (C-9)$$

If we examine the results in Eqs. (C-5) and (C-9) they are found consistent with the use of the matrix derivative operator

$$\mathbf{J} = \begin{bmatrix} \frac{\partial f}{\partial x} & \frac{\partial f}{\partial y} \\ \frac{\partial g}{\partial x} & \frac{\partial g}{\partial y} \end{bmatrix},$$

in the expression for the covariance matrix

$$\Sigma_{fg} = \mathbf{J} \Sigma_{xy} \mathbf{J}^T.$$

**APPENDIX D: Expected Value of  $\Delta E_{ab}^*$**

The expected value of  $\Delta E_{ab}^*$  is

$$\mathbb{E}[\Delta E_{ab}^*] = \mathbb{E}[\sqrt{\Delta L^{*2} + \Delta a^{*2} + \Delta b^{*2}}] \quad (\text{D-1})$$

where  $\Delta L^* = L^* - \mu_{L^*}$ , etc. Since the first and second partial derivative of the function  $\Delta E_{ab}^*(L^*, a^*, b^*)$  are undefined when evaluated at  $L^* = a^* = b^* = 0$ , a key requirement of error propagation based on Taylor series is violated. We can, however, approximate equation (D-1) in two steps and compare the result with that for a simple univariate case. We include up to the fourth moment.

First let

$$p = L^{*2} + a^{*2} + b^{*2}$$

where  $L^*$ ,  $a^*$ , and  $b^*$  now represent the zero-mean random variables,  $\Delta L^*$ ,  $\Delta a^*$ ,  $\Delta b^*$ , with some covariance matrix,  $\Sigma_{L^*a^*b^*}$ . The expected value of  $p$  is

$$\mathbb{E}[p] = \mu_p = \sigma_{L^*}^2 + \sigma_{a^*}^2 + \sigma_{b^*}^2 . \quad (\text{D-2})$$

The variance is

$$\sigma_p^2 = \mathbb{E}[p^2] - \mu_p^2 . \quad (\text{D-3})$$

If we expand  $p^2$  and take expectations,

$$\mathbb{E}[p^2] = \mathbb{E}[L^{*4}] + \mathbb{E}[a^{*4}] + \mathbb{E}[b^{*4}] + 2 [ \mathbb{E}[L^{*2}a^{*2}] + \mathbb{E}[L^{*2}b^{*2}] + \mathbb{E}[a^{*2}b^{*2}] ] . \quad (\text{D-4})$$

The terms of Eq. (D-4) cannot be related to  $\Sigma_{L^*a^*b^*}$  without an assumption about the

probability density function,  $P(L^*, a^*, b^*)$ . If we can approximate this by a joint normal distribution, then

$$\begin{aligned} E[L^{*4}] &= 3\sigma_{L^*}^4, \\ E[L^{*2}a^{*2}] &= \sigma_{L^*}^2 \sigma_{a^*}^2 + 2(\sigma_{L^*a^*})^2, \dots \end{aligned} \quad (D-5)$$

substituting Eqs. (D-5) and (D-4) into (D-3)

$$\sigma_p^2 = 2(\sigma_{L^*}^4 + \sigma_{a^*}^4 + \sigma_{b^*}^4) + 4[(\sigma_{L^*a^*})^2 + (\sigma_{L^*b^*})^2 + (\sigma_{a^*b^*})^2]. \quad (D-6)$$

Next we form the transformed variable,

$$q = \sqrt{p}.$$

Here we can expand the function in a series about the mean value of  $p$ , which is not zero. Following this approach the expected value is given by

$$E[q(p)] = E[\Delta E_{ab}^*] \approx \sqrt{\sigma_{L^*}^2 + \sigma_{a^*}^2 + \sigma_{b^*}^2} - \frac{\sigma_p^2}{8(\sigma_{L^*}^2 + \sigma_{a^*}^2 + \sigma_{b^*}^2)^{3/2}}, \quad (D-7)$$

where  $\sigma_p^2$  is given by Eq. (A6).

#### *Univariate normally-distributed errors*

As stated above, Eq.(D-1) does not have continuous partial first derivatives when  $\mu_{L^*} = \mu_{a^*} = \mu_{b^*} = 0$ . To compare our approximation, Eq. (D-7), with a known result, consider the case of a normally-distributed error in only one variable, i.e., where  $\sigma_{a^*}^2 = \sigma_{b^*}^2 = 0$ . Equation (D-7) becomes

$$E[\Delta E_{ab}^*] = 0.75 \sigma_{L^*}$$

For this case, however,  $\Delta E_{ab}^*$  is seen as merely the absolute value of  $\Delta L^*$ . The expected value of Eq. (D-1) is the mean absolute deviation given, for a normal random variable (Papoulis 1965), by  $0.80\sigma_{L^*}$ . So, for this univariate case, using Eq. (D-7) underestimates the mean of  $\Delta E_{ab}^*$ . A less accurate, but more conservative approximation is given by the first term of Eq. (D-7), resulting in  $E[\Delta E_{ab}^*] = \sigma_{L^*}$ .

### Appendix E: Model for CCD Imager Fixed-Pattern Noise

As discussed in Section 3 B, a simple model for CCD imager noise variance includes both dark and shot noise. If the quantum sensitivity or gain,  $\eta$ , can be described as a random variable about some mean value then the distribution of signal would become a compound Poisson process because the mean parameter is varying from pixel-to-pixel. To develop an expression for the detected signal variance in terms of fixed-pattern noise and shot noise, this process was simulated.

It was first assumed that the fixed-pattern noise variation could be sufficiently described as a normal random variable with mean and variance,  $\mu_\eta$  and  $\sigma_\eta^2$ , respectively. Two-hundred samples were drawn from a population. This was done ten times, varying the fixed-pattern noise parameter,  $f(\sigma_\eta/\mu_\eta)$ , from 2% to 14% in 2% increments. For each of these data sets, the following was done. Each of the 200 values was used as the mean value for a Poisson number generator, which gave 200 deviates. The resulting 200 sets of 200 values were treated as a single population for calculation of a sample mean,  $\mu_o$ , and variance,  $\sigma_o^2$ .

The mean value of the secondary values was found to be equal to the mean value of the primary samples. The variance was seen as well-fit by the equation

$$\sigma_o^2 = \mu_\eta + \sigma_\eta^2 \mu_\eta^2 (1 - f^2).$$

Figure E2 shows the result of the above simulation, for a mean input signal, varying from 100-1000 photons, for the extreme case of  $f = 25\%$ .

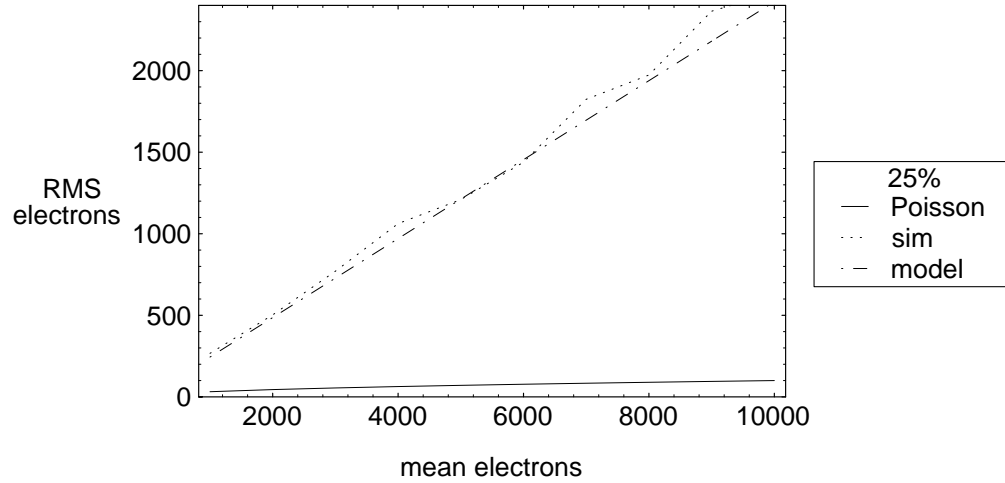


Fig. E-1: Results of the fixed-pattern noise simulation, as a function of mean signal, for  $f = 25\%$ . *Poisson* indicates the level expected for  $f = 0$ , *sim.* shows the simulation results and *model* shows the levels predicted by model of Eq. (3.33).

**APPENDIX F: Measurement of the Kodak Digital Camera Spectral Sensitivity**

Measurement of the spectral sensitivity of the digital camera was accomplished using a calibrated light source, part of the Model 740A-D Optical Radiation measurement system from Optronic Laboratories, Inc. This system includes an automated double monochromator with light source, capable of producing narrowband illumination over a range 280-900nm and triangular band widths of 1, 2.5, 5 and 10nm. A calibrated detector is used in conjunction with the automated wavelength derive, which can sweep the monochromator while measurements are made. The digital camera was to be used to capture several images of the source exit slit, at 10nm intervals. The signal values of the various images of the slit would be used to derive the measurement of camera spectral sensitivity.

A working distance of of 70 cm was chosen from the exit slit of the monochromator to the front surface of the Nikon camera lens. This gave an image size of the slit in the captured image of 25 x 45 pixels, which was centered. Next, the camera was replaced by the calibrated detector, and the source spectral irradiance was measured over the range [400-700 nm] in 10nm intervals. This is shown in Fig. C-1.

The camera was then remounted in the original position and several test exposures were made with several of the interference filters in place. Due to the wide range in both source irradiance and camera sensitivity over the wavelength range, it was necessary to significantly vary the camera exposure over the course of the experiment. It was also decided to fix the lens f/number at f/8, and set the camera to an ISO setting of 100, which would yield the lowest noise images. The camera was focused on the exit slit of the monochromator.

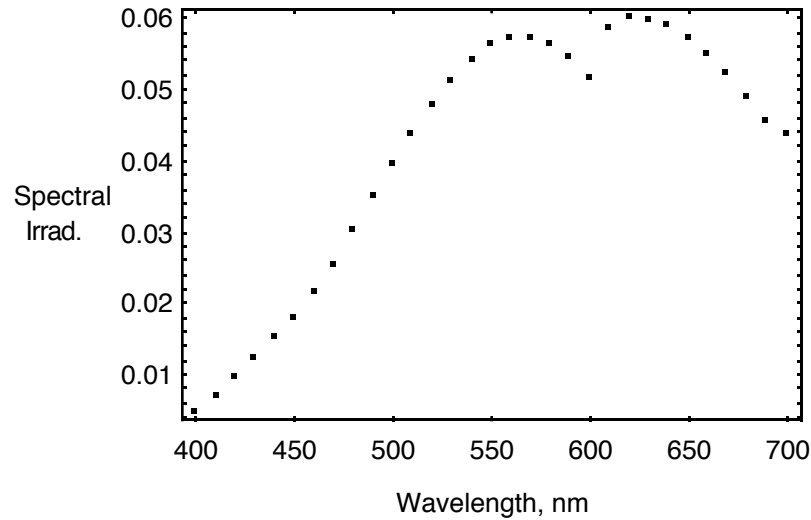


Fig. F-1: Measured spectral irradiance for the monochromator source used to measure the spectral sensitivity of the DCS 200m digital camera, in units of  $\text{j/m}^2/\text{nm} \times 10^3$ . Each symbol represents the source irradiance at the exit slit, of which a digital image was captured.

The problem with varying the camera exposure time setting is that there is no guarantee that the camera response in terms of digital value-exposure is a linear proportional scale. In addition, the stated exposure interval may not be accurate, for example changing from 1/250 sec. to 1/125 sec. may not double the exposure time interval. To solve both of these problems, the camera response to varying exposure needed to be established first. For a single wavelength, 610nm, images were captured under the above conditions, with the exposure time at each setting  $\{1/200, 1/1000, 1/500, 1/125, \dots 2 \text{ sec}\}$ . This was repeated at 450nm. The mean digital value for the slit image was then easily fit to the equations

$$\Delta v = 5644 (\Delta t)^{0.663} \quad (\text{C-1})$$

and the inverse

$$\Delta t = 0.06003 (\Delta v)^{1.508}, \quad (\text{C-2})$$

where  $\Delta v$  and  $\Delta t$  are the digital value and corresponding nominal exposure time interval. Note that the exponent in Eq.(C-2)<sup>†</sup> is consistent with a compensation for CRT characteristic response with  $\gamma = 1.5$ . This relationship was used to define an effective spectral sensitivity, separate from the nonlinear signal readout and signal processing, characterized by Eqs. (C-1) and (C-2) and shown in Fig. 4-6.

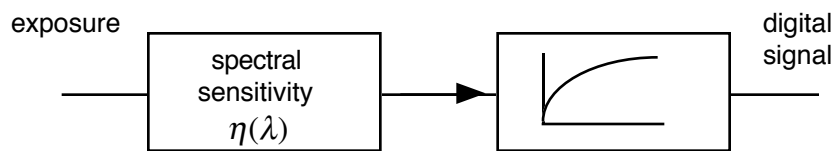


Fig. F-2: Two stage model of digital camera spectral sensitivity and signal processing

Using this model and Eq. (C-2), it was simple to relate signal values corresponding to varying exposure times. Each wavelength was addressed from 400nm increasing in order, with the exposure time chosen so as to maximize the digital signal level without causing signal clipping. The procedure used was:

1. For a given monochromator wavelength setting, the image was captured and the average digital signal value calculated.
2. This value was then multiplied by the nominal exposure time in seconds.
3. This value was then corrected for the nonlinear step using Eq. (4-2) and recorded as an effective response.
4. The ratio of this response divided by the previously measured source irradiance gives the effective spectral sensitivity.

The validity of this procedure was tested by comparing the results of each setting, at a

---

<sup>†</sup>and the inverse in Eq. (C-1).

wavelength when the exposure interval was changed. For example at 420nm a 1/30 sec exposure was set, for a signal of 217.6. Since the exposure is increasing as wavelength increases, exposing 430 at 1/30 sec would cause clipping. So prior to exposing 430 nm at 1/60, an additional exposure at 420nm was made at 1/60, so the above procedure could be validated. Since the two spectral sensitivity estimates at 420nm were almost identical, the procedure was taken as valid. This was done for each change of exposure setting.

It should be noted that this procedure yields an effective spectral sensitivity in terms  $\text{dv}/\text{j}/\text{m}^2/\text{nm}$ . It can only be compared with the expected detector absolute quantum efficiency in shape, or as a normalized curve. This is done in Fig. 4-6.

### Appendix G: Camera Signals for Macbeth ColorChecker Image Capture, and Photometric Correction Equations

Table: G-1: The average camera signal value for each of the color samples in the ColorChecker target. The eighth record was acquired using a Schott infra-red filter.

Sample	Filter record number							
	1	2	3	4	5	6	7	8
Dark skin	33.53	29.30	43.35	54.55	73.76	60.71	65.47	66.82
Light skin	68.75	69.40	93.70	109.10	144.60	114.30	105.20	132.60
Blue sky	88.90	74.35	71.58	61.92	66.94	45.88	38.88	70.88
Foliage	26.25	27.35	51.78	49.61	52.78	38.27	44.01	53.16
Blue Flower	104.90	88.25	79.70	73.87	91.37	73.10	80.84	92.19
Bluish green	91.98	99.27	128.40	104.90	102.60	66.80	61.84	115.30
Orange	30.10	29.78	70.72	119.60	162.70	127.60	114.10	139.60
Purplish blue	95.81	79.73	55.18	46.39	54.14	43.93	43.91	56.81
Moderate red	52.55	44.70	50.29	82.23	132.00	111.60	97.40	109.20
Purple	60.90	40.30	31.72	37.19	54.40	52.75	69.87	50.66
Yellow green	35.26	51.00	121.70	120.40	125.50	84.23	76.23	127.80
Orange yellow	32.21	39.65	101.10	141.60	178.70	133.80	119.90	159.10
Blue	79.29	70.08	39.75	30.01	38.88	32.86	35.08	41.15
Green	32.31	41.88	86.54	74.70	64.33	40.45	36.73	74.80
Red	26.52	23.10	29.87	56.87	113.20	113.10	106.50	95.32
Yellow	28.13	46.46	129.40	152.60	180.80	133.20	113.40	168.70
Magenta	90.73	66.58	55.28	73.69	127.60	121.90	118.70	113.00
Cyan	87.35	93.00	85.58	54.27	52.77	38.96	38.15	68.09
White	156.00	148.80	180.00	185.40	212.80	159.40	137.80	211.10
Neutral 8	122.20	113.30	135.30	138.50	158.40	115.70	97.06	156.90
Neutral 6.5	88.18	80.81	95.66	98.53	113.40	82.71	70.33	111.20
Neutral 5	59.50	54.39	64.51	66.40	78.15	56.91	49.78	75.38
Neutral 3.5	36.73	32.31	40.26	42.96	50.63	39.10	36.50	47.30
Black	19.04	16.83	19.91	22.81	27.47	21.42	20.95	23.03

Table: G-2: The average dark signal value for each of the color samples in the ColorChecker target.. Columns 4, 5 and 8 have the same values because the same camera settings were used.

Sample	Filter record number							
	1	2	3	4	5	6	7	8
Dark skin	3.56	3.54	2.71	4.17	4.17	4.17	1.58	4.17
Light skin	3.43	3.46	2.61	4.02	4.02	4.02	1.50	4.02
Blue sky	3.49	3.47	2.51	4.00	4.00	4.00	1.48	4.00
Foliage	3.51	3.49	2.49	3.96	3.96	3.96	1.48	3.96
Blue Flower	3.55	3.54	2.53	4.02	4.02	4.02	1.42	4.02
Bluish green	3.43	3.41	2.41	3.88	3.88	3.88	1.39	3.88
Orange	2.98	2.95	2.35	3.75	3.75	3.75	1.31	3.75
Purplish blue	2.85	2.87	2.21	3.52	3.52	3.52	1.28	3.52
Moderate red	2.93	2.87	2.19	3.59	3.59	3.59	1.31	3.59
Purple	2.86	2.83	2.14	3.57	3.57	3.57	1.23	3.57
Yellow green	2.85	2.82	2.17	3.56	3.56	3.56	1.20	3.56
Orange yellow	2.84	2.84	2.12	3.49	3.49	3.49	1.13	3.49
Blue	2.34	2.32	1.96	3.36	3.36	3.36	1.13	3.36
Green	2.28	2.26	1.97	3.23	3.23	3.23	1.05	3.23
Red	2.33	2.30	1.94	3.21	3.21	3.21	1.04	3.21
Yellow	2.43	2.41	1.87	3.21	3.21	3.21	1.01	3.21
Magenta	2.36	2.35	1.87	3.15	3.15	3.15	1.03	3.15
Cyan	2.32	2.33	1.79	3.12	3.12	3.12	1.00	3.12
White	1.90	1.88	1.77	3.02	3.02	3.02	0.96	3.02
Neutral 8	1.87	1.87	1.68	2.84	2.84	2.84	0.93	2.84
Neutral 6.5	1.91	1.91	1.68	2.84	2.84	2.84	0.87	2.84
Neutral 5	1.93	1.93	1.62	2.81	2.81	2.81	0.82	2.81
Neutral 3.5	1.87	1.85	1.66	2.77	2.77	2.77	0.87	2.77
Black	1.85	1.82	1.62	2.73	2.73	2.73	0.86	2.73

Table: G-3: The average white reference signal value for each of the color samples in the ColorChecker target. The eighth record was acquired using a Schott infra-red filter.

Sample	Filter record number							
	1	2	3	4	5	6	7	8
Dark skin	186.8	173.1	209.6	206.1	245.7	185.2	164.9	243.4
Light skin	184.9	169.3	204.7	198.7	235.7	174.0	151.3	234.0
Blue sky	182.0	165.7	200.0	193.7	229.2	167.4	144.0	227.6
Foliage	179.9	163.9	197.3	192.1	227.7	165.7	143.1	225.6
Blue Flower	179.8	164.4	198.8	194.2	231.3	168.9	148.2	228.8
Bluish green	179.5	165.9	201.9	198.2	239.0	176.9	159.5	234.9
Orange	187.9	173.9	210.4	206.7	246.0	185.1	162.8	243.6
Purplish blue	186.6	170.9	205.9	200.3	236.8	174.6	150.5	234.7
Moderate red	186.8	169.9	204.2	197.5	232.8	170.2	148.0	231.0
Purple	187.0	169.8	203.0	196.4	233.4	171.0	156.7	230.8
Yellow green	187.5	171.1	205.3	199.6	236.9	172.6	149.5	234.3
Orange yellow	187.2	172.4	207.1	203.3	244.7	180.7	160.2	240.6
Blue	185.6	172.1	207.7	204.3	243.6	184.2	161.8	241.1
Green	183.6	168.5	202.3	198.4	234.7	173.6	149.2	232.4
Red	182.5	166.2	200.4	194.8	229.3	168.4	143.6	227.4
Yellow	182.0	165.5	198.7	193.0	227.3	166.5	143.4	225.4
Magenta	185.8	169.7	203.9	198.6	235.2	172.3	148.7	232.9
Cyan	186.2	171.5	205.7	202.0	242.9	180.2	159.2	239.5
White	179.7	167.0	201.1	199.5	238.8	182.5	161.0	235.8
Neutral 8	177.6	162.6	195.2	193.2	229.3	171.4	147.8	226.7
Neutral 6.5	174.4	159.7	192.6	188.7	223.5	165.4	141.0	221.3
Neutral 5	172.3	158.1	190.8	186.5	220.9	163.1	139.3	219.2
Neutral 3.5	173.1	158.7	191.7	188.3	225.0	166.1	143.3	222.3
Black	174.6	160.9	194.5	192.9	232.3	173.4	154.4	229.0

## Camera Photometric Corrections equations

$$s_1 = -0.0353 + 0.576 v_1 + 1.43 v_1^2$$

$$s_2 = -0.0295 + 0.566 v_2 + 1.82 v_2^2$$

$$s_3 = -0.0242 + 0.417 v_3 + 1.28 v_3^2$$

$$s_4 = -0.0252 + 0.432 v_4 + 1.34 v_4^2$$

$$s_5 = -0.0272 + 0.357 v_5 + 1.11 v_5^2$$

$$s_6 = -0.0244 + 0.389 v_6 + 2.2 v_6^2$$

$$s_7 = -0.0207 + 0.251 v_7 + 3.48 v_7^2$$

$$s_8 = -0.0238 + 0.371 v_8 + 1.22 v_8^2$$

where  $\{v\}$  is the set of camera signals, and  $\{s\}$  the set of corrected signals.

**Appendix H:  $\Delta E_{ab}^*$  for PCA and Direct Transformations.**

Table H-1: Average colorimetric errors,  $\Delta E_{ab}^*$ , based on the processing of captured ColorChecker pixel data by the PCA method, simple direct (Eq. 2-11) and complex direct (Eq. 2-12) calculations. Transformations for columns 2-4 were based on model camera and Munsell 37 data set. Column 5 is optimized for the camera signals. CIE illuminant D<sub>65</sub> and the 10° observer were used for the calculation, with each value based on a sample of 400 pixels.

Sample	PCA	simple	complex	PCA <sub>opt.</sub>
Dark skin	4.6	4.1	20.1	3.5
Light skin	4.5	7.0	9.8	4.4
Blue sky	3.8	10.2	9.8	3.0
Foliage	8.4	7.6	17.0	5.5
Blue Flower	3.4	5.0	12.1	3.5
Bluish green	3.7	3.1	3.2	4.7
Orange	11.0	7.1	15.3	3.9
Purplish blue	5.3	6.6	14.2	2.5
Moderate red	3.6	4.5	19.3	2.7
Purple	7.6	8.6	13.8	2.3
Yellow green	8.5	9.8	17.9	4.6
Orange yellow	9.2	10.9	14.3	6.8
Blue	1.0	16.1	12.7	6.1
Green	2.0	4.1	2.1	4.0
Red	8.2	11.2	36.3	4.1
Yellow	9.6	16.0	23.4	5.7
Magenta	6.1	8.5	15.3	4.2
Cyan	1.6	1.2	9.9	2.4
White	1.2	1.6	1.4	4.6
Neutral 8	1.7	2.1	2.0	4.3
Neutral 6.5	3.8	3.6	5.2	2.7
Neutral 5	1.9	3.4	6.0	2.1
Neutral 3.5	3.3	4.1	6.7	2.5
Black	7.3	5.1	12.5	6.8
average	5.1	6.7	12.5	4.0

**Appendix I: CIELAB image noise for PCA and Direct transformations.**

Table I-1: RMS colorimetric errors and  $E[\Delta E_{ab}^*]$  based on the processing of captured ColorChecker pixel data by the PCA method. Columns 1-4 are from transformations based on the model camera and Munsell 37 data set. The fifth column used a transformation matrix  $\mathbf{A}$  optimized for the experimental camera signals. The CIE illuminant  $D_{65}$  and the  $10^\circ$  observer were used for the calculation, with each value based on a sample of 400 pixels.

Sample	$\sigma_{L^*}$	$\sigma_{a^*}$	$\sigma_{b^*}$	$E[\Delta E_{ab}^*]$	$E[\Delta E_{ab}^*]_{\text{opt.}}$
Dark skin	0.6	2.8	3.3	4.4	3.3
Light skin	0.5	2.0	1.8	2.7	2.2
Blue sky	0.7	2.9	1.9	3.5	3.2
Foliage	0.8	4.0	3.9	5.6	3.9
Blue Flower	0.5	2.2	1.6	2.7	2.4
Bluish green	0.4	1.9	1.4	2.4	1.9
Orange	0.5	2.2	4.7	5.2	4.5
Purplish blue	0.5	2.1	1.4	2.6	2.6
Moderate red	0.6	2.8	3.0	4.2	3.7
Purple	0.9	4.2	2.3	4.9	4.3
Yellow green	0.4	1.9	3.1	3.7	2.8
Orange yellow	0.4	1.9	4.0	4.4	4.1
Blue	0.6	3.3	1.7	3.7	3.8
Green	0.5	2.5	2.8	3.8	3.2
Red	0.7	2.9	4.5	5.4	5.0
Yellow	0.4	1.9	4.1	4.5	4.1
Magenta	0.5	2.1	1.6	2.7	2.7
Cyan	0.4	2.1	1.3	2.5	2.3
White	0.4	1.8	1.4	2.3	1.9
Neutral 8	0.4	1.8	1.3	2.3	1.9
Neutral 6.5	0.5	2.1	1.7	2.7	2.4
Neutral 5	0.5	2.2	1.7	2.9	2.4
Neutral 3.5	0.7	3.3	2.8	4.4	4.0
Black	1.9	8.0	6.2	10.3	10.5
Average	0.6	2.7	2.7	3.9	3.5

Table I-2: RMS colorimetric errors and  $E[\Delta E_{ab}^*]$  based on the processing of captured ColorChecker pixel data by the two direct colorimetric transformations. Columns 1-4 are based on the simple model of Eq. (2-10) and columns 5-8 are based on the complex model of Eq. (2-11). Both transformations are based on the model camera and Munsell 37 data set. The CIE illuminant  $D_{65}$  and the  $10^\circ$  observer were used for the calculation, with each value based on a sample of 400 pixels.

Sample	Simple-direct				Complex-direct			
	$\sigma_{L^*}$	$\sigma_{a^*}$	$\sigma_{b^*}$	$E[\Delta E_{ab}^*]$	$\sigma_{L^*}$	$\sigma_{a^*}$	$\sigma_{b^*}$	$E[\Delta E_{ab}^*]$
Dark skin	1.9	3.0	3.5	5.0	10.0	16.0	4.1	19.0
Light skin	1.5	2.1	1.7	3.1	11.0	12.0	2.2	17.0
Blue sky	2.1	2.9	1.9	4.1	17.0	7.2	2.5	19.0
Foliage	2.5	3.6	3.7	5.7	13.0	23.0	7.7	27.0
Blue Flower	1.9	2.3	2.0	3.6	8.2	11.0	3.9	14.0
Bluish green	1.4	2.0	1.5	2.9	3.6	2.6	2.0	4.9
Orange	1.8	2.7	3.2	4.6	6.8	18.0	3.4	19.0
Purplish blue	1.7	2.4	2.0	3.6	8.0	4.6	2.6	9.5
Moderate red	1.8	3.0	2.8	4.5	12.0	17.0	3.9	21.0
Purple	2.7	3.6	2.8	5.3	22.0	27.0	7.4	36.0
Yellow green	1.7	2.5	3.4	4.6	11.0	12.0	4.2	17.0
Orange yellow	1.7	2.5	2.9	4.2	11.0	15.0	3.2	19.0
Blue	2.8	3.9	2.7	5.5	16.0	13.0	4.6	21.0
Green	2.1	2.8	3.3	4.8	8.2	5.3	3.8	10.0
Red	2.4	3.7	3.7	5.7	20.0	26.0	5.5	33.0
Yellow	1.6	2.3	3.3	4.3	21.0	17.0	4.2	27.0
Magenta	1.8	2.1	1.7	3.3	10.0	18.0	2.9	21.0
Cyan	1.9	2.3	1.9	3.6	8.8	10.0	2.3	14.0
White	1.5	2.0	1.8	3.1	5.2	4.0	1.4	6.7
Neutral 8	1.4	2.0	1.5	2.9	3.1	3.9	1.3	5.2
Neutral 6.5	1.7	2.0	1.9	3.3	3.9	3.7	1.6	5.6
Neutral 5	1.7	2.3	2.1	3.6	5.3	4.9	1.9	7.5
Neutral 3.5	2.6	3.3	4.2	5.9	15.0	6.2	3.6	16.0
Black	4.3	6.8	8.0	11.4	43.0	15.0	10.0	47.0
Average	2.0	2.8	2.8	4.5	12.2	12.2	3.8	18.2

## APPENDIX J: Camera RMS Noise for Macbeth ColorChecker Image Capture

Table: J-1: The observed camera rms noise for each of the color samples in the ColorChecker image files. The units are digital counts [0-255].

Sample	Filter record number							
	1	2	3	4	5	6	7	8
Dark skin	2.17	1.61	1.75	1.34	1.52	1.86	2.33	1.96
Light skin	1.64	1.45	1.70	1.55	1.81	1.93	1.90	1.76
Blue sky	1.93	1.96	2.18	1.74	2.02	1.92	1.91	1.83
Foliage	1.88	1.69	2.13	1.86	1.67	1.57	1.89	1.64
Blue Flower	2.22	1.81	1.61	1.94	2.27	1.63	1.91	2.23
Bluish green	1.79	1.84	2.21	1.62	1.61	2.08	2.20	1.82
Orange	1.86	1.59	1.92	1.47	1.86	2.21	2.85	1.74
Purplish blue	1.92	1.64	1.28	1.34	1.33	1.63	1.77	1.49
Moderate red	2.18	1.65	2.00	1.44	1.51	1.84	2.07	1.57
Purple	1.60	1.73	2.00	2.35	1.58	2.09	4.62	1.86
Yellow green	2.78	1.93	1.49	1.49	1.77	1.35	1.75	1.70
Orange yellow	1.93	1.85	1.85	1.30	1.62	1.70	2.02	1.50
Blue	2.05	1.59	1.45	1.65	1.40	2.58	2.34	1.63
Green	1.97	1.69	1.48	1.72	1.86	1.45	1.83	1.42
Red	2.03	2.32	1.70	1.46	1.80	1.87	1.50	1.55
Yellow	1.83	1.51	2.32	2.26	2.43	2.05	2.16	2.57
Magenta	1.63	1.55	1.30	1.87	1.80	1.68	1.88	1.90
Cyan	1.79	1.57	1.49	1.52	1.82	1.67	2.07	1.82
White	2.74	1.92	2.37	2.39	2.32	2.29	2.93	2.24
Neutral 8	1.85	1.61	1.69	1.64	1.72	1.67	2.05	1.90
Neutral 6.5	1.85	1.74	1.82	1.88	1.93	1.57	1.78	2.05
Neutral 5	1.70	1.62	1.41	1.45	1.46	1.58	2.08	1.61
Neutral 3.5	2.70	1.76	1.48	1.75	1.95	1.73	2.36	2.10
Black	2.68	2.23	2.53	2.00	1.96	1.90	1.98	2.11

Table: J-2: The observed camera rms dark for each for the image locations and camera settings used for the ColorChecker target capture. The units are digital counts [0-255]. Records 5, 6 and 8 have the settings as number 4.

Sample	Filter record number							
	1	2	3	4	5	6	7	8
Dark skin	3.77	3.77	3.56	3.84	3.84	3.84	2.99	3.84
Light skin	3.76	3.78	3.54	3.83	3.83	3.83	2.93	3.83
Blue sky	3.75	3.75	3.5	3.81	3.81	3.81	2.92	3.81
Foliage	3.76	3.74	3.48	3.81	3.81	3.81	2.92	3.81
Blue Flower	3.78	3.78	3.51	3.82	3.82	3.82	2.88	3.82
Bluish green	3.75	3.74	3.45	3.8	3.8	3.8	2.85	3.8
Orange	3.66	3.65	3.43	3.79	3.79	3.79	2.78	3.79
Purplish blue	3.61	3.61	3.37	3.77	3.77	3.77	2.76	3.77
Moderate red	3.65	3.64	3.35	3.8	3.8	3.8	2.79	3.8
Purple	3.61	3.61	3.33	3.78	3.78	3.78	2.71	3.78
Yellow green	3.66	3.65	3.37	3.79	3.79	3.79	2.73	3.79
Orange yellow	3.63	3.64	3.33	3.74	3.74	3.74	2.63	3.74
Blue	3.44	3.42	3.24	3.74	3.74	3.74	2.62	3.74
Green	3.41	3.4	3.24	3.71	3.71	3.71	2.56	3.71
Red	3.45	3.45	3.24	3.73	3.73	3.73	2.55	3.73
Yellow	3.47	3.46	3.18	3.69	3.69	3.69	2.49	3.69
Magenta	3.49	3.46	3.23	3.7	3.7	3.7	2.55	3.7
Cyan	3.42	3.42	3.14	3.66	3.66	3.66	2.48	3.66
White	3.2	3.2	3.13	3.66	3.66	3.66	2.45	3.66
Neutral 8	3.2	3.21	3.07	3.62	3.62	3.62	2.41	3.62
Neutral 6.5	3.22	3.22	3.07	3.61	3.61	3.61	2.34	3.61
Neutral 5	3.23	3.24	3.02	3.6	3.6	3.6	2.28	3.6
Neutral 3.5	3.19	3.19	3.05	3.57	3.57	3.57	2.33	3.57
Black	3.18	3.16	3.02	3.56	3.56	3.56	2.32	3.56

## APPENDIX K: CIELAB Color-Differences Due To Multispectral Camera Signal Quantization

Table K-1: CIELAB color-differences due to uniform camera signal quantization, and modified PCA spectral reconstruction. Signals (1, 2, 3, 7, 8) were used, with 12-bit (4096-level) signal encoding, eight basis vectors, CIE D<sub>65</sub> illuminant and 10° observer. Rounding error is between the actual color-locus and the nearest discrete level.

ColorChecker Sample	quantized coordinates			rounding, error $\Delta E_{ab}^*$	interval, $\Delta E_{ab}^*$		
	$L_{ab}^*$	$a^*$	$b^*$		mean	median	max.
Dark skin	36.80	12.70	12.74	0.05	0.13	0.12	0.24
Light skin	66.02	12.57	15.93	0.02	0.05	0.05	0.10
Blue sky	52.34	-2.97	-22.10	0.02	0.08	0.07	0.16
Foliage	42.60	-14.41	22.09	0.06	0.13	0.12	0.25
Blue flower	57.59	6.15	-25.67	0.04	0.06	0.06	0.13
Bluish green	72.92	-31.24	2.43	0.02	0.05	0.05	0.11
Orange	58.94	32.73	52.94	0.03	0.08	0.07	0.15
Purplish blue	42.97	7.38	-40.72	0.07	0.10	0.09	0.20
Moderate red	51.64	41.79	12.62	0.03	0.07	0.07	0.12
Purple	30.63	21.20	-25.21	0.07	0.14	0.14	0.27
Yellow green	72.07	-21.44	58.66	0.02	0.06	0.06	0.12
Orange yellow	70.27	18.98	64.32	0.03	0.06	0.06	0.12
Blue	32.62	9.66	-47.10	0.09	0.14	0.13	0.28
Green	55.60	-35.19	36.22	0.06	0.10	0.09	0.19
Red	40.42	49.26	26.03	0.08	0.11	0.10	0.21
Yellow	80.01	3.42	78.84	0.03	0.06	0.06	0.11
Magenta	51.61	42.53	-16.62	0.02	0.07	0.06	0.12
Cyan	53.34	-30.52	-22.99	0.02	0.09	0.08	0.20
White	96.36	-1.21	2.65	0.00	0.03	0.03	0.06
Neutral 8	81.41	-0.39	-0.26	0.01	0.04	0.04	0.08
Neutral 6.5	66.49	0.10	-0.08	0.02	0.05	0.05	0.11
Neutral 5	50.90	0.26	-0.39	0.01	0.08	0.08	0.16
Neutral 3.5	33.94	-0.15	-0.34	0.11	0.15	0.14	0.30
Black	19.09	0.12	-0.97	0.08	0.30	0.28	0.60
Average					0.09	0.09	0.18

## APPENDIX L: Camera Image Noise as Projected into CIELAB

Table L-1: Stochastic errors in CIELAB due to detector noise, following the dark- and shot-noise model. The imager dynamic range (max. signal/ $\sigma_{\text{dark}}$ ) of 1200 and maximum signal charge of 60,000 electrons, calculated for the ColorChecker samples. The CIELAB transformation, following spectral reconstruction using five (1, 2, 3, 7, 8) camera signals, is for CIE illuminant  $D_{65}$ , and  $10^\circ$  observer. The seventh column is the mean color-difference.

Sample	$\mu_{L^*}$	$\mu_{a^*}$	$\mu_{b^*}$	$\sigma_{L^*}$	$\sigma_{a^*}$	$\sigma_{b^*}$	$E[\Delta E_{ab}^*]$
Dark skin	36.80	12.66	12.72	0.22	1.01	0.56	1.03
Light skin	66.02	12.58	15.94	0.15	0.74	0.38	0.74
Blue sky	52.34	-2.95	-22.11	0.17	0.91	0.38	0.85
Foliage	42.60	-14.36	22.11	0.19	1.14	0.54	1.10
Blue flower	57.59	6.11	-25.67	0.16	0.83	0.36	0.79
Bluish green	72.92	-31.26	2.42	0.14	0.88	0.34	0.80
Orange	58.95	32.74	52.97	0.17	0.67	0.53	0.80
Purplish blue	42.98	7.32	-40.70	0.19	0.96	0.40	0.90
Moderate red	51.65	41.78	12.64	0.18	0.66	0.44	0.73
Purple	30.62	21.27	-25.23	0.25	1.07	0.52	1.06
Yellow green	72.08	-21.45	58.64	0.14	0.84	0.46	0.86
Orange yellow	70.27	19.01	64.32	0.15	0.68	0.49	0.78
Blue	32.63	9.75	-47.10	0.22	1.12	0.46	1.04
Green	55.60	-35.24	36.23	0.16	1.08	0.49	1.02
Red	40.43	49.23	26.11	0.23	0.68	0.60	0.86
Yellow	80.01	3.40	78.82	0.14	0.70	0.49	0.79
Magenta	51.61	42.55	-16.63	0.19	0.68	0.40	0.72
Cyan	53.35	-30.50	-22.98	0.16	1.08	0.38	0.95
White	96.36	-1.21	2.65	0.12	0.66	0.30	0.63
Neutral 8	81.41	-0.37	-0.26	0.13	0.71	0.32	0.68
Neutral 6.5	66.49	0.09	-0.09	0.15	0.79	0.36	0.75
Neutral 5	50.91	0.26	-0.39	0.17	0.91	0.41	0.87
Neutral 3.5	33.94	-0.04	-0.37	0.22	1.18	0.54	1.12
Black	19.11	0.10	-0.89	0.34	1.80	0.82	1.71
Average				0.18	0.91	0.46	0.90